



ΠΑΝΕΠΙΣΤΗΜΙΟ ΚΡΗΤΗΣ
ΤΜΗΜΑ ΙΑΤΡΙΚΗΣ
ΕΡΓΑΣΤΗΡΙΟ ΙΑΤΡΙΚΗΣ ΦΥΣΙΚΗΣ
ΔΙΕΥΘΥΝΤΗΣ: ΚΑΘΗΓΗΤΗΣ Ι. ΔΑΜΗΛΑΚΗΣ



ΜΕΤΑΠΤΥΧΙΑΚΟ ΔΙΠΛΩΜΑ ΕΙΔΙΚΕΥΣΗΣ

ΔΙΠΛΩΜΑΤΙΚΗ ΕΡΓΑΣΙΑ

**Απεικονιστικές μετρήσεις της παραμέτρου T2 με τεχνικές ΑΜΣ σε
σχέση με τις ηλεκτρικές αγωγιμότητες και θερμοκρασίες στις
κλίμακες ήπιας υπερθερμίας.**

ΚΑΡΚΑΒΙΤΣΑΣ ΣΠΥΡΙΔΩΝ

ΕΠΙΒΛΕΠΩΝ

ΘΩΜΑΣ ΜΑΡΗΣ

ΚΑΘΗΓΗΤΗΣ ΙΑΤΡΙΚΗΣ ΦΥΣΙΚΗΣ

ΗΡΑΚΛΕΙΟ, ΟΚΤΩΒΡΙΟΣ 2020

ΔΙΑΠΑΝΕΠΙΣΤΗΜΙΑΚΟ ΔΙΑΤΜΗΜΑΤΙΚΟ
ΠΡΟΓΡΑΜΜΑ ΜΕΤΑΠΤΥΧΙΑΚΩΝ ΣΠΟΥΔΩΝ ΣΤΗΝ
ΙΑΤΡΙΚΗ ΦΥΣΙΚΗ – ΑΚΤΙΝΟΦΥΣΙΚΗ



**UNIVERSITY OF CRETE
SCHOOL OF MEDICINE
DEPARTMENT OF MEDICAL PHYSICS
CHAIRMAN: PROFESSOR IOANNIS DAMILAKIS**



POSTGRADUATE SPECIALISATION DIPLOMA

MASTER THESIS

**T2-quantitative MRI measurements in relation to Electrical
Conductivity and temperature on mild hyperthermia scales.**

KARKAVITSAS SPYRIDON

SUPERVISOR

THOMAS G.MARIS

PROFESSOR OF MEDICAL PHYSICS

HERAKLION, OCTOBER 2020

INTERDEPARTMENTAL

POSTGRADUATE PROGRAM

MEDICAL PHYSICS – RADIATION PHYSICS

Abstract

Magnetic Resonance Imaging (MRI) is a noninvasive imaging technique that produces 3D images with superior soft tissue contrast and high spatial resolution. Furthermore, MRI is a core diagnostic tool in demonstration and visualization of spatial distribution of various diseases and disorders with many different contrasts available on MR images. The signal, which is detected and quantified by various MR pulse sequences, depends on intrinsic parameters such as the longitudinal relaxation time T1, transverse relaxation time T2, overall transverse relaxation T2*, proton density (PD) and molecular diffusion (ADC). However, academic interest in researching the temperature dependence of many measurable signal parameters (T1 and T2 relaxation rates, diffusion coefficient (ADC), proton resonance frequency, PRF, and magnetization transfer, MT) has been growing since 1980.

Since many NMR properties are temperature sensitive, non invasive temperature measurements can be achieved with MRI. Particularly, the ability of MRI to provide in vivo three – dimensional and temperature sensitive quantitative maps makes it the ideal modality for guiding and monitoring many hyperthermic procedures

Various temperature sensitive MR parameters have been proposed and investigated for MR based thermometry. The aim of this study was twofold. Firstly, we wanted to measure and characterize the temperature dependence of T2 relaxation time in 6 samples of typical electrolytes solutions (NaCl solutions) with varying salt concentration and in one sample of tap water. T2 relaxation time was measured in the temperature range of 20°C up to 45°C. In addition T2 relaxation time maps of the solutions were acquired using a experimental setup on a hybrid clinical MRI system under controlled experimental conditions. Two different T2 - mapping techniques were compared : A Multi – Echo Spin Echo (MESE) and a 2D Half – Fourier Acquisition Single – Shot Turbo spin Echo (HASTE) sequence. Based on the results we concluded which imaging method is better for quantifying the effect of temperature on the T2 relaxation time. Following the same procedure we tried to quantify the relationship between temperature and proton density (PD).

Secondly we wanted to investigate the relationship between T2 relaxation time and electrical conductivity (EC). At first, the EC of all six sodium chloride solutions was measured in the temperature range of 20°C up to 45°C. Using these results and the T2 values obtained from MESE and HASTE sequence, we tried to quantify a possible correlation between T2 relaxation time and EC.

Περίληψη

Η Απεικόνιση Μαγνητικού Συντονισμού (ΑΜΣ) αποτελεί μια μέθοδο παραγωγής 3D εικόνων με εξαιρετική αντίθεση μαλακών ιστών και άριστη χωρική διακριτική ικανότητα. Επιπρόσθετα, η ΑΜΣ μπορεί να χαρακτηριστεί ως ένα ιδανικό διαγνωστικό μέσο για την ανάδειξη και οπτικοποίηση ασθενειών μέσω της υψηλής σκιαγραφικής αντίθεσης που χαρακτηρίζει τις παραγόμενες εικόνες. Το σήμα μαγνητικού συντονισμού που αποτελεί συνάρτηση παραμέτρων όπως τους χρόνους μαγνητικής αποκατάστασης T1 και T2, την πυκνότητα πρωτονίων, PD, λαμβάνεται και ποσοτικοποιείται με την χρήση ποικίλων απεικονιστικών ακολουθιών. Ωστόσο, το ακαδημαϊκό ενδιαφέρον στην θερμοκρασιακή εξάρτηση μαγνητικά μετρούμενων παραμέτρων (χρόνοι μαγνητικής αποκατάστασης T1 και T2, συντελεστής διάχυσης ADC, συχνότητα συντονισμού πρωτονίου και μεταφορά μαγνήτισης, MT) υπάρχει ήδη από τις αρχές του 1980.

Η θερμοκρασιακή εξάρτηση αυτών των παραμέτρων καθιστούν το απεικονιστικό σύστημα MR ένα μη επεμβατικό εργαλείο στην μέτρηση θερμοκρασίας. Πιο συγκεκριμένα η δυνατότητα παραγωγής θερμοκρασιακών παραμετρικών χαρτών κάνει δυνατή την καταγραφή θερμοκρασιακής μεταβολής σε διαδικασίες υπερθερμίας.

Ο στόχος της παρούσας διπλωματικής εργασίας ήταν διπλός. Αρχικά, θέλαμε να μετρήσουμε την χρονική παράμετρο T2 και να ποσοτικοποιήσουμε την σχέση της με την θερμοκρασία σε 6 διαλύματα χλωριούχου νατρίου (NaCl) διαφορετικής περιεκτικότητας και σε ένα δείγμα νερού. Η θερμοκρασιακή εξάρτηση του χρόνου T2 εξετάστηκε στο εύρος 20°C έως και 45°C. Για τον σκοπό αυτό χρησιμοποιήθηκε υβριδικό κλινικό σύστημα ΑΜΣ υπό ελεγχόμενες πειραματικές συνθήκες. Έγινε χρήση δύο διαφορετικών τεχνικών για την κατασκευή παραμετρικών χαρτών T2 : Της Multi- Echo Spin Echo (MESE) και της 2D Half – Fourier Acquisition Single – Shot Turbo spin Echo (HASTE). Με βάση τα αποτελέσματα συμπεράναμε ποια απεικονιστική μέθοδος είναι η καλύτερη για την ποσοτικοποίηση της σχέσης μεταξύ της χρονικής παραμέτρου T2 και της θερμοκρασίας. Ακολουθώντας την ίδια διαδικασία προσπαθήσαμε να ποσοτικοποιήσουμε και την εξάρτηση της θερμοκρασίας με την πυκνότητα πρωτονίων, PD.

Ο τελικός στόχος της παρούσας εργασίας ήταν η διερεύνηση της σχέσης μεταξύ της χρονικής παραμέτρου T2 και ηλεκτρικής αγωγιμότητας. Αρχικά, μετρήθηκε η ηλεκτρική αγωγιμότητα και των 6 διαλυμάτων χλωριούχου νατρίου σε εύρος θερμοκρασιών από 20°C έως 45°C. Κάνοντας χρήση αυτών των αποτελεσμάτων και των μετρήσεων T2, προσπαθήσαμε να βρούμε και να ποσοτικοποιήσουμε την συσχέτιση της μαγνητικής παραμέτρου T2 και την ηλεκτρικής αγωγιμότητας.

Ευχαριστίες

Η παρούσα διπλωματική εργασία εκπονήθηκε στο εργαστήριο Ιατρικής Φυσικής του Πανεπιστημίου Κρήτης.

Αρχικά θα ήθελα να ευχαριστήσω τον επιβλέπων της εργασίας μου, κ. Θωμά Μαρή, καθηγητή Ιατρικής Φυσικής του Πανεπιστημίου Κρήτης για το απαιτητικό και ταυτόχρονα πολύ ενδιαφέρον θέμα που μου ανάθεσε. Επιπλέον, θα ήθελα να τον ευχαριστήσω για τον χρόνο που διέθεσε για την λήψη σημαντικών μετρήσεων, όπου χωρίς αυτές η εκπλήρωση αυτής της εργασίας δεν θα ήταν εφικτή. Τέλος, τον ευχαριστώ για την αγορά ενός μετρητικού εξοπλισμού όπου βοήθησε σημαντικά στην αποτελεσματική λήψη μετρήσεων αυτής της εργασίας.

Θα ήθελα να ευχαριστήσω επίσης τον κ. Ιωάννη Δαμηλάκη, καθηγητή Ιατρικής Φυσικής του Πανεπιστημίου Κρήτης και διευθυντή του εργαστηρίου Ιατρικής Φυσικής που δέχθηκε να είναι μέλος στην τριμελή επιτροπή.

Τέλος, θα ήθελα να ευχαριστήσω και τον κ. Κώστα Περισυνάκη, καθηγητή Ιατρικής Φυσικής του Πανεπιστημίου Κρήτης που δέχθηκε να είναι μέλος στην τριμελή συμβουλευτική επιτροπή.

Επίσης ευχαριστώ την οικογένεια μου που με στηρίζουν σε κάθε μου βήμα αλλά και την κοπέλα μου, Μάνθα Λαμπρούση όπου έστω και από μακριά ήταν πάντα δίπλα μου για να μοιραστώ τους προβληματισμούς μου και να με υποστηρίξει σε ψυχολογικό επίπεδο.

Πίνακας περιεχομένων

1.INTRODUCTION	7
1.1 Magnetic Resonance Imaging (MRI)	8
1.2 Principles of MRI	8
1.2.1 Nuclear Magnetic Resonance : Equilibrium state & excitation	8
1.2.2 Relaxation back to equilibrium	11
1.2.2.1 Molecular motion and relaxation	11
1.2.2.2 Description of molecular motion : Correlation time	11
1.2.2.3 Spectral density function $J(\omega)$	12
1.2.2.4 Relaxation mechanism : Dipole –Dipole interaction	13
1.2.2.5 Autocorrelation function	15
1.2.3. Expression of the relaxation times T_1 and T_2	16
1.2.4 Temperature dependence of T_1 and T_2 relaxation times	23
1.2.5 Temperature dependence of proton density (PD)	26
1.3 Introduction to MRI sequences	28
1.3.1 Single or Conventional Spin Echo (SE) sequence	28
1.3.2 Multi- Echo Spin Echo (MESE) sequence	28
1.3.3 HASTE: Half – Fourier Single Shot Turbo Spin Echo sequence	29
1.4 Introduction to image contrast	30
1.4.1 Image contrast in SE sequence	30
1.4.2 Image contrast in MESE sequence	30
1.4.3. Image contrast in TSE sequence	30
1.4.4 Image contrast in HASTE sequence	31
1.5 Temperature dependence of Electrical Conductivity in typical electrolyte solutions	31
1.6 Magnetic field within electrically conductive material	33
Scope of this study – questions addressed	34
2.MATERIALS AND METHODS	35
2.1.Electrical conductivity measurement	36

2.2 MRI system: Siemens Magnetom Sonata	38
2.3 Temperature measurement	40
2.4 Laboratory water bath	43
2.5 Centrifugal water pump	46
2.6 Experimental design	47
2.6.1 Sodium chloride (NaCl) solution	47
2.6.2 Closed loop circulation system	50
2.6.3 MRI Image acquisition	51
2.6.4 MR Data Handling and Quantification	61
2.6.4.1 Weighted least squares (WLS)	61
2.6.4.2 Random noise estimation from the image	62
2.6.4.3 Measurements of T2/PD on T2/PD parametric maps	63
2.6.4.4 Data handling and Analysis	67
3.RESULTS	68
3.1 T2 relaxation time vs temperature and EC measurements	69
3.2 Electrical Conductivity (EC) vs temperature	85
3.3 Correlation between T2 relaxation time and EC measurements	87
4. DISCUSSION/CONCLUSIONS	93
4.1 Evaluation of the goodness of fit	94
4.1.1 Variation of T2 with temperature	94
4.1.2 Variation of Proton density (PD) with temperature	95
4.1.3 Variation of T2 with Electrical Conductivity (EC)	96
4.2 Discussion	97
4.2.1 Hyperthermia treatment	97
4.2.2 Hyperthermia treatment and MRI	98
References	100

1. INTRODUCTION

1.1 Magnetic Resonance Imaging (MRI)

MRI is a non-invasive imaging technique that produces 2D/3D images with excellent soft tissue contrast and high spatial resolution in any orientation. In clinical MRI the primary sources of signal are water hydrogen nuclei or protons in water and freely moving fat containing tissues. In conventional MRI the image contrast depends principally on tissue T1 (longitudinal relaxation time), T2 (transverse relaxation time), T2* (overall transverse relaxation time), PD (proton density) and water/blood molecular diffusion and macroscopic flow. The final MR image voxel signal depends on the contribution of all the above parameters and it is represented as a 2D/3D image with contrast based on the relative parameter weight (T1-W, T2-W, T2*-W, PD-W Diffusion-W etc). Thus this imaging method by using non ionizing radiation has been proven to be a validated tool to diagnose and detect diseases and disorders.

1.2 Principals of MRI

1.2.1 Nuclear Magnetic Resonance: Equilibrium state & excitation.

Nuclear Magnetic Resonance is the physical process by which the signal detected in MRI is generated, it is the foundation on which MRI.

As we know proton (1H) has spin quantum number of $\frac{1}{2}$ ($i = \frac{1}{2}$) and it is the most commonly used nucleus in NMR experiments. The positively charged proton can be considered to be revolving about an axis (spinning hydrogen nucleus-spin) and it generates its own local magnetic dipole field.¹ The magnetic moment vector, $\vec{\mu}$ associated with this field will be oriented parallel to the axis of self-rotation of the proton. The magnetic moment $\vec{\mu}$ is directly proportional to proton's internal angular momentum \vec{I} (spin) ($\vec{\mu} = \gamma \cdot \vec{I}$, γ is the gyromagnetic ratio of proton)². In the presence of an external and static magnetic field B_0 , there is a torque-induced precession of the magnetic moment around an axis which is parallel to B_0 . The frequency of precession is expressed by the Larmor equation ($\omega_0 = \gamma \cdot B_0$).¹

Consider a large collection of protons (e.g. water) in free space, in the absence of B_0 . The vectors of the magnetic moments of the protons are irregularly arranged in space so that the vector sum of these is zero.³ On the contrary, in the presence of B_0 the magnetic moments, of the protons, are oriented approximately either parallel (low energy state) or anti-parallel (high energy state) to the main field.² In thermal equilibrium, all isochromats of protons (average magnetic moment of a microscopic group of nuclei all precessing at the same frequency and phase) precess at the same Larmor frequency but they are all out of phase with each other.¹ Also, the population in low energy state is slightly greater than the number of protons in high energy state. This unequal number in each energy state means that the vector sum of isochromats will be nonzero and will be aligned with B_0 (figure 1). The system is magnetized with net magnetization, \vec{M} . The magnitude of \vec{M} can be of the order of a microtesla (μT) and it is a measurable quantity.²

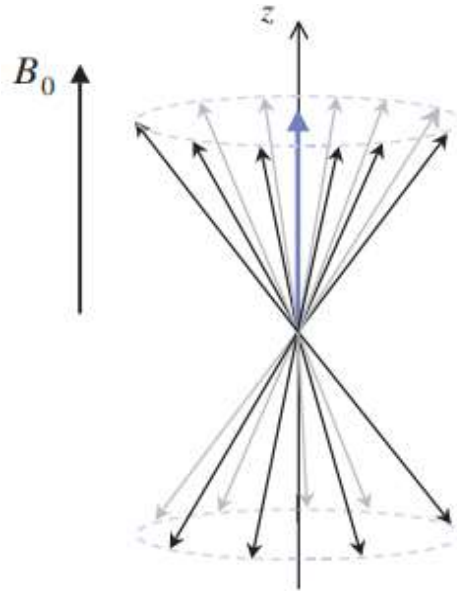


Figure1: Parallel or anti-parallel orientation of isochromats (black arrows) with the main magnetic field B_0 . The vector sum of these produces the net magnetization (blue arrow).²

In order to measure the net magnetization (which is along z-axis) of the sample of protons we must tip \vec{M} in the $x - y$ or transverse plane (excitation of the system of protons). This can be done by using a Radiofrequency (RF) pulse 90° (excitation pulse). Microscopically, there is net absorption of energy by the system, so the population in both energy states is equal leaving no magnetization along z-axis.²

After the RF pulse is off, the perturbed system returns (or relaxes) back to a state of equilibrium and there is emission of the absorbed energy (provided to the system of spins by the RF pulse) through naturally occurring mechanisms (spin-lattice/ T1 and spin-spin/ T2 relaxation). During relaxation the net magnetization as a vector is consisted by longitudinal and the transverse component. The longitudinal component (M_z) is caused by the difference in the number of magnetic moments in high and low energy state, and the transverse magnetization (M_{xy}) due to spins getting into phase with each other.¹

Each of these magnetizations has a characteristic time which is called relaxation time, so there are 2 kinds of relaxation time constants. T1-relaxation time, which is called spin-lattice relaxation time, is the required time for the longitudinal magnetization to return to its 63% of its strength in thermodynamic equilibrium state (initial state) in the direction of B_0 . T2-relaxation time, known as spin-spin relaxation time, is the required time for the transverse magnetization to fall to its 37% (or lose the 63%) of its strength in thermodynamic equilibrium state (initial state). T1 and T2 relaxation are two different and independent mechanisms that occur at the same time.³

During relaxation the recovery of longitudinal magnetization follows an exponential growth process with time constant T1 according to the following equation:³

$$M_z(t) = M_0 \cdot \left(1 - e^{\left(-\frac{t}{T1}\right)}\right) \quad (1)$$

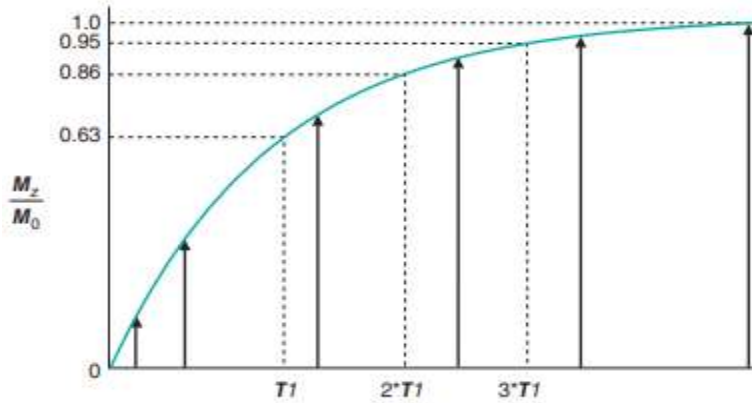


Figure 2: Exponential growth of longitudinal magnetization M_z with time constant T_1 . M_z reaches 63% of its initial value (M_0) at time $t=T_1$. As more protons release their energy M_z is very close to M_0 ($\frac{M_z}{M_0} \approx 1$) approximately at time $t=5 \cdot T_1$.³

Immediately after the RF pulse all individual spins within the isochromat, \vec{M}_c are completely in phase with each other (phase coherence). Also the RF pulse generates phase coherence between the isochromats, so that the transverse magnetization has maximum value ($M_{xy}=M_0$)¹. Spin-spin relaxation mechanisms cause the loss of phase coherence between spins within the isochromat (or randomization of magnetic moments in the transverse plane). In other words, spin-spin relaxation causes a cumulative and random loss in phase ($\Delta\phi$) between adjacent spins. As a result the magnitude of the transverse component of \vec{M}_c decays with time (figure 3a).⁴ Taking all the above into consideration, the disappearance of transverse magnetization is given by the following equation:²

$$M_{xy}(t) = M_0 \cdot e^{-\frac{t}{T_2}} \quad (2)$$

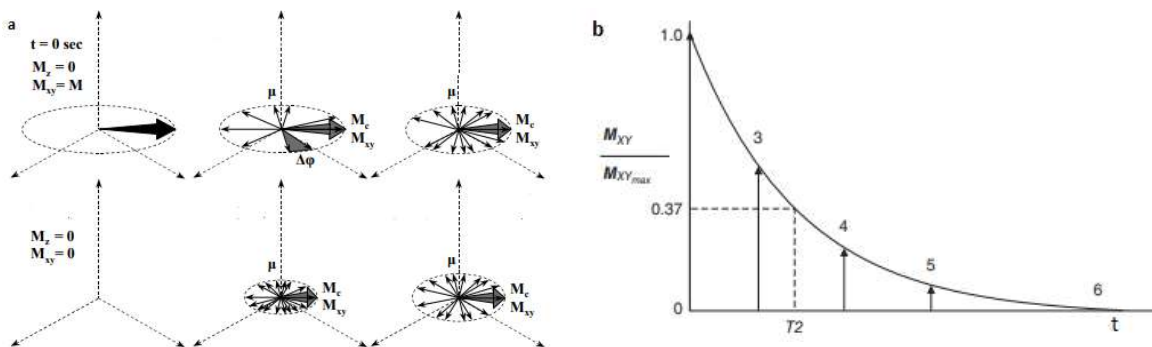


Figure 3: (a) Following a 90° pulse, the spins within the isochromat M_c precess initially in phase (phase coherence). As time elapses, there is a cumulative loss in phase ($\Delta\phi$) between spins. As more time elapses the transverse coherence becomes smaller resulting in transverse magnetization decay (M_{xy} goes to zero).⁵ (b) Transverse magnetization decay is described by an exponential curve with time constant T_2 . T_2 is the time when M_{xy} has decayed to 37% of its initial value ($M_{xy\max}$). As time passes by (3,4,5,6) M_{xy} diminishes to zero.³

1.2.2 Relaxation back to equilibrium

1.2.2.1 Molecular motion and relaxation.

As described above, if irradiation at the Larmor frequency (RF pulse) is applied to the system of protons then it will be perturbed from its equilibrium state (excitation of the system). After the RF pulse is switched off the system will return back to its initial state by releasing the energy that had been put into it. However, this process which is termed as relaxation is not spontaneous. A stimulating magnetic field causes spins in the high energy state to return to low energy state.² This fluctuating magnetic field arises largely from the thermal motion (Brownian motion) or tumbling of the neighbouring protons, nuclei or other molecules where spins reside (dipole-dipole interaction).^{2,4,5} Components of the local field that oscillate at the Larmor frequency, ω_0 , of the spin system can stimulate transitions between low and high energy state.^{2,4,5} This results in the exponential regrowth of the longitudinal magnetization or T1 relaxation. It is noted that only the perpendicular to B_0 component of the background field (as the B_1 field in excitation) is responsible to T1 relaxation.^{1,5} The exponential decay of the transverse magnetization or T2 relaxation is due to gradual loss in phase coherence between the spins within isochromats.^{2,4} Again, this irreversible loss is caused by the various molecular motion which generates random local field fluctuations. Variations in the local magnetic field cause microscopic and time dependent variations in Larmor frequency of the individual magnetic moments. Hence, spins immediately begin to dephase and phase coherence between them is lost.

In addition any process causing T1 relaxation results in T2 relaxation (ie phase incoherence between spins in transverse plane). However, T2 relaxation can occur without T1 relaxation by the longitudinal component of the local static field (parallel to B_0), and this is known as "secular" contribution to T2. Therefore, T1 is always greater than or equal to T2.¹ Even though dipole-dipole interaction is the major mechanism of relaxation, any process that generates magnetic field fluctuations can induce relaxation (chemical shift anisotropy, molecular diffusion, chemical exchange and so forth).¹

The contribution of molecular thermal motion to T1 and T2 relaxation have been successfully explained by the Bloembergen, Purcell and Pound (BPP) theory.⁶ Solomon generalized BPP theory and derived frequency dependent equations of T1 and T2 relaxation times for a pair of interacting spins with $i = \frac{1}{2}$ in the presence of a main magnetic field B_0 .⁷

1.2.2.2 Description of molecular motion: Correlation time.

Every atom or molecule in liquids and solutions undergo fast thermal motion. They tumble (rotational reorientations, vibrational motions, translational motions or their combinations) in a stochastic (random) and continuous way (Brownian motion)^{1,2,4}. Also their state of motion changes at a rapid and random rate because they interact (collide) with each other within the medium.² This kind of movement is characterized by the temperature which is a measure of the average kinetic energy of the

randomly tumbling molecules.⁸ Quantitatively these random (Brownian) movements are characterized by the correlation times, τ_c .^{1,4,8} This time is named like that because it associates two different points in time and space during the random movement of the molecule.⁴ Alternatively correlation time is the required time in which the orientation of a molecule changes. For instance, rotational correlation time can be considered as the average time required for a particular molecule to rotate one radian.¹² Translational correlation time is the time interval over which a molecule translate through a distance equal to its size.⁴ Each type of motion is characterized by its own unique correlation time. The overall or complex motion of the molecule is a combination of different types of motions (translational, rotation, chemical exchange etc) that occurring simultaneously and its resulting correlation time τ_c is given by the following equation:⁴

$$\frac{1}{\tau_c} = \frac{1}{t_a} + \frac{1}{t_b} + \frac{1}{t_d} + \dots \quad (3)$$

Where t_a, t_b, t_d are the correlation times that correspond to different components of the overall molecular motion.

Consequently, the motion of high mobile molecules in solution will be characterized by a short correlation time τ_c (or high molecular tumbling rate). On the contrary immobile molecules in solids or high viscosity liquids have longer τ_c (or low molecular tumbling rate).^{2,5}

1.2.2.3 Spectral density function $J(\omega)$

Via Fourier Transform we can decompose this random molecular tumbling into its various frequency components.⁴ The frequency distribution depends on the correlation time that is used to characterize random movements.⁸ Essentially, spectral density function expresses the probability of finding a component of motion at a given frequency ω (in *rad/sec*).² Molecules that tumble rapidly (short τ_c , molecules with small molecular weight, free molecules in liquid with low viscosity) will have motion with contribution from higher frequency components (broad spectrum).⁵ However, because the overall motion is composed of wide range of frequencies, the amplitude of each frequency is relatively small.² Conversely, molecules that tumble slowly (long τ_c , molecules with large molecular weight, bound molecules in solid material) will have almost no contribution from high frequency components (narrow spectrum), or in other words, slow motions emphasize the low frequency components. Despite that, the amplitude of motion will be large in each of the low frequency components.^{2,5,8} Spectral density as a function of frequency for slow, intermediate and fast molecular tumbling is depicted in the following diagram (figure 4).⁴ In each of the three cases the amplitude of the motion components above a certain frequency decreases rapidly so that there are no components of the motion at higher frequencies. This threshold frequency which characterizes the molecular tumbling is equal to $1/\tau_c$.⁸ Finally, since $J(\omega)$ represents probability, the area under each curve remains constant.⁴

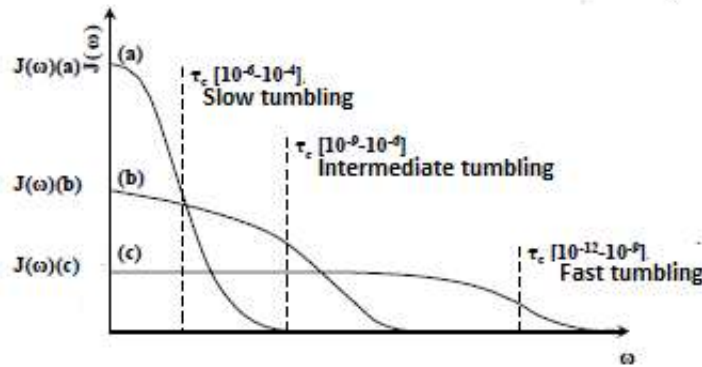


Figure 4: Spectral density function $J(\omega)$, as a function of frequency for slow (a), intermediate (b) and fast (c) motion.⁴

1.2.2.4 Relaxation mechanism: Dipole-dipole interaction

As stated before the recovery of the longitudinal equilibrium magnetization is described by the spin-lattice relaxation time T_1 while the exponential decay of transverse magnetization is characterized by the spin-spin relaxation time T_2 . Magnetic active nuclei can be thought of as magnetic dipoles whose electromagnetic fields interact through space. For many nuclei ($i = 1/2$, eg protons) the dipolar interaction is the most important contribution to T_1 and T_2 relaxation.^{1,9} The dipole-dipole relaxation mechanism is depended on many factors such as the internuclear distance, types of spins that interact with each other, angle between the vector that connect the two nuclei and the main static magnetic field and of course their relative motion.¹

Relative motion of the dipolar pair is depended on thermal molecular motion, so it is straightforward to say that this factor determines the type of relaxation (T_1/T_2 relaxation or combined). In particular, the fluctuations of one spin that resides on a molecule are determined on the molecular tumbling.⁵ Thus the frequency distribution of the randomly fluctuating magnetic field is the same with the spectrum of the molecular motion.⁴ T_1 relaxation is mainly induced by frequency components near or at Larmor frequency.¹ On the other hand T_2 relaxation is induced mainly by relatively static dipolar magnetic fields.² As it can be seen from equation (4) and (5) the strength of the dipole field is inversely proportional to the cube of the internuclear distance, r . However, the rate of relaxation driven by dipolar interaction fall off as $\frac{1}{r^6}$. In water molecules, mainly intramolecular dipolar interactions cause T_1/T_2 relaxation to occur.^{2,6,7} In addition the strength of interaction depends on the magnitudes of the individual interacting magnetic moments. Interaction between proton and an electron is much stronger than proton-proton interaction. This happens because the value of the gyromagnetic ratio of an electron is much larger than the value of proton.^{1,5} Thus relaxation driven by electron-nuclear interaction is more efficient than relaxation driven by nuclear-nuclear interaction.⁵ MRI contrast agents containing substances like gadolinium which possess 7 unpaired electrons. Electrons interact strongly with nearby protons that reside on water

molecules. Thus efficient T1 and T2 relaxation can be induced due to strong dipole-dipole interaction.¹

When two magnetic active nuclei move in close proximity with each other, the total magnetic field around each one is influenced. The magnetic moment (or dipolar field) of one spin affects the local field of the other adjacent in space spins in a stochastic manner due to molecular tumbling. In this way a local field is generated within the system of spins which is superimposed upon the main magnetic field B_0 . The nuclei can reside on the same molecular structure or they may be components of different molecules. In any case, there are a great number of ways that nuclei can move around each other so that the strength of the total magnetic field (main and local field) felt by a nucleus varies randomly in time. As it was mentioned before, correlation time t_c characterizes the molecular tumbling. So it is obvious that as t_c becomes smaller, the strength of the local magnetic field, B_{loc} , will fluctuate to a greater degree (figure 5)

In quantitative manner, the transverse and the longitudinal component of the local field, generated by one spin at the other, is given by the following expression:¹

$$B_z \sim \frac{(3 \cos(\theta)^2 - 1)}{r^3} \quad (4)$$

$$B_{xy} \sim \frac{\sin \theta \cdot \cos \theta}{r^3} \quad (5)$$

where θ is the angle between the main magnetic field B_0 and the vector connecting the two centres of the two nuclei and r is the distance between spins. (figure 6)

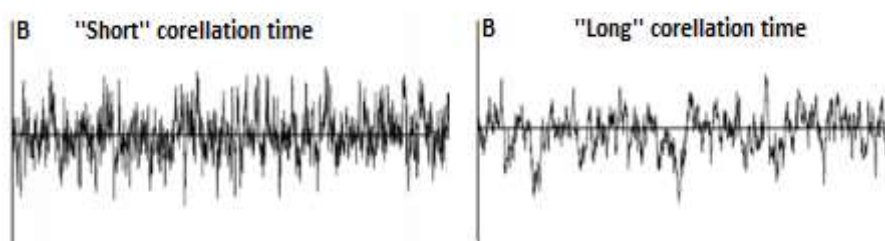


Figure 5: Magnitude of local magnetic field, B_{loc} , over time for "short" and "long" correlation time.

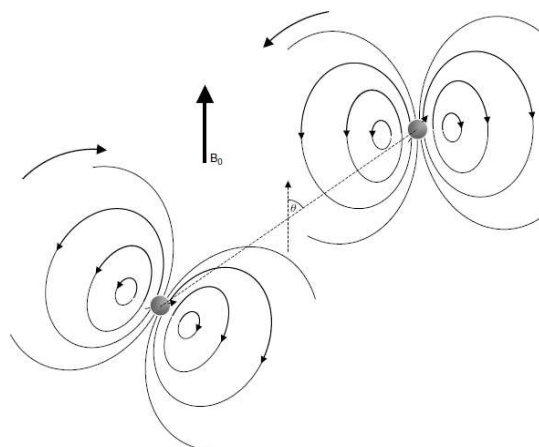


Figure 6: Two magnetic moments, in the presence of the main magnetic field, B_0 , interact with each other so that the transverse component of the local magnetic field, B_{xy} , each one experiences is modified according to their relative motion in space.¹

1.2.2.5 Autocorrelation function

As it was previously stated the local magnetic field produced at one nucleus by its neighboring magnetic nuclei which undergo Brownian motion varies randomly over time. The frequency distribution of the local fluctuating magnetic fields is defined as the spectral density function, $J(\omega)$.^{1,5} T1 relaxation will be induced if the molecular tumbling (and so the fluctuating local magnetic field) has a large component of motion at exactly the Larmor frequency, ω_0 .^{5,8} One way to characterize this random movement is its correlation time and its associated spectral density function.^{2,10} Another way to quantitatively characterize the frequency components of these random fluctuations, is the autocorrelation function, $G(\tau)$ ($\tau = t_2 - t_1$, where t_2, t_1 are two different points in time).¹ Autocorrelation is a real function, independent of t and acts as a correlation coefficient between the same variable (strength of local magnetic field) at different time in points. In simple terms, $G(\tau)$ describes how well coupled the local magnetic field is to itself as time τ progresses.^{1,4,5} The autocorrelation function takes an exponential form according to the following relationship:¹

$$G(\tau) = e^{\left(\frac{-\tau}{\tau_c}\right)} \quad (6)$$

where τ_c is the correlation time.

For small time separations or small values of τ the amplitude and the orientation of the local magnetic field is almost the same, so the value of $G(\tau)$ is large (i.e. high correlation). It is reasonable to assume that correlation diminishes for long values of τ due to molecular tumbling. Correlation time, τ_c , can be interpreted as a constant that determines the rate of decay. For short τ_c (eg for mobile spins in solution, $\tau_c \sim 10^{-12} \text{ s}$)^{2,4} the local magnetic field is extremely altered (rapid fluctuations over time) and $G(\tau)$ goes to zero fast (loss of correlation). For long τ_c (eg for immobile spins in solids or in high viscosity liquids, $\tau_c \sim 10^{-8} \text{ s}$)⁴ the reverse happens (figure 7).

Fourier transform of the autocorrelation function leads to the spectral density function, $J(\omega)$. Thus we can express $J(\omega)$ as follows:^{1,5,6}

$$J(\omega) = \frac{\tau_c}{1 + \omega^2 \tau_c^2} \quad (7)$$

It should be noted that equation (7) is valid for isotropic random motion.⁴ As mentioned earlier slow molecular motion (long τ_c) emphasize low frequency components (narrow spectrum) while fast thermal motion (short τ_c) emphasize high frequency components (broad spectrum).^{2,4,5} Apparently, molecules with short τ_c (figure 8-green curve, $\frac{1}{\tau_c} \gg \omega_0$) will have frequency contributions with relatively small amplitude above the Larmor frequency. Molecules with longer τ_c (Figure 8-red curve, $\frac{1}{\tau_c} \sim \omega_0$) would have a larger frequency component near or at Larmor frequency. So in the latter case where the movement is more restricted relaxation would occur more quickly. As τ_c becomes longer (Figure 8-blue curve, $\frac{1}{\tau_c} \ll \omega_0$) the motion has almost zero power near or at Larmor frequency.^{1,2,8}

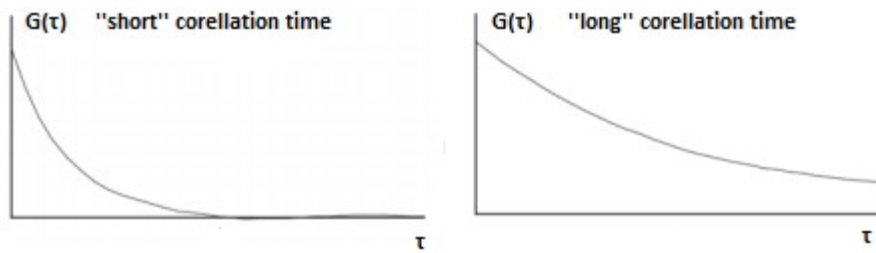


Figure 7: Autocorrelation function, $G(\tau)$, for “short” and “long” correlation time, τ_c . For small values of τ_c , $G(\tau)$ vanishes more rapidly over time separation τ compared to higher values of τ_c .

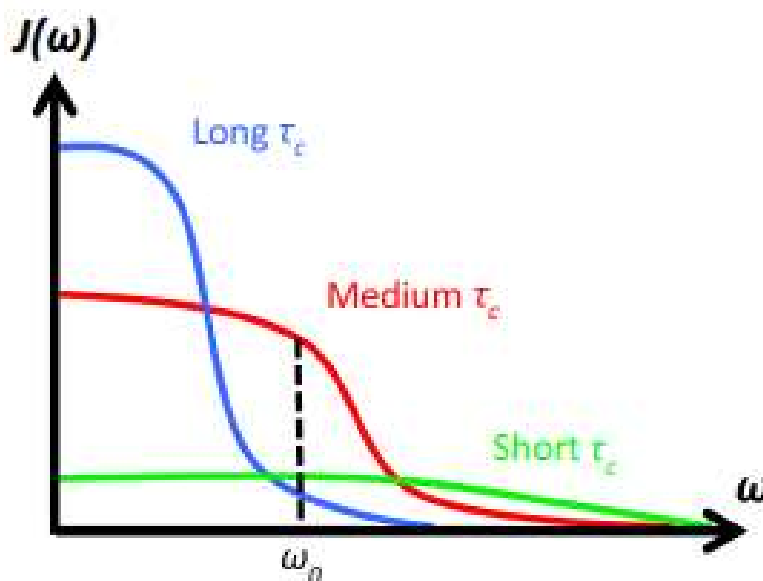


Figure 8: Spectral density function, $J(\omega)$, as a function of resonance frequency, ω for three different correlation times, τ_c . As τ_c increases and molecular tumbling becomes slower, the amplitude of the motion component at the Larmor frequency, $J(\omega_0)$, decreases.¹¹

1.2.3 Expressions of the relaxation times T1 and T2

As it was previously mentioned, relaxation results from the interaction of nuclear spin system with fluctuating local magnetic fields. The resultant magnetic field experienced by a spin is the superposition of the constant magnetic field, B_0 , and the local magnetic field, B_{loc} , which randomly changing over time and acts as a small perturbation. The mechanism which leads to relaxation of the system depends on the origin of these magnetic fields. Also, they may arise from the magnetic moment of neighboring nuclei which can reside on the same molecule with the spin of interest (intramolecular dipole-dipole interaction) or it can reside on a different molecule (intermolecular dipole-dipole interaction). In this case the specific source of the fluctuating magnetic fields leads to a particular relaxation mechanism. Thus different relaxation processes (i.e. scalar relaxation and nuclear dipole-dipole

relaxation, paramagnetic relaxation etc) result in different set of equations of T1 and T2 relaxation time.

As a first approximation, an ideal but not realistic relaxation mechanism is introduced, the so-called "random fields model". In this simple approach which can be considered as a simplified version of nuclear dipole-dipole relaxation, a general set of T1 and T2 equations can be derived.¹¹ In physically more realistic situation, where nuclear spins are relaxed through a particular relaxation mechanism, adjustments or corrections on these relationships must be made. According to this model spins are subject to local magnetic field whose source is the random thermal motion of molecules. Also it is assumed that nuclear spins are relaxed independently of each other via these magnetic field fluctuations.¹² In addition molecules tumble in an isotropic fashion. For all the above, relationships between the components of the total magnetic field in a seen by a proton in the laboratory frame are given below:

$$\vec{B} = B_0\vec{z} + B_x(t)\vec{x} + B_y(t)\vec{y} + B_z(t)\vec{z} \quad (8)$$

In equation (8) B_0 is the magnitude of the static main magnetic field. $B_x(t)$ and $B_y(t)$ represent the time dependent transverse components of the local fluctuating magnetic field and of course $B_z(t)$ is the longitudinal component. Due to isotropic molecular tumbling the various components of the field are equal. So :¹¹

$$\langle B_x^2 \rangle = \langle B_y^2 \rangle = \langle B_z^2 \rangle = \langle B^2 \rangle \quad (9)$$

Where $\langle B^2 \rangle$ is the mean square value of the local magnetic field. Finally, according to this simple model the longitudinal relaxation rate ($\frac{1}{T_1}$) of the spin system back to equilibrium state follows the following relationship:^{11,12}

$$\frac{1}{T_1} = K \cdot \langle B^2 \rangle \cdot J(\omega) \quad (10)$$

In the above equation K is constant and $J(\omega)$ is the spectral density function of the molecular tumbling. It is assumed that autocorrelation function $G(\tau)$ has a simple exponential form with decay constant τ_c . Thermal motion has a short range correlation. So the Fourier transform of $G(\tau)$ which is $J(\omega)$ ¹ is given by the equation (6). In that case ,equation (10) can be written as:¹¹

$$\frac{1}{T_1} = \gamma^2 \cdot (\langle B_y^2 \rangle + \langle B_x^2 \rangle) \cdot J(\omega) \quad (11)$$

Where γ is the gyromagnetic ratio of the spin. As it can be seen from equation (11) only fluctuations in the transverse plane lead to spin-lattice relaxation.^{1,11}

According to this idealized relaxation mechanism, the expression of the transverse relaxation rate ($\frac{1}{T_2}$) is given below:¹¹

$$\frac{1}{T_2} = \gamma^2 \cdot (\langle B_z^2 \rangle \cdot \tau_c + \langle B_y^2 \rangle \cdot J(\omega)) \text{ and } J(0) = \tau_c \quad (12)$$

From equations (11) and (12) it is obvious that the longitudinal component of the local field contributes only to relaxation of the transverse relaxation.^{1,11}

Even with this approximate model of relaxation, predictions about the variation of T1 and T2 relaxation time with correlation time τ_c and angular frequency ω can be made.

For rapid molecular tumbling in liquids (protons in water molecules) where $\omega \cdot \tau_c \ll 1$ and $J(\omega) \approx \tau_c$ so that T1 and T2 are proportional to $\frac{1}{\tau_c}$.

$$\frac{1}{T_1} = \frac{1}{T_2} \propto \tau_c \quad \text{for } \omega \cdot \tau_c \ll 1 \quad (13)$$

From equation (13) relaxation becomes more efficient (smaller values of T1 and T2) as τ_c increases and vice versa. As will be explained later, correlation time, τ_c , is increased or reduced by lowering and raising the temperature respectively.

For slow molecular tumbling in solids or in liquids with high viscosity, $\omega \cdot \tau_c \gg 1$ and $J(\omega) \approx \frac{1}{\omega^2 \tau_c}$. In that case, T1 and T2 relaxation rates are given below.

$$\frac{1}{T_1} \propto \frac{1}{\tau_c} \quad \text{for } \omega \cdot \tau_c \gg 1 \quad (14)$$

$$\frac{1}{T_2} \propto \tau_c + \frac{1}{\omega^2 \tau_c} \quad \text{for } \omega \cdot \tau_c \gg 1 \quad (15)$$

Clearly from equation (14) T1 relaxation becomes slower as τ_c is increased and vice versa. In contrast, T2 relaxation becomes more efficient as τ_c increases.

T_1^{-1} goes through a maximum or in other words T1 relaxation is most efficient when molecular tumbling rate ($\frac{1}{\tau_c}$) matches the Larmor frequency (so $\omega = \omega_0$). Specifically when:^{1,11}

$$\omega_0 \cdot \tau_c \sim 1 \quad (16)$$

The same result can be obtained by differentiating equation (6) with respect to τ_c and for fixed ω and equal to the resonance frequency of the spins.

Considering all the above, the variation of spin-lattice relaxation rate T_1^{-1} and spin-spin relaxation rate T_2^{-1} with correlation time, τ_c , is shown in Figure 9.

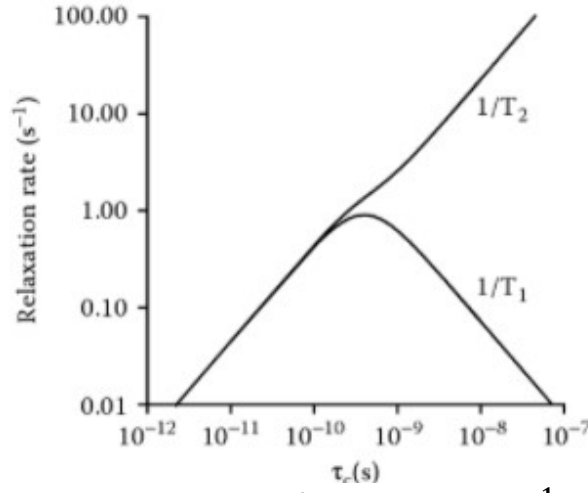


Figure 9 : Dependence of relaxation rates T_1^{-1} and T_2^{-1} on correlation time, τ_c . The value of ω is fixed and equal to the Larmor frequency, ω_0 for protons and $B_0 = 9.4 \text{ T}$. T_1^{-1} goes through a maximum when $\tau_c \sim \frac{1}{\omega_n}$.

Although there are many mechanisms that contribute to T1 and T2 relaxation, the dominant process among them for protons is nuclear dipolar relaxation.¹ From equations (4) and (5) direct dipole-dipole interaction between two magnetic nuclei depends on their internuclear separation, r and on angle θ . These parameters are affected by the relative motion of the dipolar pair. Therefore, rapidly fluctuating dipole interactions take place due to molecular thermal motion. Thus, the local magnetic field produced at one magnetic active nucleus by other adjacent nuclei becomes time dependent and varies randomly. Moreover, for this particular mechanism the two dipolar-coupled spins are not independent of each other.¹¹ They relax in a correlated fashion. This mutual interaction between the spins lead to T1 and T2 relaxation.

Bloembergen et al explained how a system of identical magnetic moments returns back to thermal equilibrium though random Brownian molecular motion. Also, they derived approximate expressions for T1 and T2 relaxation time for protons in various homogeneous liquids (water, ethyl alcohol, glycerol etc). The seminal work of Bloembergen et al was the first to emphasize the importance contribution of dipolar interaction to T1 and T2 relaxation. A more complete derivation of T1 and T2 relaxation rate was given by Solomon whose work is based on BPP theory.^{6,7}

Dipolar interaction between two nuclear spins can be intermolecular and intramolecular. In the case of intramolecular interaction, relaxation rates T_1^{-1} and T_2^{-1} for a pair of identical spins ($i_1 = i_2 = i$) can be expressed in terms of τ_c , γ and ω according to the following relationships:^{7,11}

$$\left(\frac{1}{T_1}\right)_{intr} = \frac{2 \cdot \hbar^2 \cdot \gamma^4 \cdot i(i+1)}{5 \cdot r^6} \cdot \left(\frac{\tau_c}{1 + \omega^2 \cdot \tau_c^2} + \frac{4 \cdot \tau_c}{1 + 4 \cdot \omega^2 \cdot \tau_c^2} \right) \quad (17)$$

and

$$\left(\frac{1}{T_2}\right)_{intra} = \frac{2 \cdot \hbar^2 \cdot \gamma^4 i(i+1)}{5 \cdot r^6} \cdot \left(3 \cdot \tau_c + \frac{5 \cdot \tau_c}{1 + \omega^2 \cdot \tau_c^2} + \frac{2 \cdot \tau_c}{1 + 4 \cdot \omega^2 \cdot \tau_c^2} \right) \quad (18)$$

Where r is the internuclear distance

When molecular motion is rapid so the condition $\omega \cdot \tau_c \ll 1$ is met then

$$\left(\frac{1}{T_1}\right)_{intra} = \left(\frac{1}{T_2}\right)_{intra} = \frac{2 \cdot \hbar^2 \cdot \gamma^4 i(i+1)}{r^6} \cdot \tau_c \quad \text{for } \omega \cdot \tau_c \ll 1 \quad (19)$$

For fixed internuclear distance T_1 and T_2 are equal and proportional to the correlation time. The same conclusion can be drawn from the equation (13) where a different relaxation mechanism was used.

For protons, substituting $i = 1/2$ in equations (17) and (18) gives

$$\left(\frac{1}{T_1}\right)_{intra} = \frac{6}{20} \cdot \frac{\hbar^2 \cdot \gamma^4}{r^6} \cdot \left(\frac{\tau_c}{1 + \omega^2 \cdot \tau_c^2} + \frac{4 \cdot \tau_c}{1 + 4 \cdot \omega^2 \cdot \tau_c^2} \right) \quad (20)$$

and

$$\left(\frac{1}{T_2}\right)_{intra} = \frac{3}{20} \cdot \frac{\hbar^2 \cdot \gamma^4}{r^6} \cdot \left(3 \cdot \tau_c + \frac{5 \cdot \tau_c}{1 + \omega^2 \cdot \tau_c^2} + \frac{2 \cdot \tau_c}{1 + 4 \cdot \omega^2 \cdot \tau_c^2} \right) \quad (21)$$

The same equations can be rewritten in a different form using equation (7):⁷

$$\left(\frac{1}{T_1}\right)_{intra} = \frac{6}{20} \cdot \frac{\hbar^2 \cdot \gamma^4}{r^6} \cdot (J(\omega) + 4 \cdot J(2\omega)) \quad (22)$$

$$\left(\frac{1}{T_2}\right)_{intra} = \frac{3}{20} \cdot \frac{\hbar^2 \cdot \gamma^4}{r^6} \cdot (3 \cdot J(0) + 5 \cdot J(\omega) + 2 \cdot J(2\omega)) \quad (23)$$

For example, equations (20) and (21) predict T_1 and T_2 values for hydrogen nuclei in a water molecule which undergoes random translational and rotational motion. It is always assumed that only intramolecular interactions take place.

As it was already stated, the rate of relaxation driven by dipolar interaction is inversely proportional to the sixth power of distance between the magnetic nuclei. Therefore the contribution of intermolecular interaction to relaxation can be neglected. Bloembergen et al calculated the longitudinal relaxation rate for protons in water due to intramolecular and intermolecular interaction. It was concluded that intramolecular interactions are more effective in inducing relaxation than intermolecular interactions between water molecules.⁶

From equations (22) and (23), the term $J(2\omega)$ corresponds to the component of the motion which depends on twice the angular frequency. This component of motion generates local magnetic fields oscillating with a frequency equal to twice the Larmor frequency ($2\omega = 2\omega_0$) so that double quantum transitions can happen.^{5,8} This process results in T_1 relaxation but also affects the transverse components of individual spins (dephasing) so that T_2 relaxation can take place. In general any process that results in both T_1 and T_2 relaxation is known as "non-secular" T_1 contribution to T_2 .¹

The term $J(0)$ (static spectral density) corresponds to the static component of the local magnetic field which can induce only T2 relaxation.¹ Zero quantum transition where both spins simultaneously flip in opposite energy state results only in T2 relaxation.¹¹ This process has a probability of happening which is proportional to the term $J(0)$. Both (22) and (23) equations contain $J(\omega)$ and $J(2\omega)$. Hence, these terms correspond to "non-secular" T1 contribution to T2. In contrast, only equation (10) contains $J(0)$. So this term corresponds to "secular" contribution to T2.¹

In conclusion, oscillating magnetic fields at frequencies of ω_0 and $2\omega_0$ induce longitudinal relaxation. On the other hand, magnetic field components that oscillate at frequencies $0, \omega_0, 2\omega_0$ contribute to transverse relaxation.⁸ Therefore, T2 relaxation time is less than or equal to T1 relaxation time.^{1,11}

Figure 10 gives a graphical depiction of equations (22) and (23) for a given value of ω ($\omega = \omega_0$, where ω_0 is the Larmor frequency of the spin system).

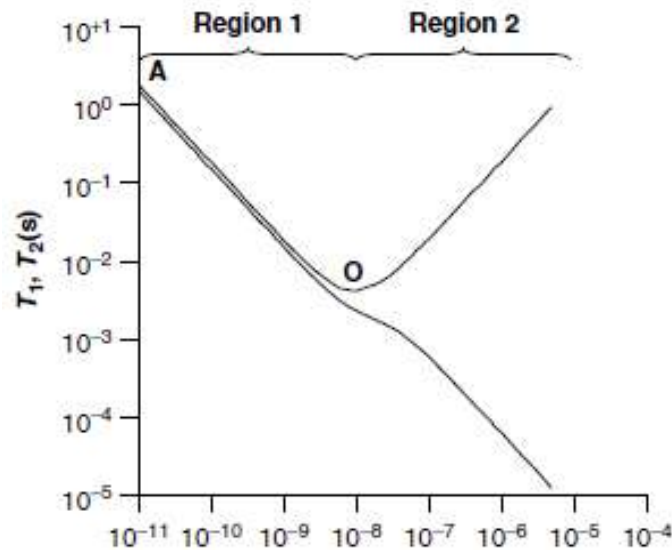


Figure 10 : T1 (black line) and T2 (grey line) relaxation time as a function of correlation time, τ_c . The minimum (point O) in T1 occurs when $\omega_0 \cdot \tau_c \sim 1$.¹¹

The classic plot of T1 and T2, as it can be seen from figure 10, is consisted of two distinct regions according to the dimensionless parameter. $\omega \cdot \tau_c$. Region 1 from point A to point O, $\omega \cdot \tau_c \ll 1$ which corresponds to rapid molecular tumbling (non viscous liquids). In this limit T1 relaxation time is relatively long and is equal to T2 relaxation time. Again, for $\omega \cdot \tau_c \ll 1$ equations (20) and (21) are simplified and they can be rewritten as follows:¹¹

$$\frac{1}{T_1} = \frac{1}{T_2} = \frac{3}{2} \cdot \left(\frac{\hbar^2 \cdot \gamma^4}{r^4} \right) \cdot \tau_c \quad (24)$$

In region 1 T1 relaxation time is long because the probability to find a component of the molecular motion near or at Larmor frequency is low (see figure 8-blue curve). Also, the rapid fluctuations in the local magnetic field experienced by a spin average out ($B_{loc} \sim 0$) due to fast molecular tumbling.^{1,2} This is sometimes referred as motional averaging or motional narrowing.⁵ In that case the magnetic field in the molecular environment of a spin is homogeneous so that loss of phase coherence between adjacent spins cannot occur.² This result in long values of T2 relaxation time. In conclusion fast molecular motion results in long values of T1 and T2 relaxation times.

Moving along the curves from point A to point O, τ_c increases T1 decrease simultaneously with T2. The separation between the 2 regions is the point O where T1 relaxation time is minimum and T2 keeps decreasing. In this intermediate region (approximately from $\tau_c = 10^{-9}s$ to $\tau_c = 10^{-8}s$) $\omega \cdot \tau_c \sim 1$ which correspond to intermediate molecular motion (viscous liquids). T1 relaxation is most efficient in this region because the threshold frequency, $\frac{1}{\tau_c}$, of the molecular motion is approximately equal to Larmor frequency. This means that intermediate molecular tumbling has a large component of motion at the Larmor frequency (see figure 8-red curve). In this way the transverse component of the local magnetic field experienced by a spin oscillates at the appropriate frequency so that transitions between spin states can be induced. Minimum of T1 relaxation time is given from equation (20) for $\omega \cdot \tau_c \sim 1$. From equation (25) it is clear that the minimum of T1 is a value that is depended on magnetic field strength B_0 .^{1,5} Moreover, when T1 relaxation time passes through a minimum, T2 relaxation is affected indirectly (T1 "non secular" contribution to T2) and reaches a "plateau". This happens because, according to equations (22), (23) both T1 and T2 are depended on the term $J(\omega_0)$ which is maximum when $\omega \cdot \tau_c \sim 1$ (see figure 8-red curve). In this case:¹

$$\frac{1}{T_1} \propto \frac{1}{\omega_0}, \omega_0 = \gamma \cdot B_0 \quad (25)$$

In region 2, $\omega \cdot \tau_c \gg 1$ which corresponds to restricted molecular tumbling (rigid solids). The region 2 is characterized by the divergence of T1 and T2 relaxation times. Particularly, T1 relaxation time is constantly increasing because the probability to find dipolar magnetic field oscillating at exactly the Larmor frequency is extremely small (see figure 8-blue curve) so that T1 relaxation is inefficient (long T1 values). In short, when $\omega \cdot \tau_c \gg 1$ then $J(\omega_0) \sim 0$ and thus from equation (22) where $T_1 \approx \frac{1}{J(\omega_0)} + \frac{1}{4J(2\omega_0)}$, T1 relaxation time has relatively long values. In contrast, T2 relaxation time constantly decreasing. This can be explained from equation (23) and from figure 8 (blue curve) where $J(\omega_0) \sim 0$ and $J(2\omega_0) \sim 0$ but $J(0) \neq 0$. Specifically, as τ_c increases and molecular tumbling gradually slowing down, the local magnetic field experienced by a spin fluctuate less and less so that it can be considered

relatively static over time. As solid state is approached, the longitudinal component of the static local field generated by a spin cause the loss of phase coherence between the transverse components of individual magnetic moments. This static magnetic “inhomogeneity” results in a large variation in precessional frequencies of spins and T2 relaxation takes place. ²Apart from that, T2 continues decreasing in a linear fashion as τ_c increases. Consequently, low oscillating or static magnetic fields are most effective at inducing T2 relaxation. ^{1,4}

1.2.4. Temperature dependence of T1 and T2 relaxation time.

In the case of an isotropic random motion, a quantitative description of correlation time is given by the following relationship: ⁶

$$\tau_c = \frac{4 \cdot \pi \cdot \eta \cdot a^3}{k \cdot T} \quad (26)$$

k is Boltzman’s constant and T is the absolute temperature. Molecule is treated as a sphere of radius a which undergoes Brownian motion in a liquid medium. η is the viscosity of the liquid. As it can be seen from equation (26), temperature affect τ_c in two ways. Viscosity, η , in the numerator varies with change in temperature. If η is nearly constant with respect to temperature (e.g. water) then τ_c is inversely proportional to the temperature. However in the general case τ_c is depended on both η and T in equation (26).

Assuming an Arrhenius - type temperature dependence of the viscosity: ⁴

$$\eta = \eta_0 \cdot e^{\frac{E_a}{k \cdot T}} \quad (27)$$

E_a is the activation energy and η_0 is a constant without physical significance. The exponential factor and not the term $1/T$ determines the dependence of τ_c on T .

So substituting η from equation (27) to equation (26) gives

$$\tau_c = \tau_o \cdot e^{\frac{E_A}{k \cdot T}} \quad (28)$$

Where τ_o is a constant again without physical significance. ⁴ Assuming that correlation time is depended only on temperature and does not depend on ω_o , τ_c on figure 10 can be substituted directly by the factor $\frac{1}{T}$.

According to equation (28) τ_c inversely proportional to temperature T . This means that increasing the temperature cause reduction in the value of correlation time. Besides that temperature T is directly proportional to the mean kinetic energy of the molecules that undergo Brownian motion. So as τ_c decreasing, the molecular Brownian motion becomes more vivid so that the range of frequency components that constitute the motion becomes larger (broad spectrum). Since the area under

spectral density function, $J(\omega)$, is constant, the amplitude of the motion components at higher frequencies increases and at lower frequencies decreases.⁸ Thus, as molecular motion becomes more rapid, the amplitude of the motion components at frequencies ω_0 and 0 (i.e. $J(\omega_0)$, $J(0)$) drops off quickly (see Figure 8).

For better understanding of how temperature affect T1 and T2 relaxation times, spectral density function of three types of molecular motion (a, b, c) is depicted in the following diagram (figure 11). In addition, for each type of molecular motion, its associated spectral density function is depicted for two different temperatures (T' , T and $T' > T$).

As it was stated before, increasing of the temperature leads to an increase in the range of frequencies that make up the molecular motion. This means that for a particular value of τ_c , the amplitude of frequency components below the threshold frequency, $\frac{1}{\tau_c}$, will be reduced significantly. So as T increases, $J(0)$ continuously reducing and T2 relaxation becomes less efficient (longer T2 values). However, change in temperature affect T1 relaxation time in a different way. From equations (20), (21) and for a given magnetic field $B_0(\omega = \omega_0)$, T1 relaxation time depends directly on the parameter $\omega_0 \cdot \tau_c$ and indirectly on the temperature according to equation (28). In liquids with low viscosity, where $\omega_0 \cdot \tau_c \ll 1$ (rapid molecular tumbling), an increase in temperature leads to a decrease in the value of correlation time τ_c . The amplitude of the motion component at frequency ω_0 , reduces (Figure 11c) and as a result, T2 relaxation time increases in accordance with equation (9) for $\omega = \omega_0$. Of course the same result can be obtained from Region 1 in figure 10 as τ_c decreases. In solids or in liquids with high viscosity, where $\omega_0 \cdot \tau_c > 1$ or $\omega_0 \cdot \tau_c \gg 1$ (slow molecular tumbling) the reverse happens as temperature increases. In particular T1 reduces because $J(\omega_0)$ increases (Figure 10a) and T1 relaxation becomes more efficient. Similarly as before, the same conclusion can be made from Region 2 in figure 10 as τ_c decreases. Lastly, a combination of ω_0 and T (or τ_c) leads to maximum value of $J(\omega_0)$ (intermediate molecular tumbling, Figure 10 b) and T1 is minimum (Point 0 in figure 10). From this point, further increase or reduction in temperature (reduction or increase in the value of correlation time, τ_c , respectively) leads to an increase in T1 relaxation time.

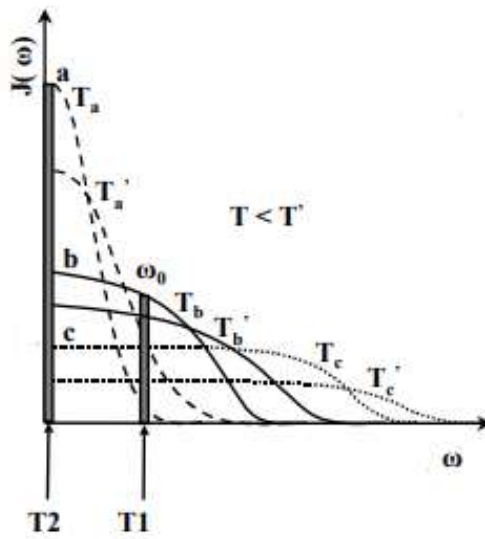


Figure 11: Spectral density function, $J(\omega)$ of rapid (c), intermediate (b) and slow (a) molecular tumbling. For each case, the graph of $J(\omega)$ is given at two different temperatures T and T' ($T' > T$). T_2 relaxation is affected by changes in the value of $J(\omega)$ at zero frequency ($J(0)$). T_1 relaxation is affected by changes in the value of $J(\omega)$ at Larmor frequency ($J(\omega_0)$).⁴

Considering all the above, equations (20), (21) and (28) show the primary temperature dependence of T_1 and T_2 relaxation time. For the frequency and temperature range used in clinical MRI it can be concluded that the condition stated by the equation (13) or (19) is met.¹³ Particularly, for liquids of very low viscosity (such as water) and in the liquid temperature range the value of dimensionless parameter $\omega_0 \cdot \tau_c$ is always much less than 1 ($\omega_0 \cdot \tau_c \ll 1$). Hence, according to equation (13) or (19) T_1 and T_2 are independent on the Larmor frequency, ω_0 , and they are inversely proportional to correlation time ($T_1 = T_2 \propto \frac{1}{\tau_c}$). In pure water $\tau_c < 10^{-11} s^2$ so that the average molecular tumbling frequency, $\frac{1}{\tau_c}$, is much higher than the Larmor frequency at frequency range normally used in MRI. In addition the viscosity, η , of water can be considered constant as temperature varies. From equation (26) for constant η , τ_c is also inversely proportional to temperature ($\tau_c \propto \frac{1}{T}$). So in the temperature range where water stays in liquid state ($0 - 100^\circ C$), T_1 and T_2 are directly proportional to temperature.

The relaxation times T_1 and T_2 as a function of the reciprocal absolute temperature for a homonuclear two spin system, when their temperature dependency can be described by the simple relationship (28), is shown below. It is assumed that strength of the main magnetic field experienced by the spins is 0.5 Tesla. So the Larmor frequency of the spin system is equal to 133MHz.⁴

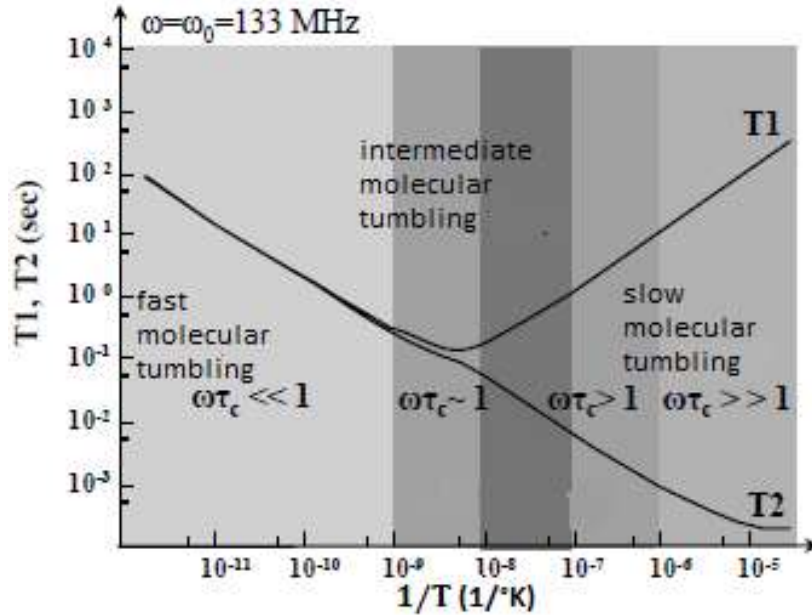


Figure 11 : The T1 and T2 relaxation times as a function of reciprocal absolute temperature ($1/T$). For short values of τ_c (fast molecular tumbling) T1 and T2 are about equal with each other. Also, they are independent of ω_0 , depending mainly on τ_c which is inversely proportional to T . Thus in this region, there is a linear relationship between T1 and T2 relaxation times and temperature ($T_1 = T_2 \propto T$).⁴

1.2.5. Temperature dependence of proton density (PD)

Proton density refers to the concentration of the protons that resonate during excitation and gives rise to NMR signal or creates the net magnetization M . Before any RF pulse is applied, the spin system reaches a state of thermal equilibrium. The temperature of the system is a measure of the average kinetic energy.⁸ That is to say, the rate of thermal collisions that tend to equalize the two energy states is increased by raising the temperature. However, in equilibrium spins tend to point with the main field direction or reside in lower energy, so that the total energy of the spin system is minimized.^{1,2,4} So thermal motion opposes the alignment of the spins with the main magnetic field state. The resultant ratio of spins in the parallel direction (low energy state) to spins in the antiparallel direction (high energy state) with respect to the main magnetic field, B_0 , is given by the Boltzmann distribution.^{1,2,4,13}

$$\frac{n_+}{n_-} = e^{\frac{\Delta E}{k \cdot T}} = e^{\frac{\gamma \cdot \hbar B_0}{k \cdot T}}, \Delta E = \gamma \cdot \hbar \cdot B_0 \quad (29)$$

n_+ is the population of low energy state, n_- is the population of high energy state, ΔE is the energy difference between low and high energy state, k is the Boltzmann constant and T is the absolute temperature in degrees Kelvin. From (29) it is clear that the ratio is depended on B_0 and T . For a given value of B_0 , the ratio and T have an inverse relationship. As temperature increases, the number of spins in low energy state decreases and vice versa.

For the field strengths and temperatures used in clinical MRI, $\Delta E \ll k \cdot T$. So as an approximation equation (29) can be written as:^{2,13}

$$\frac{n_+}{n_-} \approx 1 + \frac{\gamma \cdot \hbar \cdot B_0}{k \cdot T} \quad (30)$$

The population difference, Δn , is given by the following relationship:^{1,2}

$$\Delta n \approx n_+ - n_- = \frac{n_+ \cdot \gamma \cdot \hbar \cdot B_0}{k \cdot T} \quad (31)$$

Δn is the population difference between the two energy states creates the net magnetization, M which is oriented along the axis of the main magnetic field, B_0 (figure 1). Moreover equation (31) can be written in a different form :^{1,2}

$$\Delta n \approx n_+ - n_- = \frac{N \cdot \gamma \cdot \hbar \cdot B_0}{2 \cdot k \cdot T}, N \approx 2 \cdot n_+ \quad (32)$$

In the previous equation N is the total number of spins and is a constant number.

At thermal equilibrium the macroscopic magnetization is proportional to this net difference and scales inversely proportional to the absolute temperature corresponding to Curie's law.^{1,2,13}

$$M \approx \Delta n \cdot \mu = \frac{N \cdot \gamma^2 \cdot \hbar^2 \cdot B_0}{4 \cdot k \cdot T} = \chi \cdot B_0, \mu = \frac{1}{2} \cdot \gamma \cdot \hbar \text{ and } \chi = \frac{N \cdot \gamma^2 \cdot \hbar^2}{4 \cdot k \cdot T} \quad (33)$$

μ is the magnitude of the proton magnetic moment and χ is the magnetic susceptibility.

Using the definition of the magnetic susceptibility, equation can be rewritten as follows:^{1,2,13}

$$\Delta n \approx \frac{\gamma \cdot \hbar \cdot B_0}{2} \cdot \chi \quad (34)$$

So according to equation (34), for a given magnetic field strength Δn is proportional to the magnetic susceptibility ($\Delta n \propto \chi$).

From equation (33), for a given value of B_0 , M is inversely proportional to the temperature T . The fractional change in M with respect to T is approximately given by the following relationship:¹³

$$\frac{\Delta M}{\Delta T} \approx -N \frac{\gamma^2 \cdot \hbar^2 \cdot B_0}{4 \cdot k \cdot T^2} \quad (35)$$

It must be pointed out that the actual proton density in the biological tissue is constant with respect to temperature. As it was mentioned before, the term proton density refers to the number of protons that contribute to the formation of the NMR signal. Thus, the term proton density (PD) refers to the difference in population between the energy states, Δn .¹³

So from equation (34) it can be concluded that any changes in temperature will affect the actual proton density of the spin system but they will affect χ (Curie's law) and of course Δn .^{1,2,13} However, from equation (33) it is obvious that Δn or PD is

directly proportional to M and it will have the same temperature dependence ($M \propto 1/T$) or fractional change as $M(\frac{\Delta M}{M} \propto -\frac{1}{T^2})$. In short:¹³

$$PD \propto M \approx \frac{N \cdot \gamma^2 \cdot \hbar^2 \cdot B_0}{4 \cdot k \cdot T} = \chi \cdot B_0 \quad (36)$$

1.3 Introduction to MRI sequences

1.3.1 Single or Conventional Spin echo (SE) sequence

It consists of 90 and 180 degree RF pulses. The 90 degree RF pulse is the excitation pulse and the 180 degree pulse is a refocusing pulse that generates the spin echo. The 180° refocusing pulse is used so that the constant distortions of the static magnetic field can be eliminated.¹ However, the refocusing pulse cannot compensate for the local and field inhomogeneities due to random spin – spin interaction among the spins.² In a spin echo sequence repetition time or TR is the time interval between the application of an 90° pulse to the application of the next excitation pulse.^{4,14} Echo time or TE is the time interval from the excitation pulse until the peak of the signal that is produced.⁴ The major drawback of SE sequence is the long scan time.¹⁵

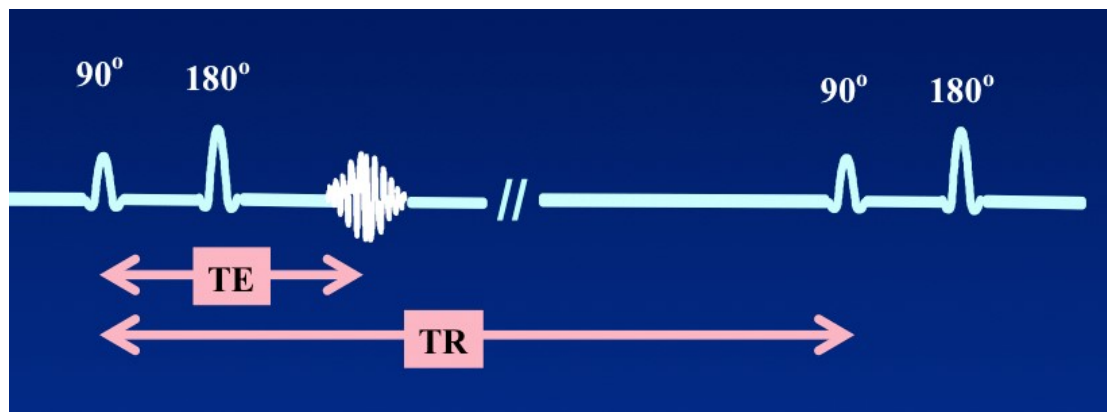


Figure 12 : Time diagram of single spin echo sequence. TR is the repetition time and TE is the echo time is the amount of time from the middle of the excitation pulse to the center of the echo where complete rephasing of MR signal or transverse magnetization occurs.¹⁴

1.3.2. Multi-echo Spin Echo (MESE) sequence

In multi-echo Spin Echo more than one refocusing pulses can be applied to the system of spins. Multiple 180° RF - pulses are applied after the 90 – RF pulse so that a train of spin echoes is formed.⁴ The parameter that regulates the duration of the echo train formation is the T2 relaxation time. The amplitude of echo is progressively smaller as T2 relaxation takes place and the magnitude of the transverse magnetization that can be recovered continuously reducing as time passes.¹ Each echo reforms and decays (Free induction decay - FID) with time constant T_2^* which takes into account inhomogeneities in the static magnetic field.^{14,15} The 180° pulse must be 90° out of phase with respect to the initial excitation pulse. Thereby problems due to inefficient sequential application of 180° can be eliminated.^{1,4} With the amplitude of the echo peaks as a function of time, T2 relaxation time can be estimated. Also, by choosing Inter – Echo Spacing, T_E to be relatively small diffusion

induced shortening of T2 can be neglected.¹ Thus the value of T2 relaxation time can be estimated from the envelope of the echo amplitudes more accurately.

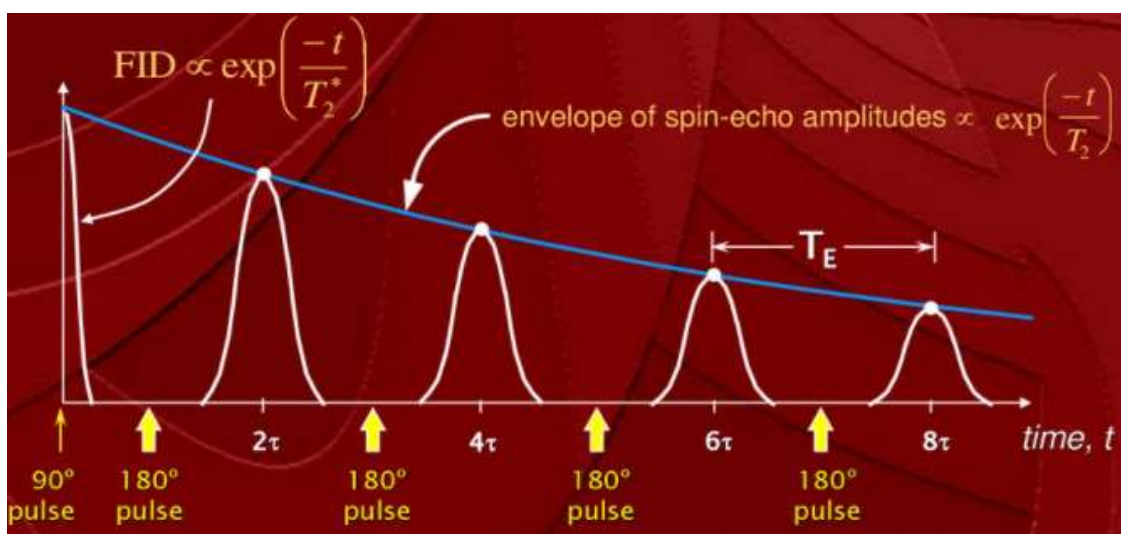


Figure 13 : Time diagram of Multi – Echo Spin Echo sequence. Multiple refocusing or 180° pulses can be used to generate additional echoes. Prior and after the refocusing pulse the signal (FID) decays exponentially at a rate that depends on the T_2^* decay constant. Assuming that T_E is small enough so that diffusion effects can be neglected, the envelope of the sequential echo peaks estimates the value of T2 relaxation time.

1.3.3 HASTE: Half – Fourier Single Shot Turbo Spin Echo sequence

HASTE is a turbo spin echo pulse sequence available on Siemens MRI scanners. At first turbo spin echo (TSE) or fast spin echo (FSE) is a modification of the conventional multi-echo spin echo. The main difference between these two sequences is that in TSE each echo is sampled with different phase encoding value while in multi-echo spin echo the same phase encoding gradient is applied for all the echoes during the TR interval.¹⁵ So during each TR time multiple lines of k space are sampled. In TSE the Inter-echo spacing is always constant cause the time interval between two 180° pulses is fixed. Turbo Spin factor or Echo Train Length (ETL) is the number of lines of k space filled with data from the same number of spin echoes acquired at the same TR time. This factor determines how many times the total scan time is reduced compared to single spin echo sequence. The higher the value of this parameter, the shorter the scan time.²

HASTE might be considered a TSE sequence with the highest value of turbo spin echo (ETL).² However there is a major difference between these two imaging techniques. TSE uses multiple excitation pulses in order to collect all the lines k space and complete the image reconstruction. In contrast, HASTE uses the so called single shot technique so that the entire k space is acquired during only one TR interval.¹⁵ In other words, HASTE uses only one initial excitation pulse followed by the required number of echoes to reconstruct the entire image.¹⁶ So HASTE can be considered as a form of single shot TSE sequence.² This sequence utilizes an additional technique called half - Fourier k space acquisition. This method taking advantage the fact the

Hermitian or conjugate symmetry of k space¹⁵. Thus only a little more than half of k space data must be acquired during TR.¹⁷ The rest of the space can be calculated using k space conjugate symmetry. Hence, HASTE combines a partial Fourier technique with TSE. As a result, HASTE imaging technique generates images in less than one second per slice with high spatial resolution. In clinical routine, the major disadvantages of HASTE sequence is the relatively low signal to noise ratio or SNR¹⁶ due to its long TE values.

1.4 Introduction to image contrast

1.4.1 Image contrast in SE sequence

Depending on the repetition time for a spin echo image, we acquire different contrast. With a low TR (usually lower than 500ms), and low TE, (usually lower than 50ms), we have T1-weighted Image, and with higher TR, and a higher TE, a T2-weighted image is obtained. In T1-weighted image, areas with long T1, appear dark in the T1W-image, whereas areas with short T1, appear brighter in the T1W-image.^{2,18}

On the other hand, if a higher TR, TE, are chosen, that means we have T2-weighted image. In that case, we have areas with long T2, to appear brighter in the T2W-image, and areas with shorter T2, to appear darker in the T2W-image.^{15,18}

Finally, on the other hand for a spin echo image, with a combination of long TR(more than 1500ms), and a short TE (less than 40ms), a Proton Density Image (PD) is acquired, which is related to the number of active signaling.^{15,18}

1.4.2 Image contrast in MESE sequence

As it was previously mentioned, in the same TR period the phase encoding gradient is constant. So for a given TR signal from each TE is recorded at different time and in separate k space. Fourier transform of these k spaces will result in images of the same slice but with different contrast. For instance, the contrast of the image acquired at the first TE is based on proton density since TR is long and TE is short. In the same way the contrast of the second image is based on T2 since the second TE is higher than the first T2. The contrast of sequential images acquired at longer TEs will be more T2 weighted than the contrast of images obtained at earlier TEs. In conclusion, in multi-echo imaging Proton density and T2-weighted images can be obtained simultaneously.^{2,15}

1.4.3 Image contrast in TSE sequence

The echoes are received at different echo times, TEs. The factor that determines which parameter (T1, T2, PD) contributes the most to the image contrast is the effective echo time or effective TE. In TSE with short TR, a minimum effective TE gives T1W image. However, this lowers the value of turbo factor and increases the scan time. For this reason the TSE sequence with long TR and effective TE is used for acquiring T2W images. Finally, high TR and minimum effective TE produces PDW images.^{2,15}

1.4.4 Image contrast in HASTE sequence

In HASTE all k space is filled with data after each TR interval and the next 90° pulse will excite a different slice. So, by definition TR is infinite and images with T1 contrast cannot be obtained in single shot acquisitions. Typically HASTE images are heavily T2W since the majority of lines in the center of k space is filled with data acquired from echoes with long TE.^{15,16}

1.5 Temperature dependence of Electrical Conductivity(EC) in electrolyte solutions

The conductivity of an electrolyte solution illustrates the ability of the solution to conduct an electric current or ions through it. The conductivity or ionic conductivity (in S/m) of the electrolyte solution can be expressed by the following equation:^{19,20}

$$\kappa = \sum n_i \cdot q_i \cdot \mu_i \quad (37)$$

κ , n_i , q_i and μ_i are the conductivity, concentration of charge carriers of ionic species i , charge of species i and mobility of species i , respectively. From equation (37) the total conductivity of the solution is equal to the sum of conductivities of the anions and cations in the solutions (Kohlrausch's law).¹⁹ Simply put, electrical conductivity is a summation of contributions from all the ions present in the solution.

Ion mobility is related to its diffusion coefficient, D_i , by the Einstein relation:¹⁹

$$\mu_i = \frac{q_i \cdot D_i}{k \cdot T} \quad (38)$$

Also concentration, n_i is given by the following relationship:

$$n_i = N_A \cdot c_i \cdot \nu_i \quad (39)$$

c_i is the concentration of the ions, N_A is the Avogadro number and ν_i is the number of ions per formula of the electrolyte.

Substituting (38) and (39) into (37), the Nernst-Einstein relation is obtained:^{19,21}

$$\kappa = \sum \nu_i \cdot c_i \cdot D_i \cdot z_i^2 \cdot N_A \cdot \frac{e^2}{k \cdot T} \quad (40)$$

z_i is the valency of the ion.

The relation between the diffusion coefficient and the viscosity η is given by the Stokes –Einstein equation:^{19,21}

$$D_i = \frac{k \cdot T}{6 \cdot \pi \cdot \eta(T) \cdot r_i} \quad (41)$$

r_i is the effective radius of the diffusing ion and $\eta(T)$ is the solvent viscosity which is dependent on temperature.

Inserting (41) into (40) leads to

$$\kappa = \sum v_i \cdot c_i \cdot z_i^2 \cdot N_A \cdot \frac{e^2}{6 \cdot \pi \cdot r_i \cdot \eta(T)} = constant \cdot \frac{1}{\eta(T)} \quad (42)$$

When water is the solvent, the viscosity over its entire liquid temperature range is given by the following expression with error less than 1 per cent:²²

$$\frac{\eta_{20}}{\eta(T)} = 10^{A/B} = e^{\frac{A}{B} \ln(10)} \approx \left(1 + \frac{A}{B} \cdot \ln(10)\right) \quad (43)$$

$$A = 1,37023 \cdot (T - 20) + 8,36 \cdot 10^{-4} \cdot (T - 20)^2, \quad B = 109 + T \quad (44)$$

T is the temperature in degrees Celsius and η_{20} is the viscosity of water in 20 degrees Celsius.

Simplifying the ratio $\frac{A}{B}$ based on equation (44) a linear expression is obtained by a Taylor series expansion in which quadratic and higher terms in T are neglected:²³

$$\frac{A}{B} \approx \frac{1,37 \cdot (T - 20)}{109 + T} \approx 0,01 \cdot (T - 20) \quad (45)$$

Also the viscosity of water at 25 degrees Celsius, η_{25} is known²² so that using the formula (43) η_{20} can be obtained.

So using equations (43) and (45) the relation (42) can be expressed approximately by:²³

$$\kappa \approx constant \cdot (1 + \ln(10) \cdot 0,01 \cdot (T - 20)) = a \cdot T + b \quad (46)$$

Where a, b are constants.

In a similar way as before, a linear equation involving a temperature coefficient can be derived:^{19,24,25,26}

$$\kappa = \left(1 + \alpha(T - T_{ref})\right) \cdot \kappa_{ref} \quad (47)$$

T_{ref} is the reference temperature and κ_{ref} is the conductivity of the electrolyte solution at T_{ref} . Typically, in conductivity measurement the reference temperature is at 25 degrees Celsius. The parameter α is the temperature coefficient which is expressed as a conductivity variation measured in $\frac{\%}{^\circ\text{C}}$ or $\frac{\%}{^\circ\text{F}}$. That is to say, α represents the percentage change in liquid's conductivity, if the temperature increases by one degree Celsius or Fahrenheit.²⁶ The previous formula describes the linear temperature compensation for conductivity. However, it is assumed that α is independent on the temperature and its value is fixed.²⁶ However, this is not true so that equation (47) describes the temperature dependence of conductivity in an approximate manner. In this way equation (47) is accurate only within in a limited temperature range around the T_{ref} .²⁴ In addition, the temperature coefficient depends on the composition and on the concentration of the dissolved in the water electrolytes. The average temperature coefficient of ionic salts (like sodium chloride) ranges from 2,2-3%/°C.²⁷ Also, the magnitude of α at 25 degrees Celsius is approximately 2%/°C for the majority of aqueous electrolytes.^{27,28}

Another model that describes the relationship between electrical conductivity of aqueous solutions and temperature is the Arrhenius equation:^{19,20}

$$\kappa = \kappa_0 \cdot e^{-\left(\frac{E_A}{R \cdot T}\right)} \quad (48)$$

E_A is the activation energy (in KJ/mol), the pre exponential factor κ_0 is a constant that fits the experimental measurements. It is assumed that both E_A and κ_0 are temperature independent. The value of constant R is $8,314 (J/K \cdot mol)$ and T is the temperature in degrees Kelvin. The previous relationship is known as conventional Arrhenius expression. A different compensated expression takes into account the temperature dependence of the dielectric constant, $\epsilon_s(T)$ contained in the pre exponential factor, κ_0 .²¹

The temperature dependence can be described by another empirical function, the Vogel-Tammann-Fulcher (VTF) equation^{19,21}

$$\kappa = \kappa_0 \cdot e^{-\left(\frac{B}{T-T_0}\right)} \quad (49)$$

κ_0, B and T_0 are empirical fitting parameters without any physical interpretation. However, the pre exponential factor can be modified and be temperature dependent so that equation (49) can be written as:¹⁹

$$\kappa = \frac{A}{T} \cdot e^{-\left(\frac{B}{T-T_0}\right)} \text{ or } \kappa = \frac{A}{T^2} \cdot e^{-\left(\frac{B}{T-T_0}\right)} \quad (50)$$

Where A is a fitting parameter.

The temperature dependent conductivity of liquid electrolyte can be represented by equations (48) and (49) or (50). However, Arrhenius equation is more suitable and accurate in describing the temperature-dependent conductivity for liquid electrolytes, whereas VTF equation can be used to describe the conductivity variation with temperature for ionic liquids and polymer electrolytes.¹⁹

As previously stated the temperature coefficient, a is not constant for all measurement temperatures. Thus the relationship between conductivity and temperature cannot be linear. So a polynomial (parabolic) fit may be applied to the experimental conductivity measurements of an aqueous solution over a temperature range. For example, the temperature dependent conductivity can be represented as:^{26,24,28}

$$\kappa = \alpha \cdot T^2 + b \cdot T + c \quad (51)$$

a, b, c are constants determined by fitting to the experimental results.

1.6 Magnetic field within electrically conductive material

It should be noted that for many MRI guided applications such as MR temperature imaging (MRTI), the temperature dependent conductivity is an important parameter. During RF-excitation, the time-varying RF field, $B_1(t)$ undergoes amplitude attenuation and phase retardation within the conductive volume to be imaged. For a

fixed depth within the conducting material , amplitude attenuation and phase retardation or phase.lag vary with conductivity in a linear fashion. However as it was mentioned earlier, the correlation between conductivity and temperature is positive. Thus, amplitude attenuation and phase retardation will increase with increasing temperature. In addition, the resultant flip angle which determines the fraction of the M turned into transverse magnetization, M_{xy} (MRI signal) depends on the amplitude of B_1 .So it is obvious that the variation of signal intensity and the distribution of flip angles will not be homogenous over the volume to be imaged.^{29,30,31}

1.7 Scope of this study – questions addressed

The first aim of this study, was to compare the ability of two major T2 mapping sequences, Multi – Echo Spin Echo (MESE) and Half Fourier Single Shot Turbo Spin Echo (HASTE) to measure relaxation time T2 in aqueous solutions with varying salt concentration. Moreover, MESE and HASTE were utilized to quantify another MR parameter which is proton density (PD). Then we wanted derive a relationship between T2/PD and temperature by utilizing both of the MESE and HASTE imaging techniques. Then we compared the results obtained from the two sequences and we tried to establish which one of them is suitable and accurate method for monitoring the temperature of typical electrolyte solutions. Finally, using both of the MESE and HASTE sequences, we wanted to investigate the correlation between T2 relaxation time and electrical conductivity (EC) at a given temperature.

2. MATERIALS AND METHODS

2.1 Electrical conductivity measurement.

Electrical conductivities of the salt solutions were measured by using a conductivity meter (HI-2030 edge® Hybrid Multiparameter EC Meter, figure 14)³². The digital conductivity electrode is the HI-763100 potentiometric probe (figure 13)³³ with a built in thermometer sensor. In this way there is no need for an external temperature probe and the measurement process becomes easier. Moreover, the electrode probe is ring type and using tetrapolar configuration. The use of a 4 electrode system in potentiometric method for measuring electrical conductivity provides important experimental advantages. The 4 ring electrode system provides more stable measurement than the amperometric two pole probes and the effects of electrode polarization are suppressed.^{27,34} So it is possible to measure a much wider conductivity range than a two electrode sensor especially for solutions in liquid state.

Before the conductivity measurements the probe was calibrated with the HI-7030 conductivity standard solution with the value of $12880 \frac{\mu S}{cm}$ at 25 degrees Celsius. Important specifications of the equipment are provided in the following tables.³⁵

HI-763100 Edge Digital EC Platinum 4 Ring Electrode

Body material	PEI
Type	4 ring
Insulator	Glass
Electrodes	Platinum
Range	0 to 200 <i>mS/cm</i>
Temperature sensor	Yes

HI-2030 edge® Hybrid Multiparameter EC Meter

EC range	Up to 500 <i>mS/cm</i> (Absolute conductivity)*
Resolution	0,01 $\mu S/cm$, 0,1 $\mu S/cm$, 1 $\mu S/cm$, 0,1 <i>mS/cm</i>
Accuracy (@ 25°)	$\pm 1\%$ of reading ($\pm 0,05 \mu S/cm$) or 1 digit)
Temperature Compensation (TC)/T.Coef (%/°C)	Yes ,No TC (Absolute conductivity)/0.0 to 6 %/°C
Temperature reference in Celsius degrees	20° or 25°
Cell factor	0,01 to 9,999 cm^{-1} **

* Absolute electrical conductivities of the salt solutions were measured. Thus no TC was selected.

** The cell factor of the sensor during conductivity measurements was $1cm^{-1}$.



Figure 14 : HI-763100 Edge Digital EC Platinum 4 Ring Electrode.³³



Figure 14 : HI-2030 edge® Hybrid Multiparameter EC Meter.³²

2.2 MRI system : Siemens Magnetom Sonata 1.5 T.³⁶

MODEL	Magnetom Sonata
Magnet	Superconducting
Power needed	
Line voltage, VAC	380/400/420/440/480
KVa (Power needed)	80
A/c, btu/hr (POWER NEEDED)	10.6 kW peak
CLINICAL USE (POWER NEEDED)	Whole body
Cooling method (X-RAY TUBE)	Single cryogen, 2stage refrigeration
CRYOGEN USE, L/hr	
Liquid helium (CRYOGEN USE, L/hr)	0,075
MAGNET WEIGHT, kg (CRYOGEN USE, L/hr)	4,050; 5,500 in operation
DIMENSIONS (HXWXD),CM (CRYOGEN USE, L/hr)	235 x 215 x 160
Radial/axial, m (5-GAUSS FRINGE FIELD)	2.5/4
SPECTROSCOPY (GRADIENT SUBSYSTEM)	SVS or CSloptional

IMAGING	
Pulse sequences (IMAGING)	GRE, IR, FIR, STIR, TrueIR/FISP, FSE, FLAIR, MT, SS-FSE, MT-SE, MTC, MSE, EPI, 3-D: DESS/CISS/ PSIF, GMR, fat/water sat/exc, others
Repetition time, msec (IMAGING)	1.5 @ 256 x 256
Echo time, msec (IMAGING)	0.58 @ 256 x 256
Inversion time, msec (IMAGING)	22
Slice thickness, mm (GANTRY)	0.1-200 (2-D), 0.05-20 (3-D)
Fov, cm (IMAGING)	0,5-40
Fov offsets (IMAGING)	±20
Scan orientations (IMAGING)	Orthogonal (x, y, z); oblique second compound
Measuring matrix (IMAGING)	64 x 64 to 1024 x 1024
Display matrix (IMAGE DISPLAY)	1024 x 1024 full screen
Resolution, mm (PERFORMANCE)	0.01 in plane
GRADIENT SUBSYSTEM	
Strength, mt/m (GRADIENT SUBSYSTEM)	45
Rise time (GRADIENT SUBSYSTEM)	200 µsec
Slew rate	200 T/m/sec
Memory size, mb (GRADIENT SUBSYSTEM)	72 GB HD, 2 GB RAM
ARRAY PROCESSOR (EXTERNAL BEAM)	Dual Pentium IV
Memory size, mb (GRADIENT SUBSYSTEM)	5x18 GB, 1GB RAMa

Storage media/size (GRADIENT SUBSYSTEM)	CD-ROM
Image storage capacity (GRADIENT SUBSYSTEM)	Approx5,000
Respiratory gating (DISPLAY)	Yes
IMAGING MODES	
Single (EYEPIECE)	Yes
Multislice (IMAGING MODES)	Yes
Volume study (IMAGING MODES)	Yes
Additional (Alarms, high/low)	Multiangle, multioblique

SHIMMING (CRYOGEN USE, L/hr)	Passive, active; 1st order; opt 2nd order
Body coil (DIAMETER, cm)	60
Head coil (DIAMETER, cm)	26 ID, open sides
CARDIAC GATING	
Ecg/peripheral (CARDIAC GATING)	Yes/yes
OPTIONS	Whole-body integrated panoramic array, applications packages: advanced cardiac, diff/perf, pMRI
BORE FEATURES (DIAMETER, cm)	Lights,ventilation,nurse call,intercom
Reconstruction time	
Single slice, sec (RECONSTRUCTION TIME)	0.056@ full 256 x 256
Multislice, sec (RECONSTRUCTION TIME)	0.056/slice @ full 256 x 256
Volume, sec (RECONSTRUCTION TIME)	0.056/slice @ full 256 x 256
DICOM 3.0 COMPATIBLE (POWER NEEDED, VAC)	Yes
Angiography	Yes
ECHO PLANAR IMAGING (CARDIAC GATING)	Optionalpackage
ELECTROMAGNETIC FIELD STRENGTH, T (5-GAUSS FRINGE FIELD)	1,5
CONFIGURATION	Compact, open sides
OTHER ATTRIBUTES (Interference compensation)	3-D shim; IPP/ panoramic table; 3-D MIP/MPR/SSD; remote diagnostics; Syngo/MRease; dynamic analysis; integrated postprocessing
FDA CLEARANCE (Interference compensation)	Yes
CE MARK (MDD) (Interference compensation)	Yes
MARKETING REGION (Interference compensation)	Worldwide

2.3 Temperature measurement.³⁷

A fiber optic thermometry system (m3300 Biomedical Lab Kit Fluoroptic thermometer) was used in order to perform real - time temperature measurements of the solutions during heating. The system consists of an m3300 Biomedical Lab Kit instrument, fluoroptic probe and fiber optic extension cable. The different components of the fluoroptic system are individually presented and described below.

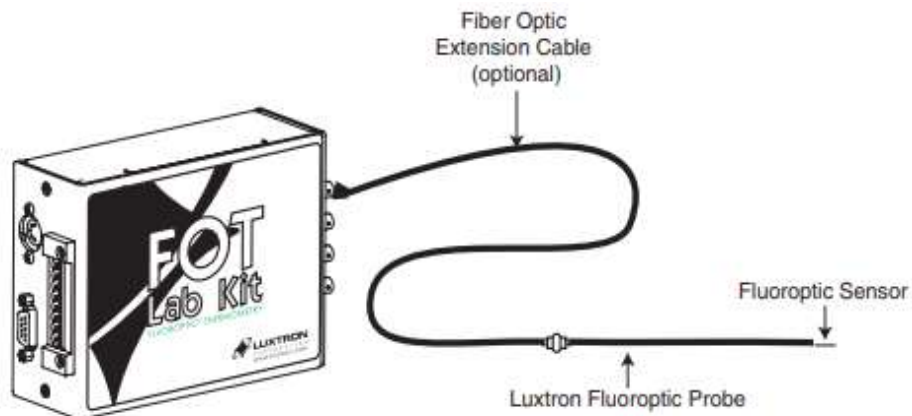


Figure 15 : Fluoroptic Thermometry system. It consists of an m3300 Biomedical Lab Kit ,fiber optic extension cables and fluoroptic temperature probe.³⁷

m3300 Biomedical Lab Kit instrument

It is a four – channel (fiber Optic Probe Connections) Fluoroptic thermometry instrument encased in an all steel enclosed (figure 16)³⁸. The instrument provides accuracy better than 0,2°C over a temperature range 0 to 120°C. It includes 0 to 10 Volt analog outputs for each measurement channel and it uses an RS-232 serial interface to PC for command input and data output. The user interface was accessed through TrueTemp software which is compatible with Windows. Particularly, TrueTemp is a data capture, display and analysis software for Luxtron instruments that allows the user to monitor up to 4 temperature probes. Important specifications of this component are given in the following table.

m3300 Biomedical Lab Kit instrument specifications

Channels	4
Measurement Range	0 to 120°C
Electrical Interference	Immune to MR, EMI, RF and microwave
Accuracy (Calibrated)	±0,2°C within ± 20° C of Calibration Point ±0,5°C within ± 50° C of Calibration Point
Standard Default Calibration	1% of full scale
Repeatability (Precision)	±0.5°C RMS at 8 Samples per Measurement
Analog output Resolution	0.01°C

Measurement Rate	1 to 4Hz per active Channel
Output Format	Selectable °C, °F and °K
Self Diagnostic	Self Diagnosis and Probe Errors Available on RS-232
Input Power	Universal power supply (input 85-264 VAC ,49-63 Hz_
Serial Output	RS-232 serial interface at 9600 bps
Analog Output	0 - 10VDC
Dimensions	184mm × 144mm × 51mm
Storage Temperature	-55°C to +75°C
Operating Environment	10°C to 40°C



Figure 16 : m3300 Biomedical Lab Kit instrument.³⁸

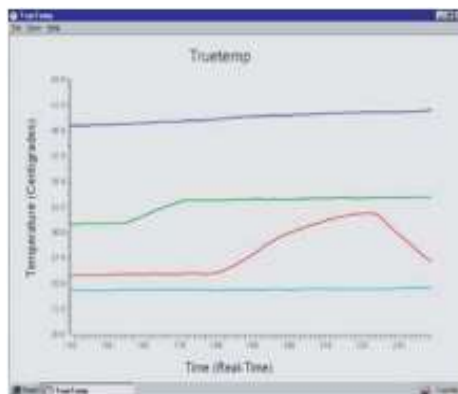


Figure 17: Luxtron TrueTemp data acquisition and graphing software.³⁷

Fluoroptic temperature probes^{37,39}

The Fluoroptic temperature probe (STB) is entirely non – metallic in construction and its sensor material in the tip is temperature sensitive and phosphorescent. So these probes are immune to EMI and RF interference and they are electrically non – conductive. Also, heat loss by induction is minimal due to the low thermal conductivity and probe’s small geometrical cross section. The probe tip has a diameter (tip OD) of 0,5 mm and the outer diameter (OD) of the probe is also 0,5 mm. Thus the probes can be characterized as minimally invasive. In addition they are protected with a Tefzel ethylene - tetrafluoroethylene (EFTE) fluoropolymer jacket so that they can be used in RF environments. Important specifications of this component are given in the following table.

Specifications for Standard STB Probe Used with the LUXTRON m3300 biomedical Lab Kit

Tip diameter	0,5mm
Jacket diameter	0,5mm
Jacket material	Tefzel (USP Class VI)
Temperature range	0 to 120°C
Response time	0,25 seconds

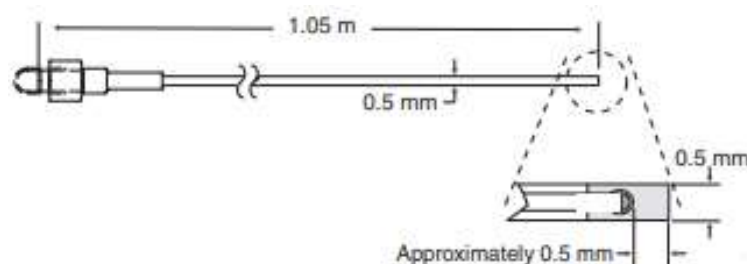


Figure 18 : Standard STB Fiber optic Probe .Its length is approximately 1 meter and its diameter (Jacket diameter) is 0,5 mm.³⁸

The temperature measurement is based on the fluorescence of the phosphor compounds attached at the end of the probe. Specifically, the instrument sends an excitation light pulse through the fiber optic cable and cause the phosphor layer to be excited and fluoresce. After excitation, the exponentially decaying signal returns to the instrument through the same fiber optic cable. DPS based electronics of the instrument detect and measure the decay time (is symbolized with τ) of the fluorescence signal. The fluorescent decay time varies with the temperature of the sensor. The electronics of the instrument through multipoint digital integration of the curve measure the decay time. Thus the analogue decaying analogue signal is converted to digital value which is correlated directly with a specific value of

temperature. Finally this value is converted to this calibrated temperature. A plot of the fluorescence intensity over time is given below.

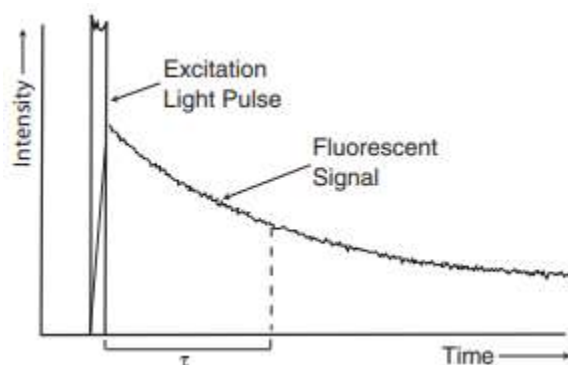


Figure 19 : Fluorescence decaying signal.³⁷

The dependence of the curve shape on temperature is depicted in the following plot.

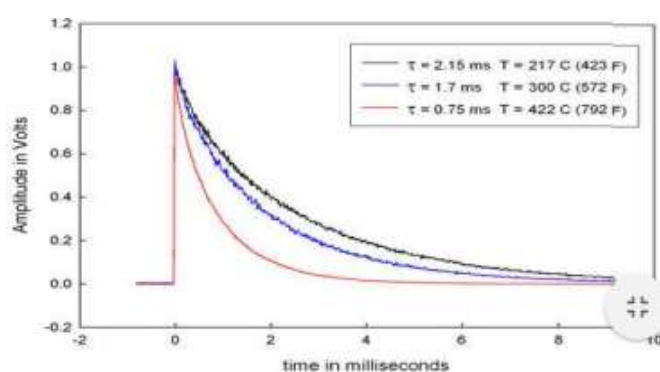


Figure 20 : The decay time, τ or the shape of the curve varies with the temperature of the sensor. As temperature increases the value of τ or the decreases.³⁹

2.4 Laboratory water bath.⁴⁰

A water bath (WPE 45 – Memmert GmbH) was used to incubate sodium chloride sample tubes with different concentrations in circulating water at a constant temperature. WPE 45 is circulating waterbath and is using high quality, corrosion – resistant stainless steel for the external and interior casing. It provides excellent temperature uniformity of heated water at various locations within the reservoir of the waterbath via a circulating pump (Figure 21). For example, when the water temperature is 90°C the maximum temperature difference between two points in the waterbath is 0,36°C. Efficient temperature maintenance can be performed over a wide range of temperatures due to continuous water circulation inside the waterbath. In addition, heating elements integrated around the tank improves temperature uniformity within the watertank (Figure 22). Moreover, gable cover was

always closed during experiments to prevent liquid loss due to evaporation and maintain temperature uniformity within the watertank. Important technical data of this laboratory equipment is given below.

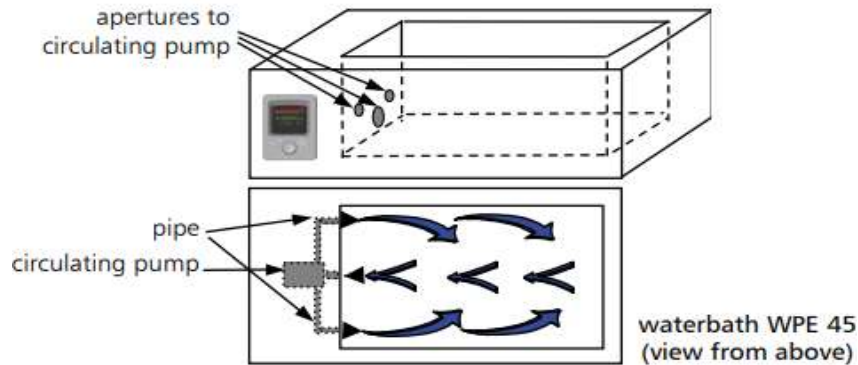


Figure 21 : A circulation pump improves thermal uniformity of the water inside the waterbath. The pump draws water from the center of the working chamber and distributes it through the pipes in the front and in the back of the bath.⁴⁰

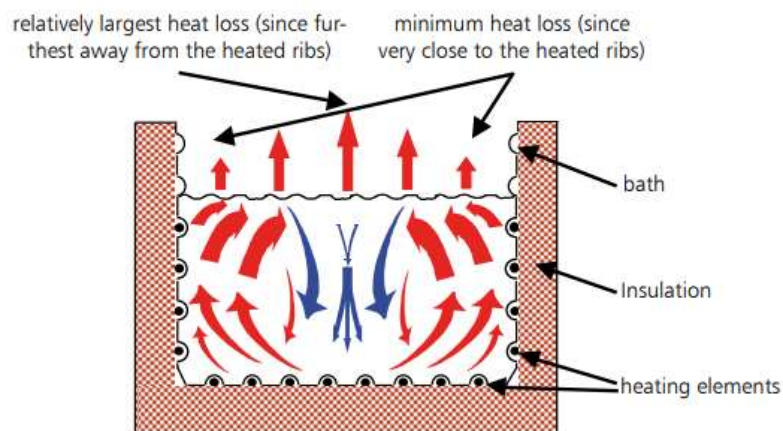


Figure 22 : Waterbath insulation and appropriate positioning of heating elements on three sides around the tank reduce heat dissipation especially in regions away from the heated ribs. Thus temperature uniformity of the water within the watertank is improved.⁴⁰



Figure 22 : Memmert – waterbath WPE45.⁴⁰

Technical specification from Memmert – waterbath WPE45

Volume (Liter)	45
Usable bath length A (mm) (figure 23)	590
Usable bath length B (mm) (figure 23)	350
Usable bath length C (mm) (figure 23)	220
Housing length D (mm) (figure 23)	818
Housing width E (mm) (figure 23)	516
Housing height (with flat cover) F (mm) (figure 23)	296
Housing height (with gable cover) G (mm) (figure 23)	401
Current consume (A)	12,2
Power (W)	2800
Ambient conditions	Ambient temperature 5°C - 40°C rh max. 80 % (no condensation) Overvoltage Category : II Contamination degree: 2
Voltage	230 V, 50/60 Hz
Electric load	Approx. 2800 W
Setting temperature range	10°C to 95°C and boiling stage
Setting accuracy	0,1°C
Indication accuracy	0,1°C
Working temperature range	Min.15°C above ambient up to 95°C (only with pump switched off)
Resolution of display	0,1°C up to 99,9°C / 1°C from 100°C

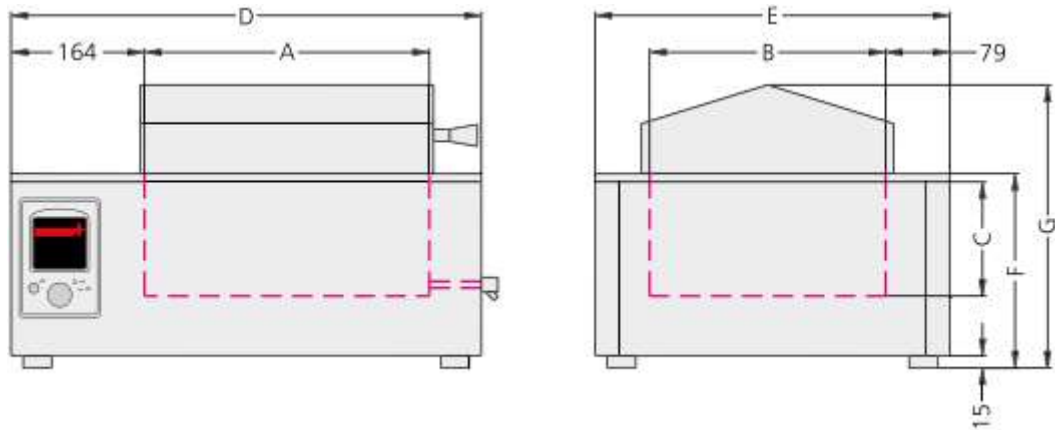


Figure 23 : Dimensions (in mm) of the Memmert – waterbath WPE 45.⁴⁰

2.5 Centrifugal water pump^{41,42}

A submersible centrifugal waterpump (COMET 12V submersible water pump VIP 16 LPM) was used in the closed circulation loop system that was constructed for the experiment. Technical specifications are given below.

Power supply Required (V), DC	12
Power consumption (W)	10 – 20
Maximum Amp consumption (A)	1,8
Discharge water rate : max (LPM)	16
Delivery head : max (m)	6,5
Delivery pressure : max (bar/psi)	0,65/9,4
Outlet diameter (mm)	10



Figure 22 : COMET 12V pump VIP 16 LPM.⁴⁰

2.6 Experimental design

2.6.1 Sodium chloride (NaCl) solutions

Aqueous sodium chloride solutions of different concentration were prepared. In a given amount of solute (in grams), the final volume of the solution was always 100 ml. In the following table, the mass / volume (w/v) percent is used to express the concentration of a sodium chloride solution.

Table 1

# of solution	Volume of solution (ml)	Mass of solute (gr)	% w/v
1	100	0,2	0,2
2	100	0,4	0,4
3	100	0,6	0,6
4	100	0,8	0,8
5	100	0,9	0,9
6	100	1	1

For each solution of differing sodium chloride concentration, electrical conductivity (EC) was measured over a wide temperature range of 20 – 45 °C. All electrical conductivities measurements were performed using the HI-2030 edge® Hybrid Multiparameter EC Meter. In all solutions the variation of EC with temperature is shown in the Results Section.

Next, seven plastic vials of approximately 100 ml volumes were used : a) 6 vials containing sodium chloride solutions with the salt concentration varying from 0,2% to 1% w/v%, b) 1 vial containing tap water with. All seven plastic vials were enclosed in a sealed water filled plastic heating box as shown in the following figure.



Figure 23 : NaCl concentration (w/v) : (1) 0,2 %, (2) 0,4 %, (3) 0,6%, (4) 0,8%, (5) 0,9%, (6) 1%. (7) tap water.

In figure 23 the eighth plastic vial which was filled with sterillium gel was not used throughout the experiment.

The heating box was equipped with a glass tube heat exchanger (See figure 26). Also, four fiber thermometric probes (Fluoroptic™ thermometer m3300 Biomedical Lab Kit) were placed into the heating box to monitor the temperature levels. One of them was placed at the front side of the heating box, whereas another one was placed at the back side of the box close to the heat exchanger. This spatial configuration of the temperature sensors allowed us to check when the temperature inside the heating box was homogenous. The other two temperature probes were used to monitor the temperature of the 0,2 %, and 1% sodium chloride solution (See figure 24). The heating box was inserted into the RF head coil and then it was placed inside the gantry of the MRI scan as shown in the following figure.

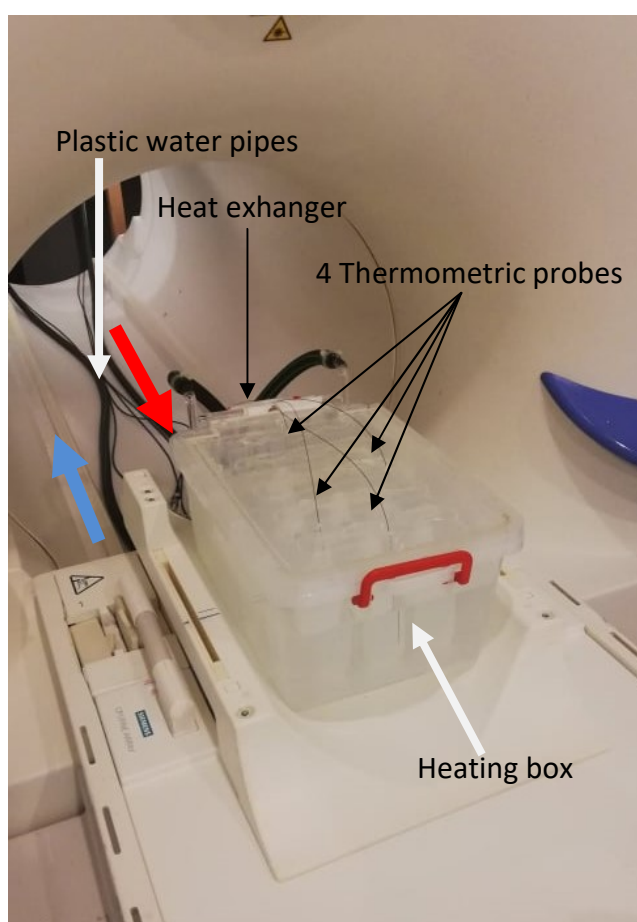


Figure 24: Monitoring spatial distribution of temperature inside the heating box using four thermometric probes. Water flows in /out of the heat exchanger through two water pipes (red arrow and blue arrow respectively).

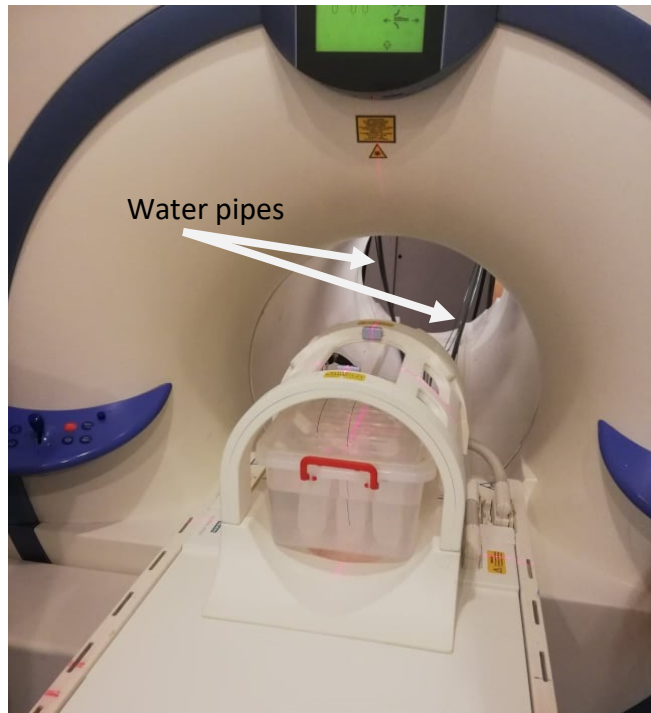


Figure 25: The heating box is properly placed inside the gantry of MRI scan.

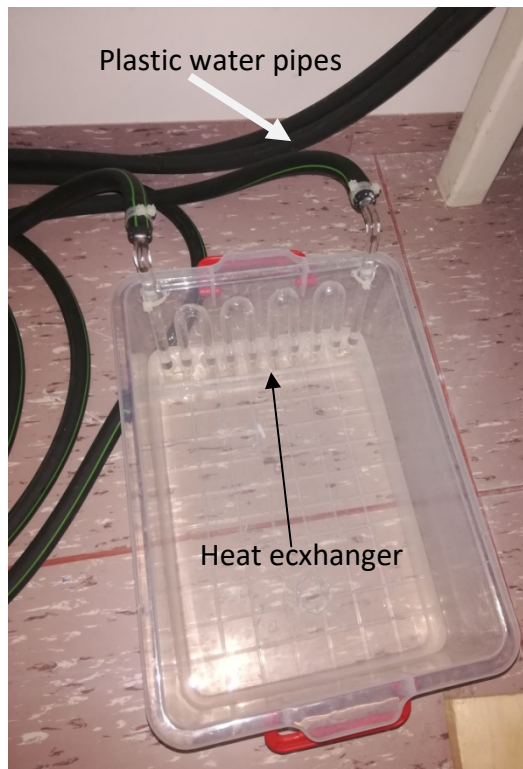


Figure 26: A heat exchanger is attached to the back side of the heating box.

2.6.2 Closed loop circulation system

As it was previously stated, the 7 plastic vials (See figure 23) were enclosed in a sealed plastic heating box which inside the gantry of the MRI scanner. The heating box was equipped with a glass tube heat exchanger which was positioned at the one side of the heating box. Then the heat exchanger was connected to a temperature – regulated water bath (Waterbath WPE, Memmert) via a couple of high pressure water pipes (see Figures 24, 25,26), thus ensuring water circulation on a close water circuit configuration (See figure 26). Thus heat is transferred to the water filled heating box through the glass type heat exchanger by conduction. In this way the temperature inside the box can be controllably increased. Moreover, the COMET 12V submersible pump was used to circulate the water around the closed loop. The whole closed loop circulation system is simply represented below. Under this mechanical setup, the monitoring and the control of the desired temperature of all plastic vials inside the heating box was achieved during the MRI scan. The arrows in the following figure indicate the direction of water flow.

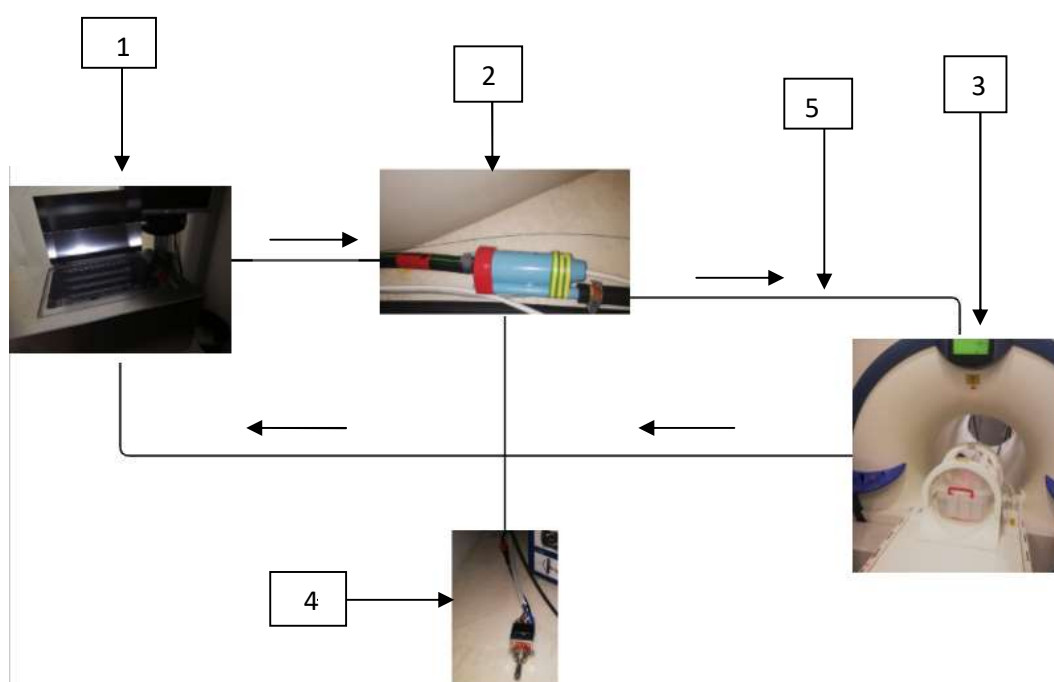


Figure 27: Closed loop circulation model .The labeled components are (1) Memmert water bath, (2) COMET 12V submersible water pump, (3) The plastic heating box which holds six 100 ml plastic vials containing sodium chloride solutions at different salt concentrations and one 100 ml plastic vial containing tap water, is placed properly within the gantry of the magnet, (4) On off switch for water pump, (5) high pressure water pipes.

In the previous figure, (1),(2) and (4) components are placed inside the equipment room which is located immediately adjacent to the Magnet room.

2.6.3 MR Image acquisition

For the experimental setup, involving all the samples in the heating box (NaCl solutions and tap water), MR imaging was performed on a hybrid clinical 1,5 Tesla wholebody superconducting MR imaging system (MAGNETOM Sonata/Vision, Siemens Healthcare, Erlangen, Germany, Gradient Strength : $40 \text{ mT} \cdot \text{m}^{-1}$, Gradient rise time : $200 \mu\text{s}$, Gradient slew rate : $200 \text{ mT} \cdot \text{m}^{-1} \cdot \text{ms}^{-1}$). A standard quadrature RF body coil was used for signal excitation and a 4 element, 2 channel head array coil was used for signal detection. Starting at a temperature of approximately 20°C , the heating box which contains all the plastic vials was heated up and after sufficient time quantitative T2 relaxometry was performed. After each scan, the temperature was increased and the described procedure was repeated until the samples in the heating box reached the maximum temperature of 45°C . A typical scheme of temperatures was 20°C , 25°C , 30°C , 35°C , 37°C , 40°C , 42°C and 45°C .

After localization was completed two different sequences were utilized in order to obtain the T2/PD maps accordingly. These were :

1: A 2D Half – Fourier Acquisition Single – Shot Turbo spin Echo (HASTE) sequence with the following parameters. Field Of View (FOV) = $(21,9 \times 35) \text{ mm}^2$ on the coronal plane, matrix size = 256×160 , TR = inf., effective TE's = 41 ms , 428 ms , 815 ms , 1250 ms , Number of averages (NEX) = 1 and 32, image pixel bandwidth = 675 Hz/pixel slice thickness = 5 mm , number of slices = 1 slice position. In addition a driven equilibrium pulse (-90° -pulse) was used in conjunction with HASTE sequence so that T2 relaxation time, and not T1, modulates the image signal intensity (Heavily T2-weighted). The total scan time was 2 seconds (HASTE with 1 NEX) and 10 seconds (HASTE with 32 NEX)

2: A Multi – Echo Spin Echo (MESE) sequence with the following parameters. Field Of View (FOV) = $(21,9 \times 35) \text{ mm}^2$ on the coronal plane, matrix size = 256×160 , TR= 2000 ms , TE = 50 ms . This MESE sequence was based on a 2D Carr-Purcell-Meiboom- Gill (CPMG) multi-echo train sequence with alternating 180° RF pulses under the Phase-Alternating-Phase-Shift (PHAPS) scheme. The MESE sequence was applied using 32 symmetrically repeated spin echoes. The first TE was 50 ms and the rest 31 TE's were obtained thereafter every 50 ms . TE's : $(50, 100, 150, 200, \dots, 1600 \text{ ms})$, Number of averages (NEX) = 1, image pixel bandwidth = 780 Hz/pixel , slice thickness = 5 mm , number of slices = 1 slice position. The total scan time was 4 minutes and 20 seconds.

Images obtained from these three sequences at different TE's and temperatures are shown bellow. Sodium chloride solutions at different salt concentrations and tap water are imaged in the coronal plane. According to the previous table, each solution is labeled with a number (1 up to 6) which indicates its salt concentration expressed as weight volume percentage. Tap water is labeled with the number 7.

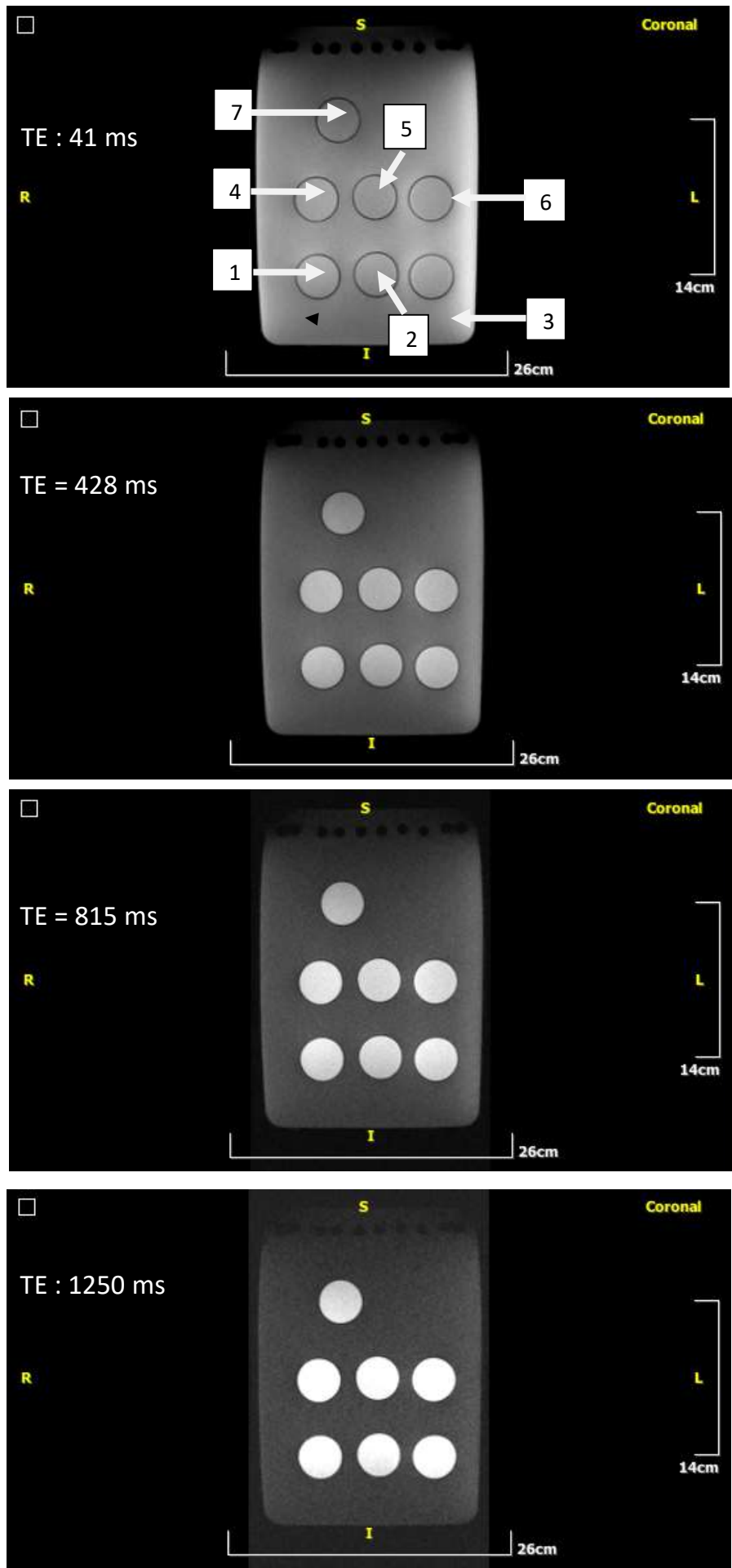


Figure 29 : Images at TE : = 41, 428, 815 and 1250 ms obtained from the HASTE sequence at temperature, $T = 20\text{ }^{\circ}\text{C}$.

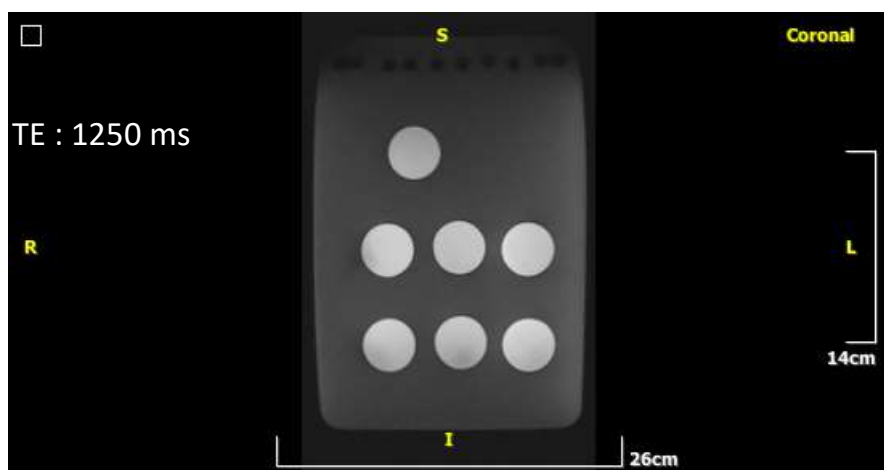
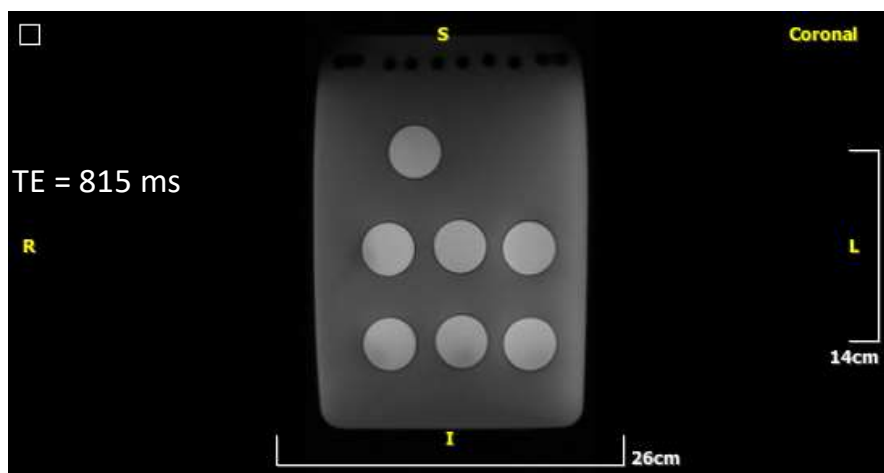
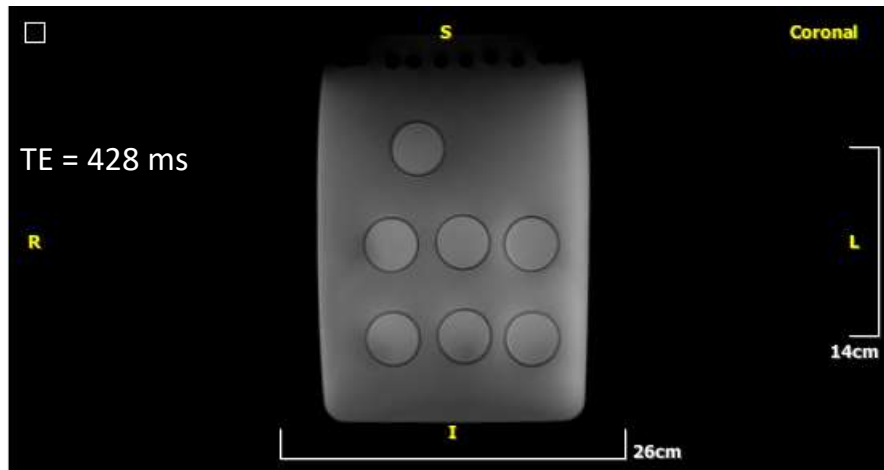
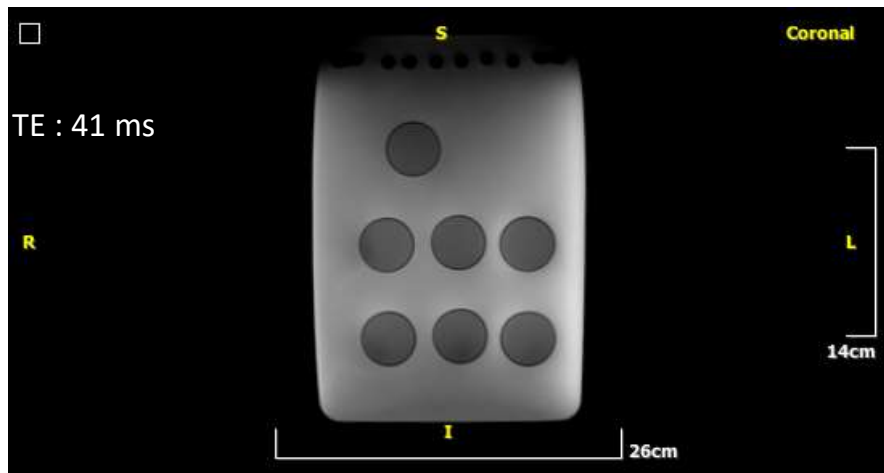


Figure 30 : Images at TE : = 41, 428, 815 and 1250 ms obtained from the HASTE(NEX 32) sequence (NEX =32), at temperature, T = 20 °C.

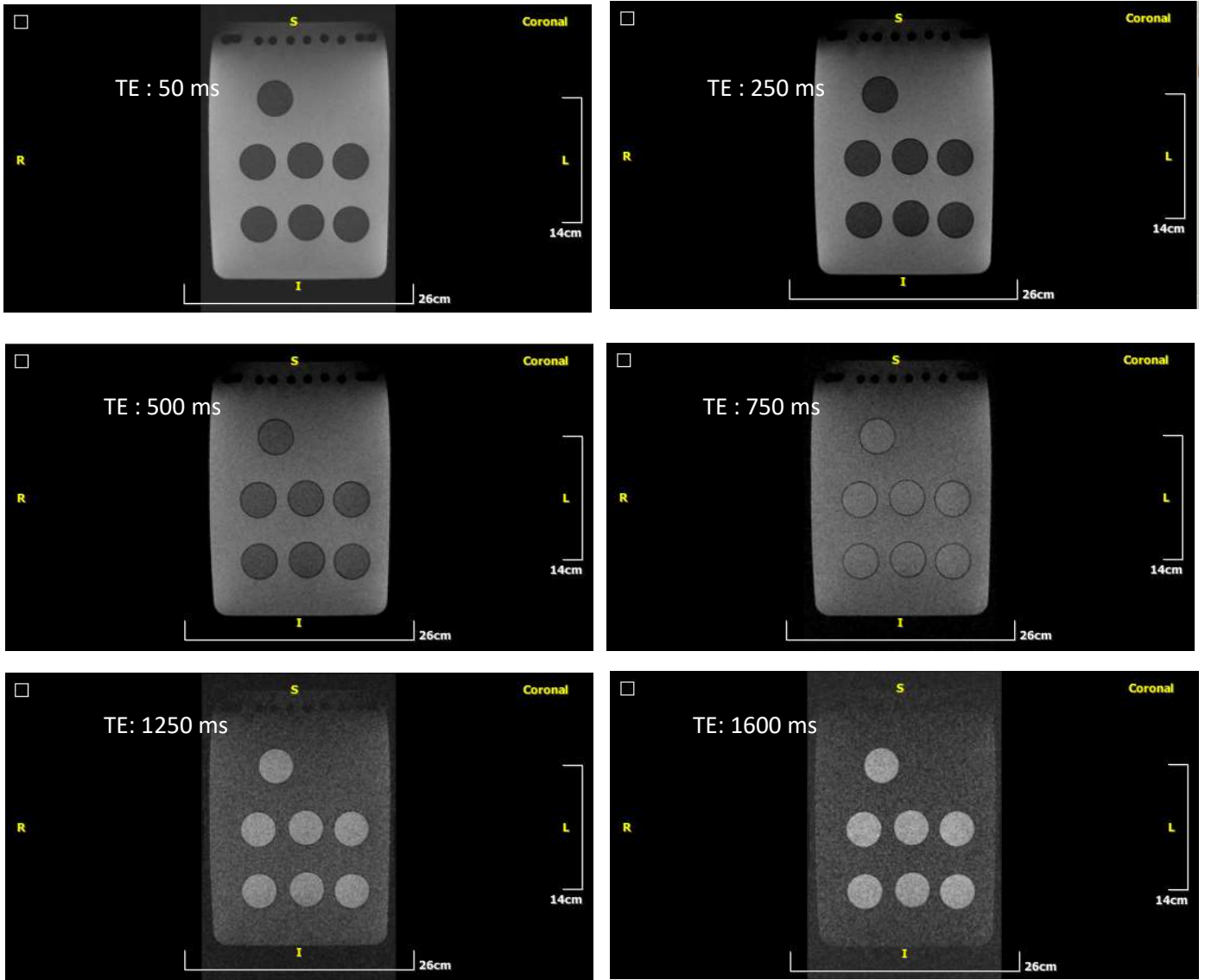


Figure 31 : Images at TE : 50, 250, 500, 750, 1250, 1600 ms obtained from the MESE sequence at temperature, $T = 20\text{ }^{\circ}\text{C}$.

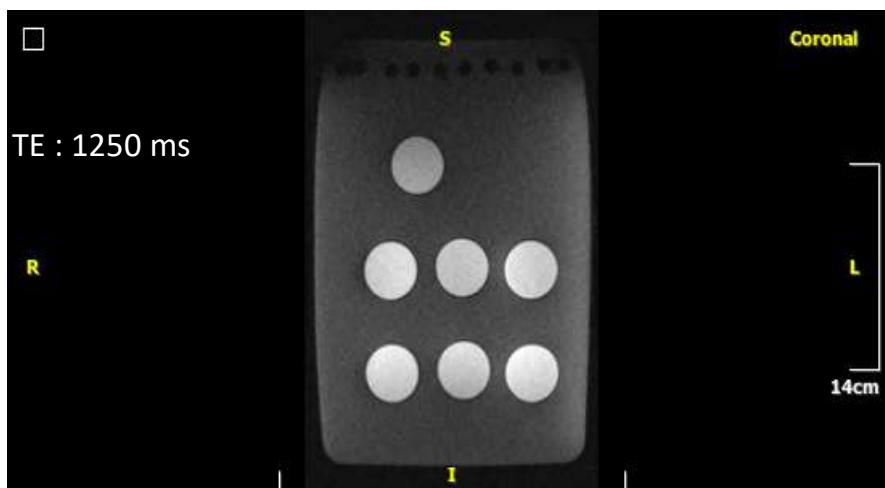
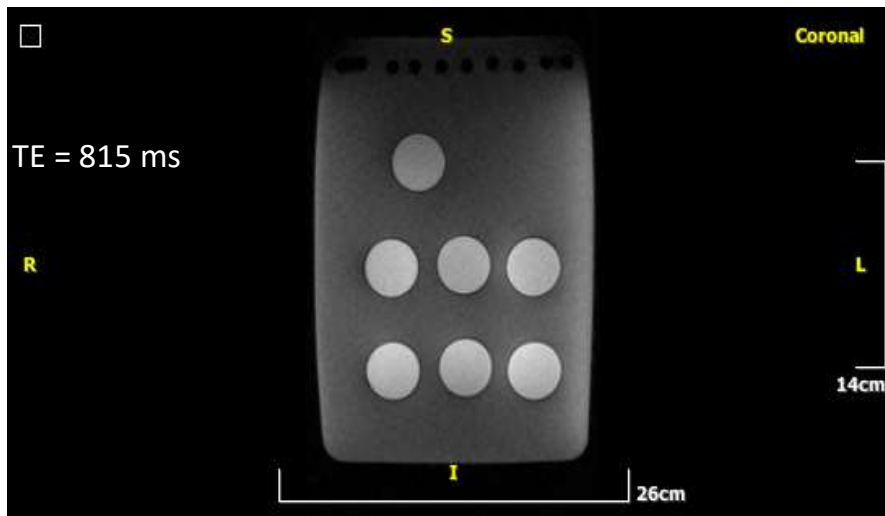
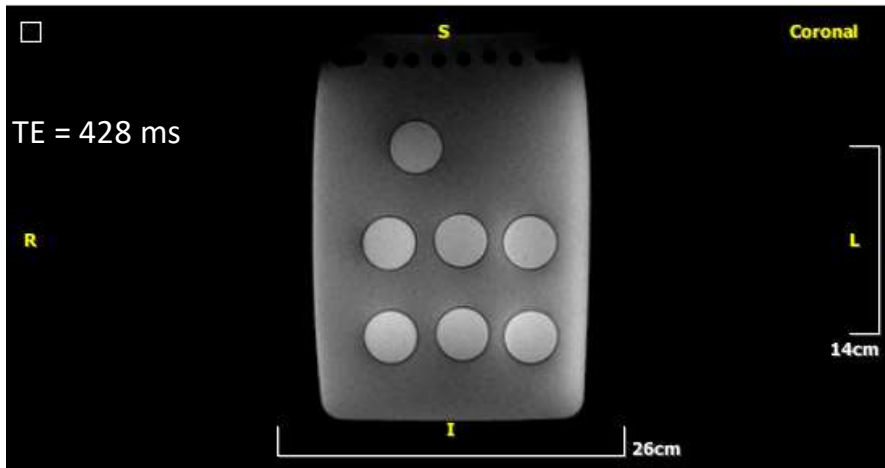
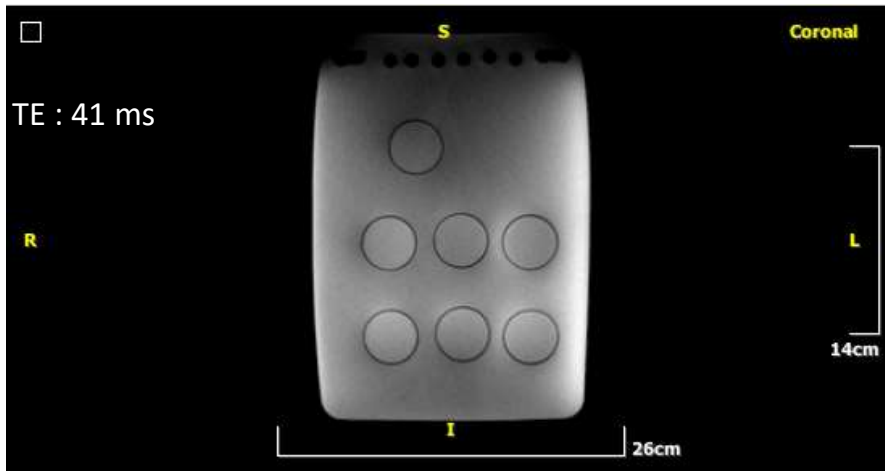


Figure 32 : Images at TE : = 41, 428, 815 and 1250 ms obtained from the HASTE sequence, at temperature, $T = 37\text{ }^{\circ}\text{C}$.

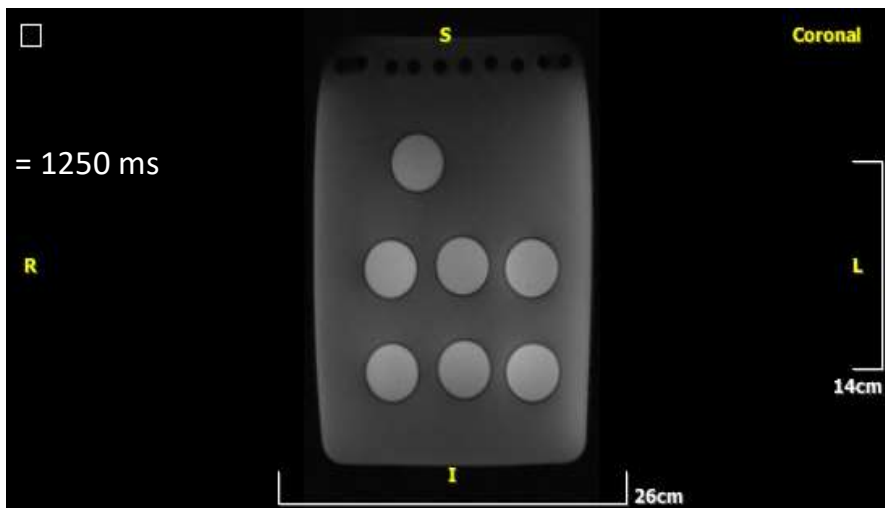
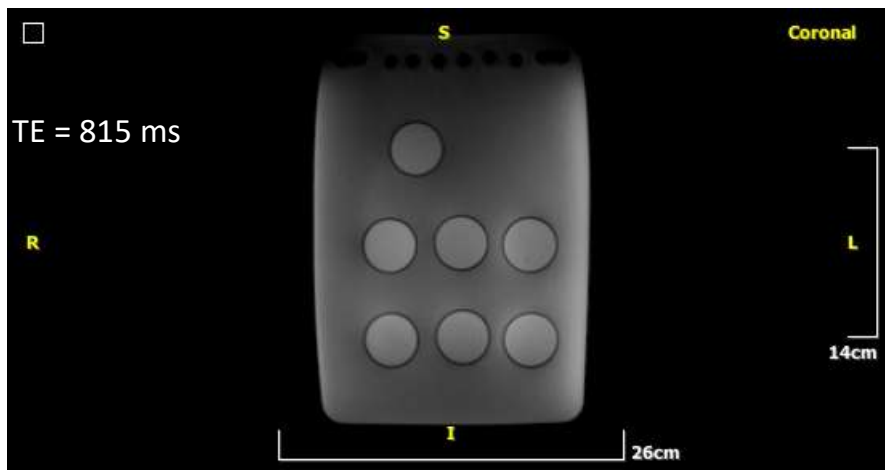
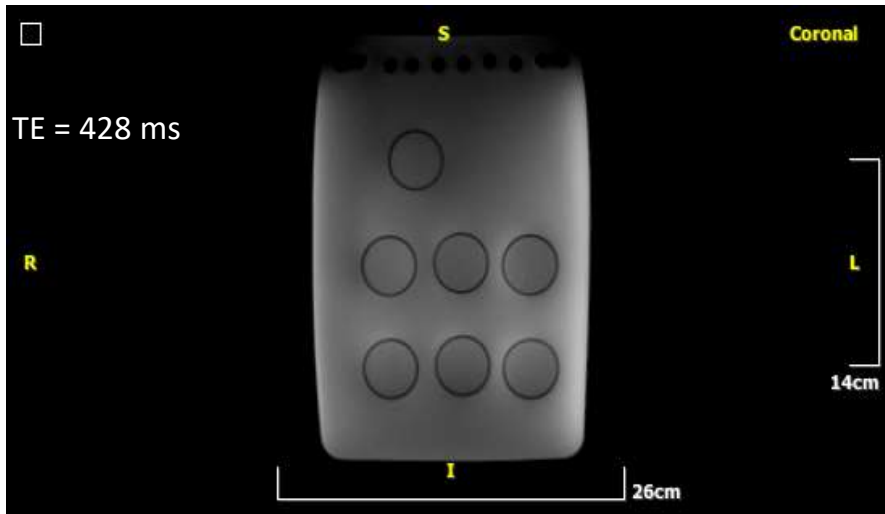
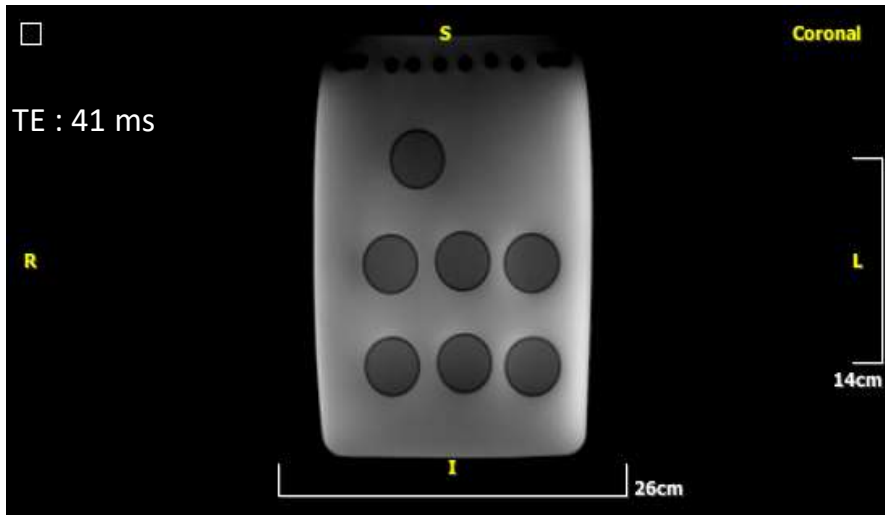


Figure 33 : Images at TE : = 41, 428, 815 and 1250 ms obtained from the HASTE sequence (32 NEX), at temperature, $T = 37\text{ }^{\circ}\text{C}$.

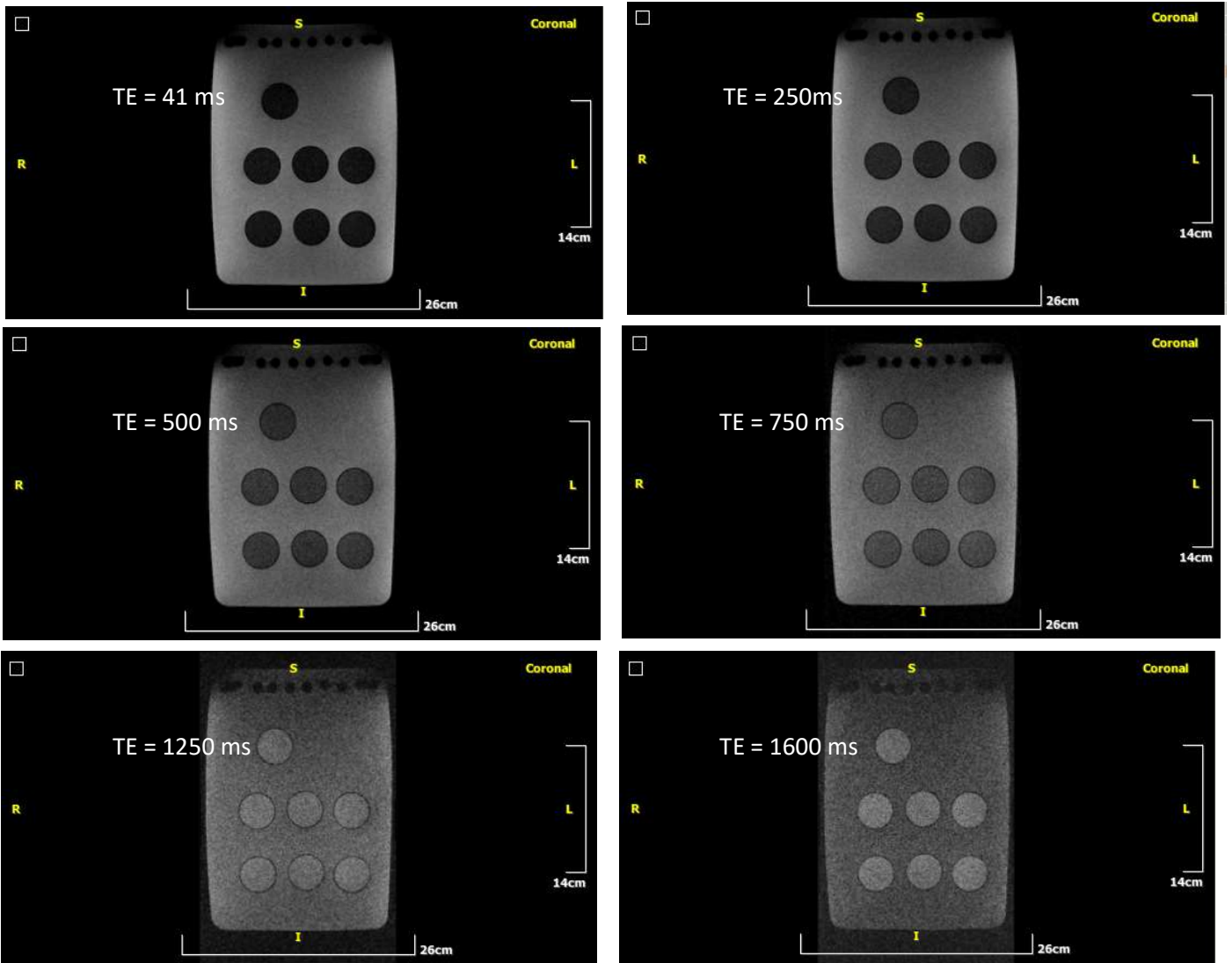


Figure 34 : Images at TE : 50, 250, 500, 750, 1250, 1600 ms obtained from the MESE sequence at temperature, $T = 37\text{ }^{\circ}\text{C}$.

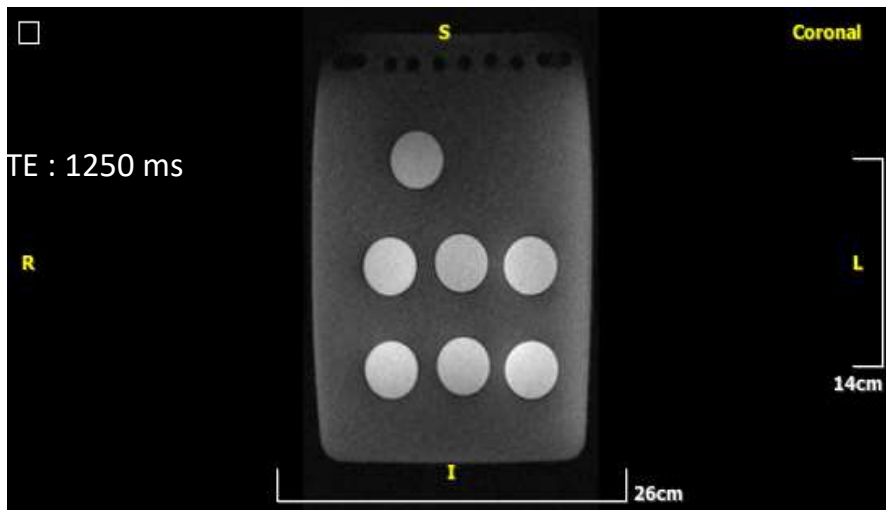
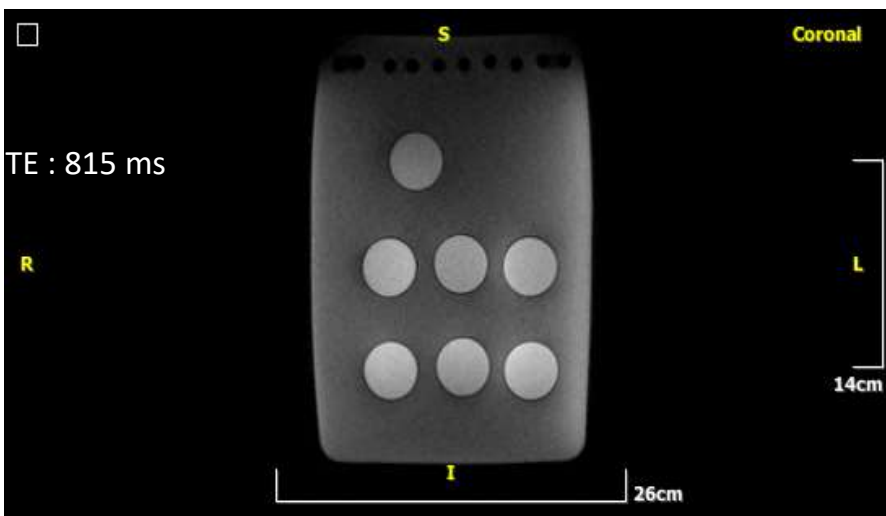
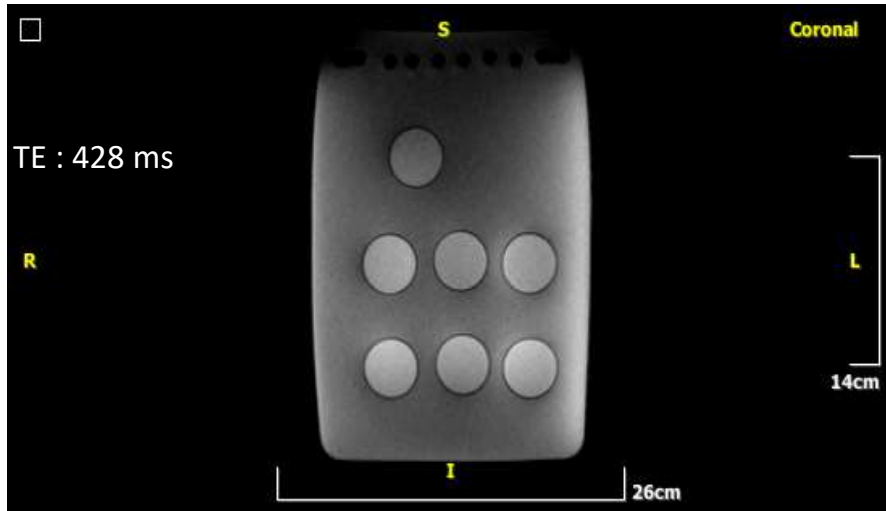
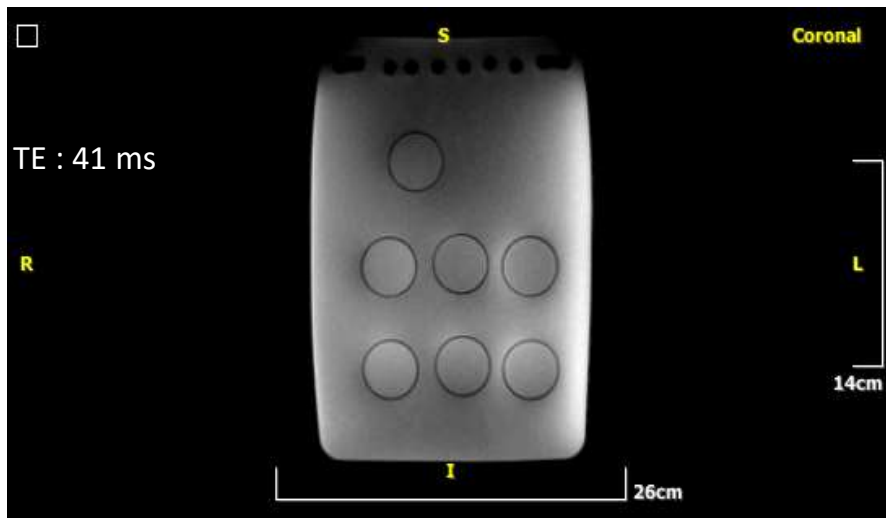


Figure 35 : Images at TE : = 41, 428, 815 and 1250 ms obtained from the HASTE sequence, at temperature, T = 45 °C.

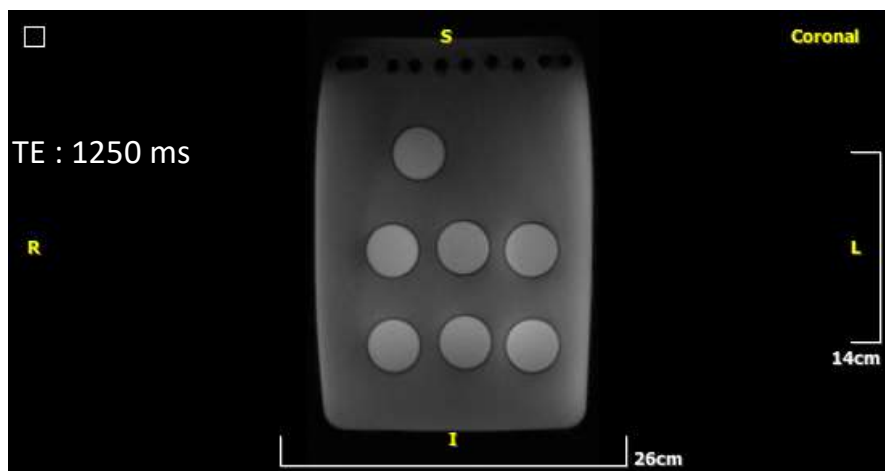
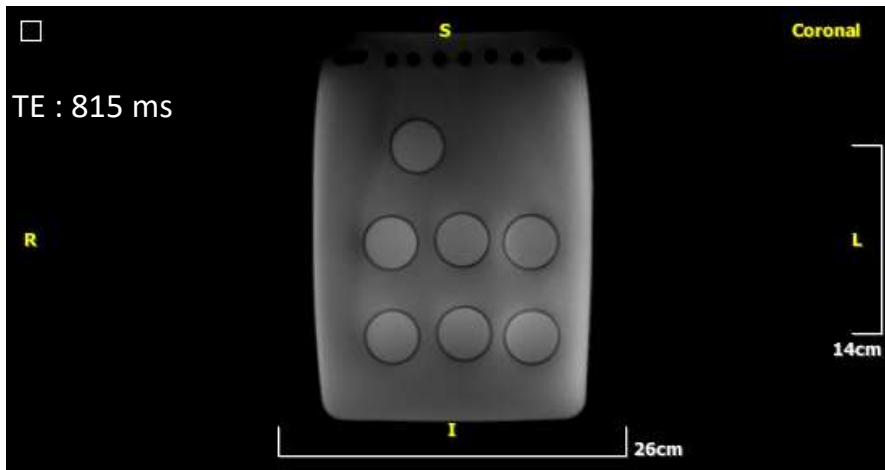
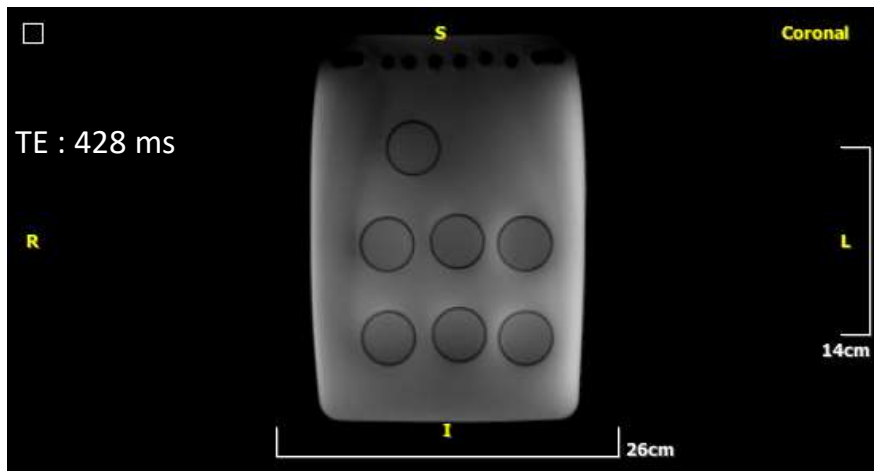
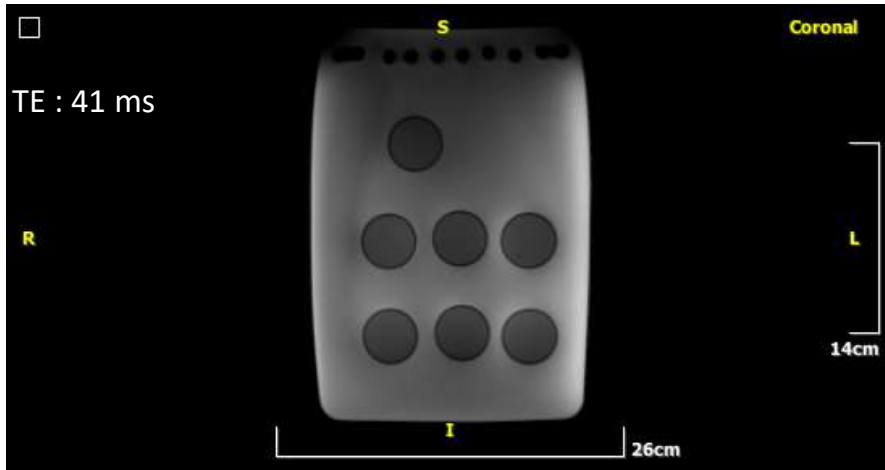


Figure 36 : Images at TE : = 41, 428, 815 and 1250 ms obtained from the HASTE sequence (32 NEX), at temperature, T = 45 °C.

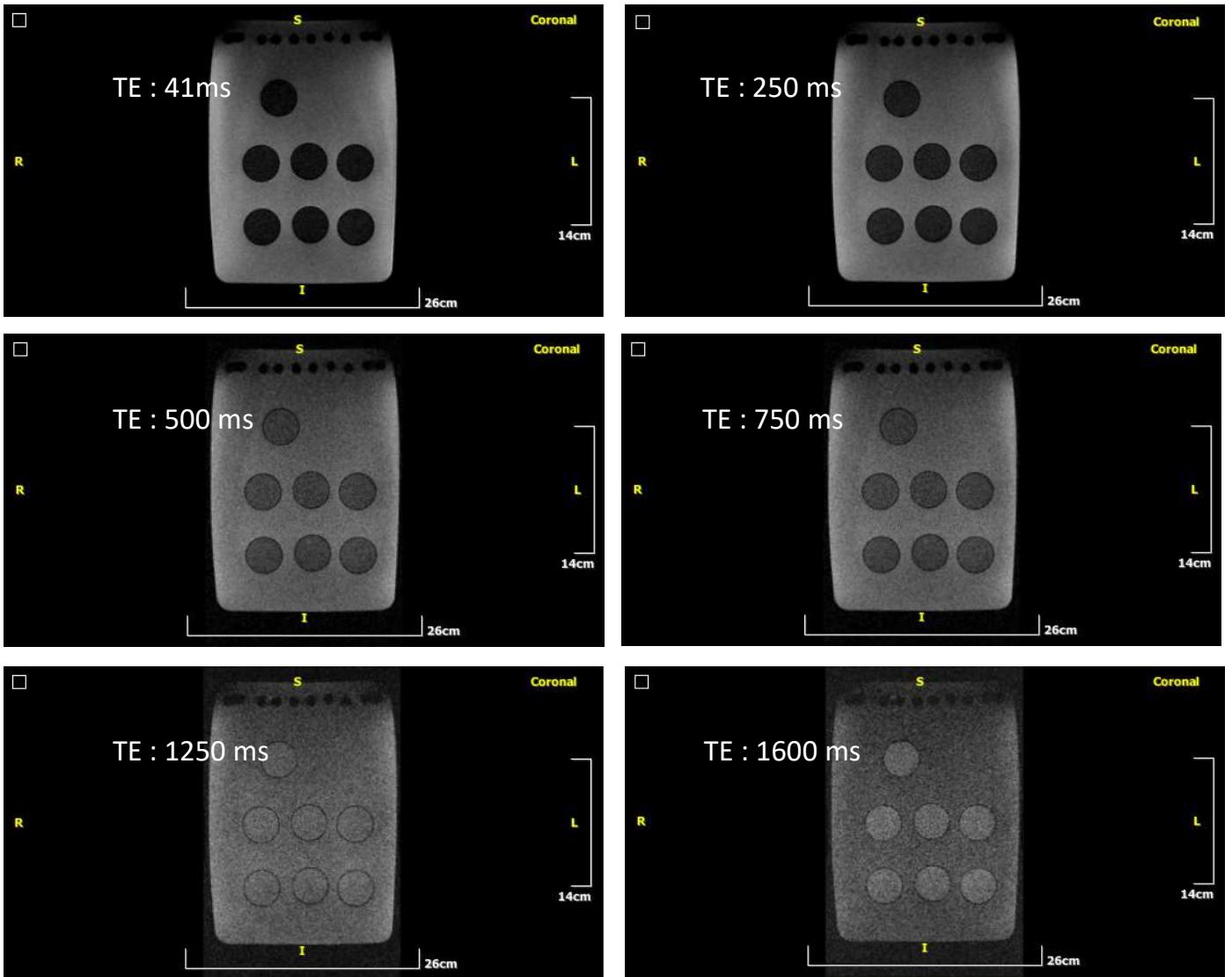


Figure 37 : Images at TE : 50, 250, 500, 750, 1250, 1600 ms obtained from the MESE sequence at temperature, $T = 45\text{ }^{\circ}\text{C}$.

2.6.4 MR Data Handling and Quantitative Image Analysis.

Coronal MRI images for each temperature, obtained from the HASTE and MESE sequences, were transferred by a Local Area Network (LAN) to a separate workstation over a dedicated research RIS/PACS platform (Evorad RIS/PACS system, Athens, Greece). Advanced image post-processing algorithms for the calculation of T2 and PD color maps were used utilizing an in-house image post-processing tool (QMRI utilities – X) designed for this purpose by Georgios Kalaitzakis (GK) and Thomas G. Maris (T.G.M).

T2 parameter values for each voxel were obtained by fitting an exponential decay curve to the signal intensity of the corresponding voxels in the image stack vs. TE time (voxel T2 relaxation decay curve). In this way, a corresponding quantitative T2 parameter map was obtained on a voxel – by – voxel basis. As TE is extended, the signal intensities in the images decreases as described by equation (52). Thus, all T2 relaxation decay curves were analyzed assuming nonlinear monoexponential decay behavior with the presence of signal offset, which is in fact the actual image background. (Eq. 52). T2 decay signal for each voxel (x, y, z) were fitted to Eq. 53.

$$S(TE_i)_{xyz} = Bg + M_0(T_1, p)_{xyz} \cdot e^{-(TE_i/T_2)xyz} \quad (52)$$

$$\ln \{(S(TE_i)_{xyz} - Bg)\} = \ln (M_0(T_1, p)_{xyz}) - \left(\frac{1}{T_2}\right) \cdot TE_i \quad (53)$$

The subscript (i) correspondsto the i^{th} image of the stack with echo time TE_i . The term $M_0(T_1, p)_{xyz}$ is the signal saturation factor for the voxel (xyz) and p is the signal producing proton density. The term is written as follows: .

$$M_0(T_1, p)_{xyz} = p \cdot \left(1 - e^{-\left(\frac{TR}{T_1}\right)}\right) \quad (54)$$

As any echo has the same TR/T_1 dependence, it can be assumed that the term $M_0(T_1, p)_{xyz}$ is proportional to the mobile proton density, p . Also, the term Bg represents the actual image background offset for the whole image stack. For all fits, the coefficient of determination, $r^2 > 0,85$.

2.6.4.1 Weighted least squares (WLS) regression.

The standard deviation, SD , of each data point $(Y_i)_{xyz} = \ln (S(TE_i)_{xyz} - Bg)$ (Net log voxel signal intensity) is given by the following error propagation formula :⁴³

$$SD(Y_i)_{xyz} = \frac{\sqrt{\sigma_{Bg}^2 + \sigma_{S(TE_i)_{xyz}}^2}}{S(TE_i)_{xyz} - Bg} = \frac{\sqrt{2} \cdot \sigma_{Bg}}{S(TE_i)_{xyz} - Bg} \quad (55)$$

As indicated from the previous equation the standard deviation of each data point increases with TE. The term σ_{Bg} represents the SD of the signal in the background of the image. Since the assumption of homoscedasticity is violated, weighted linear regression was used to maximize the efficiency of T2 estimation. According to this method, the optimum fit to the data will be to find values of slope $a = -\left(\frac{1}{T_2}\right)$ and intercept $b = \ln(M_0(T_1, p)_{xyz})$ that minimize the weighted sum of the squares of the deviations or residuals between the observed $(Y_i)_{xyz}$ and the functional portion of the regression line. The sum of the weighted squared residuals, WSS is expressed mathematically as :⁴³

$$WSS = \sum W(Y_i)_{xyz} \cdot ((Y_i)_{xyz} - \alpha - b \cdot TE_i)^2, W(Y_i)_{xyz} = \left(\frac{1}{SD(Y_i)_{xyz}}\right)^2 \quad (56)$$

In this weighted sum of squares, the relevant weighting factor $W(Y_i)_{xyz}$ is inversely proportional to the corresponding variance. Thus, data points with small error variance have a large weight and data points with higher variance are given lower variances. The relevant weighting factor can be expressed as shown in equation (57) :

$$W(Y_i)_{xyz} = \left(\frac{1}{SD(Y_i)_{xyz}}\right)^2 \xrightarrow{\text{equation (55)}} W(Y_i)_{xyz} = \frac{1}{2} \cdot \left[\frac{S(TE_i)_{xyz} - Bg}{\sigma_{Bg}}\right]^2 \quad (57)$$

The above method applied for quantitative voxel – based parametric T2 analysis is the T2qMRI technique used in this study. The above analysis was performed for all voxels of the image stack in order to create a T2 parametric image map for each temperature. So, a parametric map was generated that displayed each pixel's T2 value. The dynamic range of the resultant map was 12 bits, which corresponds to a 0 - 4095 ms direct T2 measurement scale. The same method for constructing T2 maps was applied in each imaging sequence (HASTE, HASTE (32 NEX), MESE).

Finally, using the above method of weighted linear regression , the intercept of the fitted line (equation 53) was calculated on a voxel – by – voxel basis. However, according to equation (54) the intercept of the regression line is proportional to the proton density. In this way, Proton density (PD) maps were created for each temperature. As before, the dynamic range of the map was 12 bits, which corresponds to a 0 - 4095 direct PD measurement scale in arbitrary units (AU). Again, the method for constructing PD maps was applied in each imaging sequence (HASTE, HASTE (32 NEX), MESE).

2.6.4.2 Random noise estimation from the image.

The term Bg in equations (52), (53) was calculated from a non – signal – producing region of interest (Bg – ROI) outside the actual image (signal of no interest), avoiding any prominent artifact. Its value was obtained from the last echo and it was equal to the mean background signal intensity. The same echo was used to estimate the T2 image stack random noise figure, which was expressed as the SD from the Bg – ROI ($SD Bg$). The last echo on HASTE sequence was the 4th echo and on MESE sequence was the 32nd echo. The SD from the Bg – ROI was multiplied by the Rayleigh factor

($R_f = 1,5267$) which arises when any Gaussian noise present on the raw data is centered about zero. When the magnitude image is reconstructed from the raw measurements by a 2D Fourier transform, the resultant SD of the background signal intensity (random noise) is underestimated by a factor of 1,5267. The R_f factor compensated for this effect. The SD from the $Bg - ROI$ can be expressed as

$$SD Bg = R_f \cdot SD Bg_e, \quad e = 4 \text{ or } 32 \quad (58)$$

where $SD Bg_e$ is the SD (random noise) obtained from $Bg - ROI$ on the last echo (e) of the T2 image stack. As an example, a $Bg - ROI$ which was used is shown below

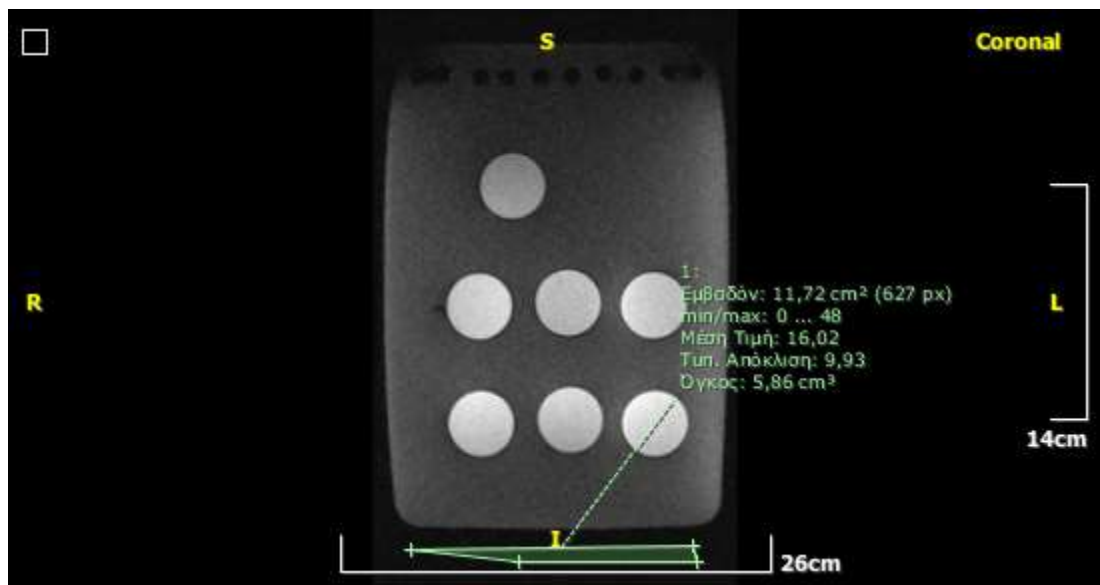


Figure 38 : The last echo (4_{th}) image at TE=1250 ms obtained with the HASTE sequence. The background ROI ($Bg - ROI$) is positioned parallel to the phase encoding direction, covering an area surface of $11,72 \text{ cm}^2$ (627 pixels). The ROI provides a measurement of the average background signal intensity (Bg) which in this case is equal to 16,02 in arbitrary units. $SD Bg_e$ is equal to 9,93 ,again in arbitrary units.

2.6.4.3 Measurements of T2 /PD on T2/PD parametric maps.

The same process for calculating T2 and PD was applied to the obtained T2 and PD maps for each temperature. Specifically a circular Region of Interest (ROI) was manually set on each sample, and a single T2/PD value was calculated from the average signal intensities within that ROI. Of course, the standard deviation of a ROI measures the dispersion of T2/PD values around the mean within that ROI. The number of each ROI corresponds to a particular sample phantom (Table 1, page 45).The total number of ROIs was 8. The EVORAD workstation was used for image handling and ROI measurements. Color maps based on the “NIH” and “Fire” Look up table (QMRI Utilities – X) were used for graphical representation of T2 and PD values respectively. By convention lower T2 values are depicted as dark and higher values are depicted as red. Similarly, lower PD values are represented as dark and higher values are depicted as light orange. Color is preferred as a means to improve visual conspicuity for the actual measurements of T2 and PD values. The accepted pixel

value segmentation levels for the T2 and PD measurement was 300–4000 ms and 1–1000 AU respectively. The T2 and PD color parametric maps obtained from the two different imaging sequences (HASTE and MESE) at 25°C are shown below.

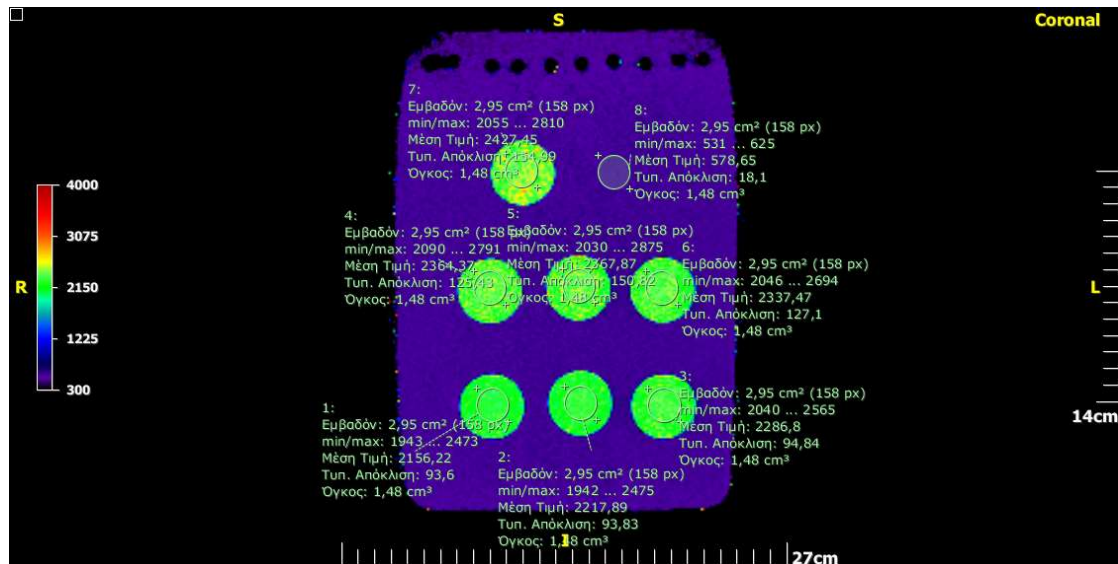


Figure 39 : The T2 color parametric map obtained with the HASTE sequence at 25°C. 8 circular ROIs were manually set on each sample. Each ROI provides a measurement of the average T2 relaxation time (in ms) of the corresponding sample phantom and covers an area of $2,95 \text{ cm}^2$.

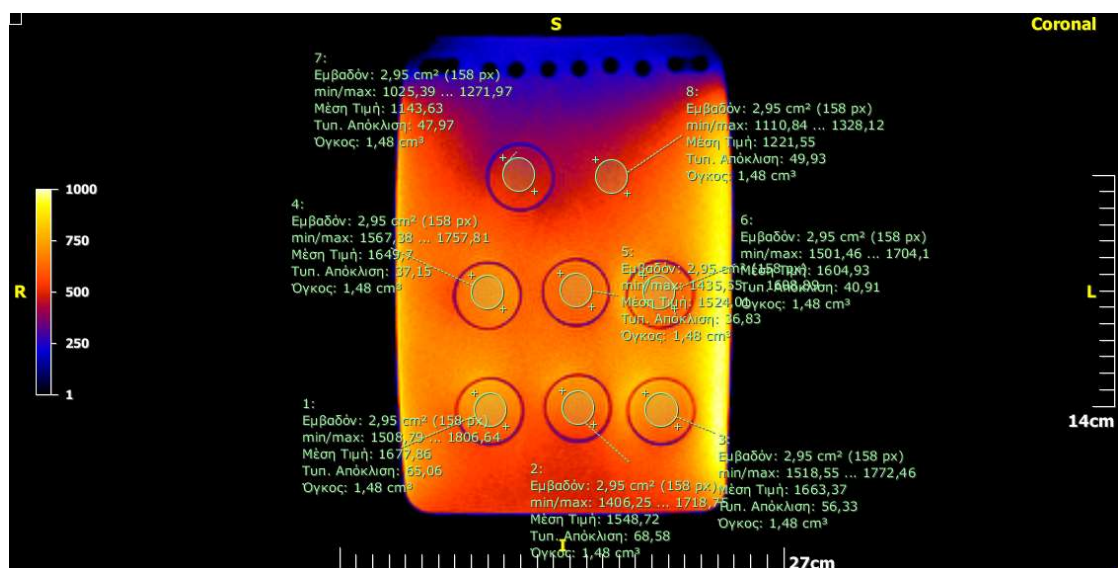


Figure 40 : The PD color parametric map obtained with the HASTE sequence at 25°C. 8 circular ROIs were manually set on each sample. Each ROI provides a measurement of the average PD relaxation time (in AU) of the corresponding sample phantom and covers an area of $2,95 \text{ cm}^2$.

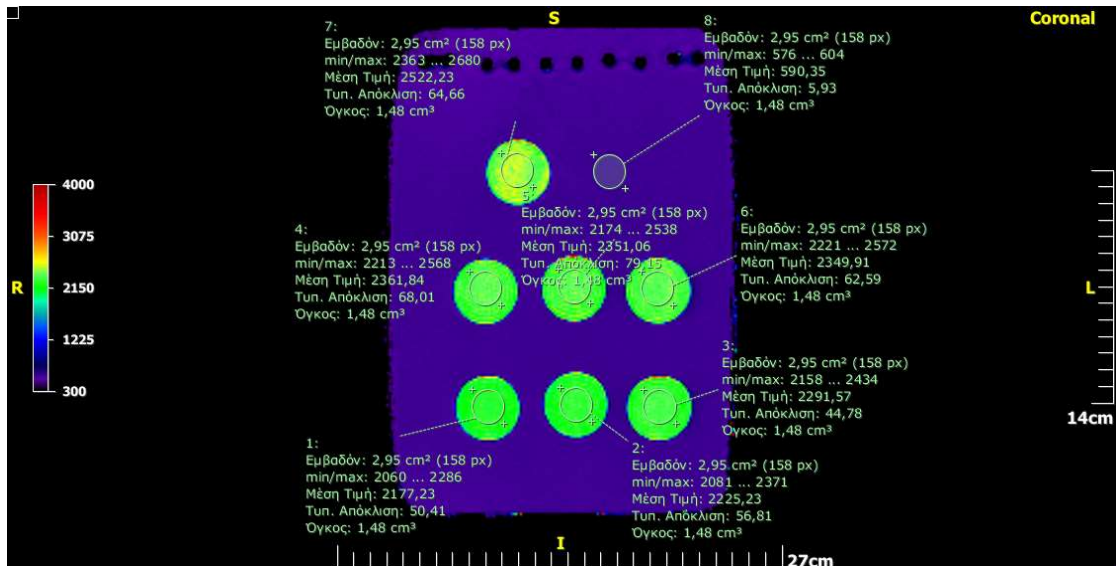


Figure 41 : The T2 color parametric map obtained with the HASTE (32 NEX) sequence at 25°C.

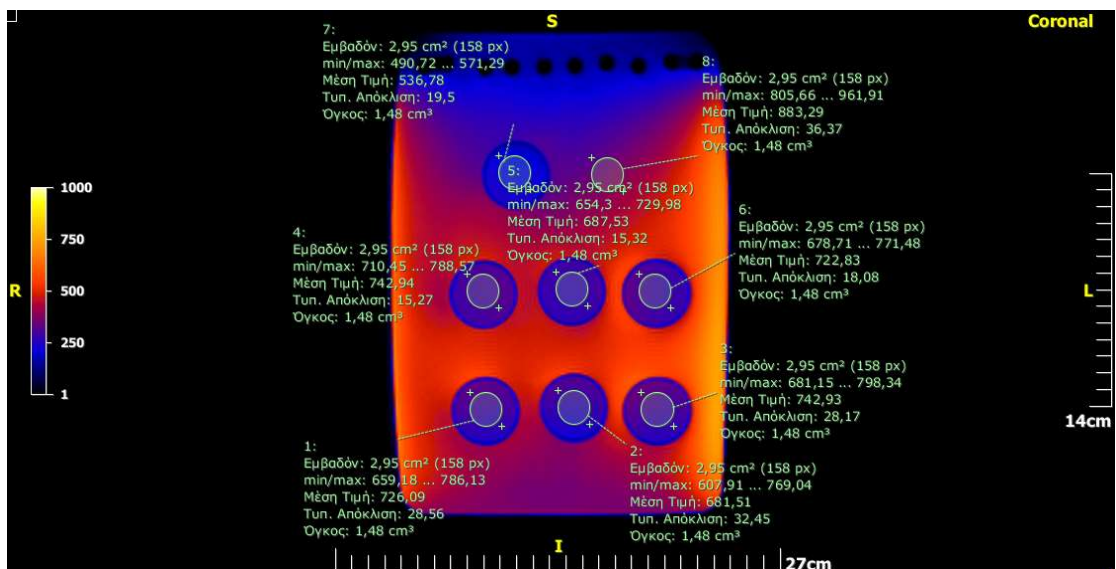


Figure 42 : The PD color parametric map obtained from HASTE (32 NEX) sequence at 25°C.

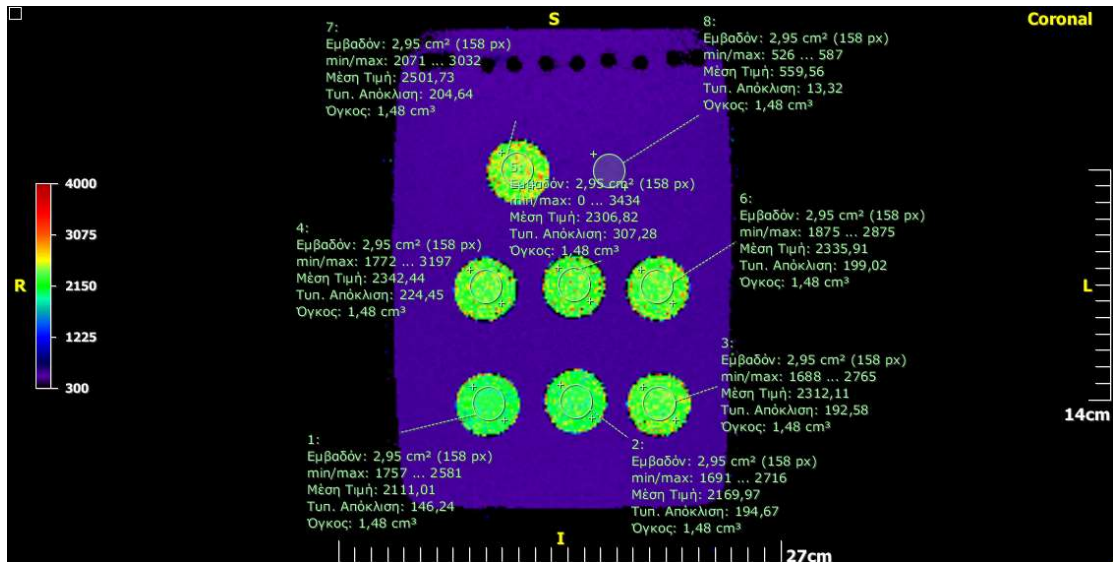


Figure 43 : The T2 color parametric map obtained with the MESE sequence at 25°C.

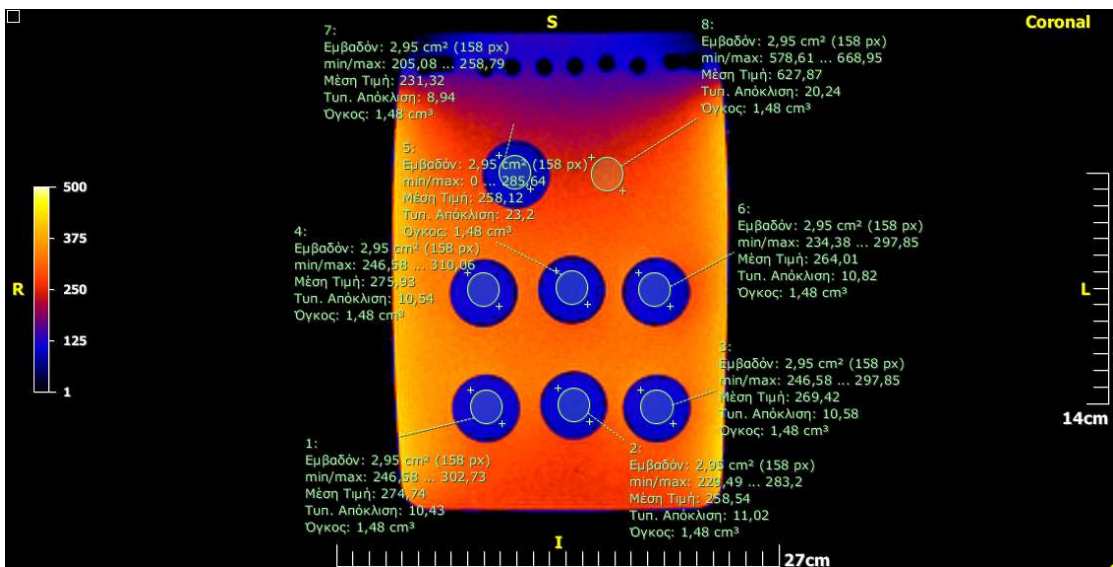


Figure 44 : The PD color parametric map obtained with the MESE sequence at 25°C.

2.6.4.4 Data handling and Analysis.

MR parameter measurement data were handled and analyzed using MedCalc (Mariakerke, Belgium) software. Although of all different normality tests is low for small sample size,^{44,45} our data was tested with two different methods: Graphical and numerical (statistical test).

Particularly, the Shapiro – Wilk (SW) test was used to decide if our data was sampled from a normal (Gaussian) distribution. SW is the most sensitive normality test followed by other tests (i.e. Kolmogorov – Smirnov (KS) test, Anderson – Darling (AD) test, Chi squared test, D’Agostino Pearson test etc) when the sample size is small ($n < 50$).⁴⁶ In other words this test has high statistical power because it can reject the null hypothesis of normality at the smallest sample size.^{44,47} In contrast, KS test requires a larger data sample to accept the alternative hypothesis.⁴⁶ From many researchers, WS test is recommended as the ideal choice for normality testing. Finally, from a comparison between four different normality tests (SW, KS, AD and Lilliefors) SW was considered as the most powerful test whereas KS was the least powerful test.^{44,45,46,47} The (SW) statistic for normality is defined as:⁴⁸

$$SW = \frac{(\sum_{i=1}^n a_i \cdot x_i)^2}{\sum_{i=1}^n (x_i - \bar{x})^2} \quad (59)$$

where the x_i are the ordered sample values and a_i are constants (or weights) generated from the covariances, variances and means of the sample of size n from a normal distribution. The value of SW lies between zero and one. Small values are evidence of departure from normality and a value close to one indicates normality of the data. Furthermore, the null hypothesis of a normal distribution is rejected if the p – value is less than or equal to α which is the significance level and equals to 0,05 in our study.⁴⁹

The graphical tool which was utilized to assess if the data is normally distributed was the Q – Q or quantile – quantile plot. A normal q – plot can indicate departure from normality. The horizontal axis of the plot shows the z scores of the observed values, and the vertical axis shows the expected z scores of the observed values under the assumption that they are originate from a normal distribution. If the sample data on the plot fall on or near a straight line, then the data are near a Normal distribution.^{45,50}

Box and whisker plots were used as a graphical tool to identify possible outliers in our data. A data point which is located outside the whiskers of the box plot can be considered as an outlier. Particularly, an outlier is an observation that is numerically smaller than the lower quartile (Q_1) minus 1.5 times the interquartile range (IQR = $Q_3 - Q_1$) or, larger than the upper quartile plus 1.5 times the interquartile range.^{45,51}

Correlations among measurable parameters were estimated by means of standard linear and nonlinear regression (Relationship between EC and T2, relationship between EC and temperature, see Results). Additionally, the Pearson correlation coefficient was used to indicate the strength of the linear relationship between the variables.

3. RESULTS

3.1 T2 relaxation time vs temperature and EC measurements

The dependence of T2 was investigated over a wide range of temperatures (20°C – 45°C) on the sample phantoms. The T2 values were measured for all the sample phantoms with respect to each degree of temperature. More specifically, different T2 maps on a voxel by voxel basis were created for each temperature using two MRI sequences:

1) A coronal single slice Multi Echo Spin Echo with different echo time (TE) acquisitions (MESE, TR/TE1/TE32/FA : 2000 ms/ 50 ms/ 1600 ms/ 180°) pulse train sequence (PHAPS technique) was applied in 32 symmetrically radiofrequency (RF) spin echoes.

2) A coronal single slice 2D Half – Fourier Acquisition Single – Shot Turbo spin – Echo (HASTE) with four different effective echo time acquisitions (TR/TE1/TE4/FA : inf/ 41ms/ 1250 ms/ 90 °). One signal average (In that case the sequence is named as HASTE) and thirty two signal averages (In that case the sequence is named as HASTE 32NEX) were used. On the maps obtained utilizing these three MRI sequences, a ROI was set on each sample and then T2 and proton density (PD) values were calculated for each temperature.

Data is presented separately for each kind of sample phantom. Specifically, T2 values regarding different concentration of sodium chloride solution (% w/v) and tap water as a function of temperature are summarized in Table 2, 3 and 4. Each table corresponds to a different T2 – mapping technique.

Table 2: T2 measurements of the salt solutions and of the tap water samples at various temperatures. All T2 values were acquired using the HASTE sequence.

<i>T2 (msec) – HASTE sequence</i>							
<i>NaCl (% w/v)</i>							<i>Tap water</i>
<i>T (°C)</i>	<i>0,2%</i>	<i>0,4%</i>	<i>0,6%</i>	<i>0,8%</i>	<i>0,9%</i>	<i>1%</i>	<i>–</i>
20	2044,9	2056	2140,3	2196,8	2198,1	2173,1	2296,9
25	2156,2	2217,9	2286,8	2364,4	2367,9	2337,5	2427,4
30	2236,7	2375,2	2414,1	2506,2	2494,3	2470,3	2485,8
35	2443	2555,4	2633,3	2724,3	2719,4	2704,6	2745,8
37	2499,4	2621,3	2701,6	2754,3	2776,4	2775,4	2924,8
40	2558,5	2794,7	2792,7	2846,6	2895,1	2835,8	2909,4
42	2573,6	2755,3	2786,2	2864,6	2869,5	2831,3	2846
45	2676,2	2824,1	2865,2	2963	2999,3	2894,6	3051,9

Table 3: T2 measurements of the salt solutions and of the tap water samples at various temperatures. All T2 values were acquired using the HASTE (32 NEX) sequence.

<i>T2 (msec) – HASTE (32NEX) sequence</i>							
<i>NaCl (% w/v)</i>							<i>Tap water</i>
<i>T (°C)</i>	0,2%	0,4%	0,6%	0,8%	0,9%	1%	–
20	2052,1	2046,8	2109,2	2175,4	2160,2	2163,1	2304,6
25	2177,2	2225,2	2291,6	2361,8	2351,1	2349,9	2522,2
30	2323,2	2402,2	2465,8	2539,3	2517,1	2514,1	2660,9
35	2507,6	2643,5	2684,3	2763,7	2764,3	2727,4	2867,6
37	2527,8	2653,9	2731,8	2786,6	2812,7	2808,8	2978,5
40	2656,9	2816,1	2836,9	2922,8	2949,5	2881,8	3070,9
42	2703,9	2900,3	2888,4	2978,2	3011,4	2947,5	3140,7
45	2781,9	2981	3015,1	3130,2	3119,9	3012,9	3216,1

Table 4: T2 measurements of the salt solutions and of the tap water samples at various temperatures. All T2 values were acquired using the MESE sequence.

<i>T2 (msec) – MESE sequence</i>							
<i>NaCl (% w/v)</i>							<i>Tap water</i>
<i>T (°C)</i>	0,2%	0,4%	0,6%	0,8%	0,9%	1%	–
20	1975,5	1957,9	2050,4	2105,7	2049,6	2089,3	2233,2
25	2111	2170	2312,1	2342,4	2326,7	2335,9	2501,7
30	2223,8	2288,2	2493,2	2505,6	2490,3	2515,5	2628
35	2476,6	2554,2	2691,6	2852,3	2672,4	2770,6	2872,8
37	2509,4	2631,5	2842,9	2833,5	2677,3	2772,9	2918,4
40	2664,1	2761,7	2878,5	2812	2622,9	2788,2	2908,4
42	2648,4	2802,9	2944	2803,5	2497,7	2763,8	2754,7
45	2676,1	2764,1	2704,3	2676,6	2353,5	2758,1	2609,4

Based on the previous tables, results for the T2 relaxation time correlation with temperature is presented graphically in the following figures. In this study, the T2 vs temperature dependence is approximated by a linear function ($y = a \cdot x + b$). The choice of equation was based on the best fit of the data (R^2 for the fits).

For obvious reasons, only 2 figures for each MRI sequence are presented below. However, the correlations of T2 relaxation time of each sample phantom with temperature are presented in Table 5, 6 and 7. Each table corresponds to a specific MRI pulse sequence.

Normality of the dependent variable which was the T2 relaxation time, was examined prior to linear least squares regression, via Shapiro – Wilk test. Also, Q-Q plots were created to determine visually if T2 relaxation time is normally distributed.

On average the Pearson correlation coefficient between all sets of data (T2 and T), for any MRI sequence (HASTE and MESE) is greater than 0,90 with P value much less than 0,05. This indicates a strong positive relationship between these two variables.

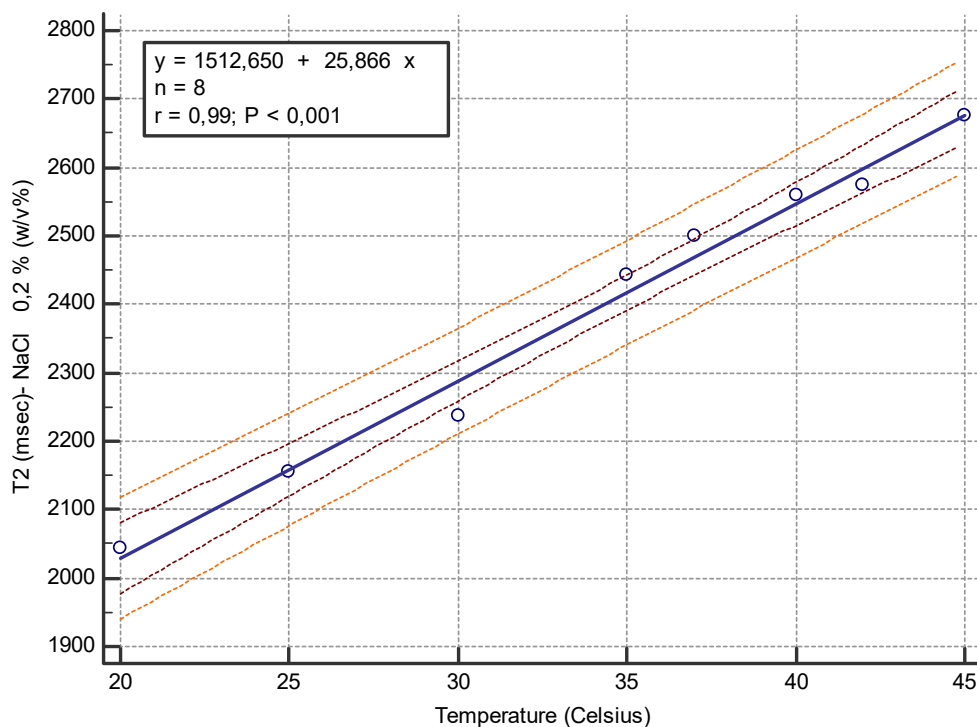


Figure 45 : Linear regression for the relationship between 0,2% (w/v%) NaCl solution T2 and temperature. The T2 values were obtained with HASTE sequence. The dashed brown curves represent the 95% confidence interval for the regression line. The dashed orange curves represent the 95% prediction interval for the regression curve.

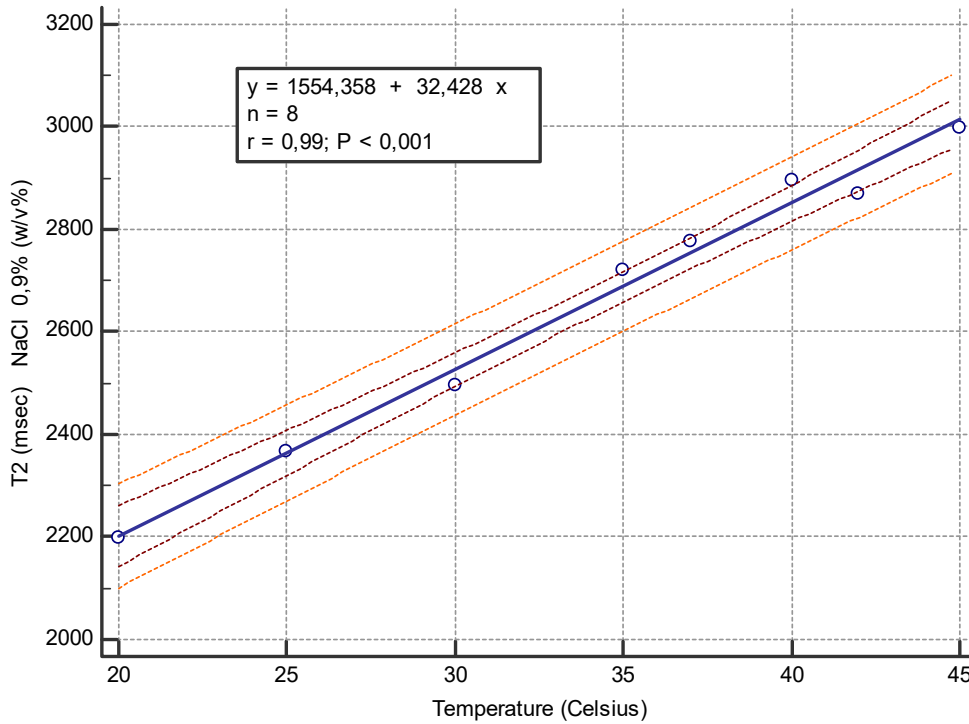


Figure 46 : Linear regression for the relationship between 0,9%(w/v%) NaCl solution T2 and temperature. The T2 values were obtained with HASTE sequence.

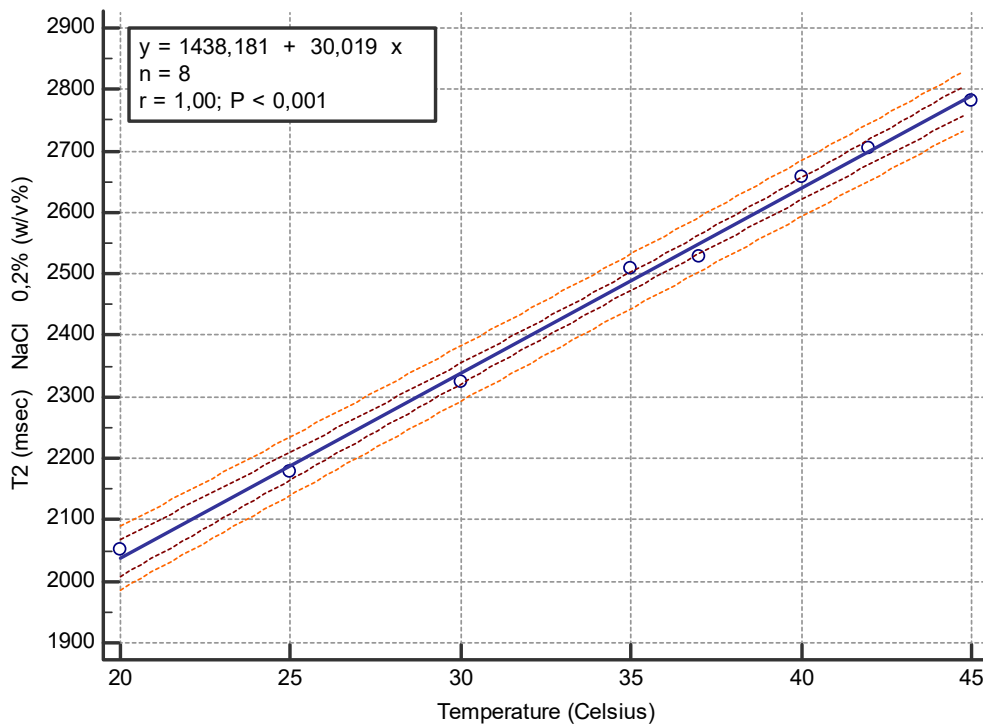


Figure 47 : Linear regression for the relationship between 0,2% (w/v%) NaCl solution T2 and temperature. The T2 values were obtained with HASTE (32 NEX) sequence.

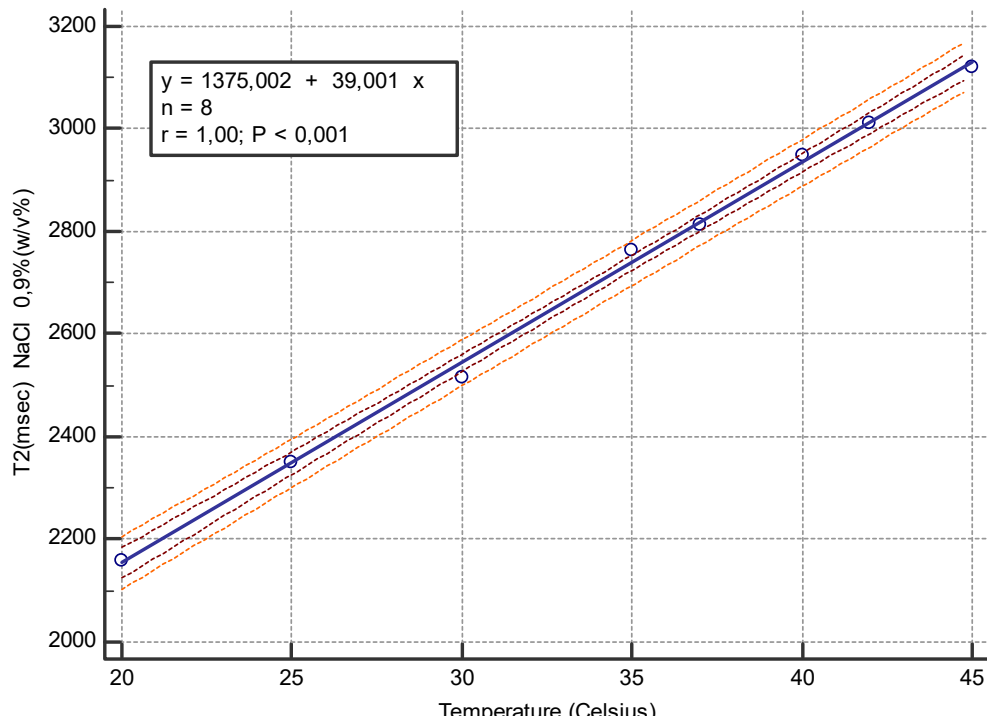


Figure 48 : Linear regression for the relationship between 0,9%(w/v%) NaCl solution T2 and temperature. The T2 values were obtained with HASTE (32 NEX) sequence.

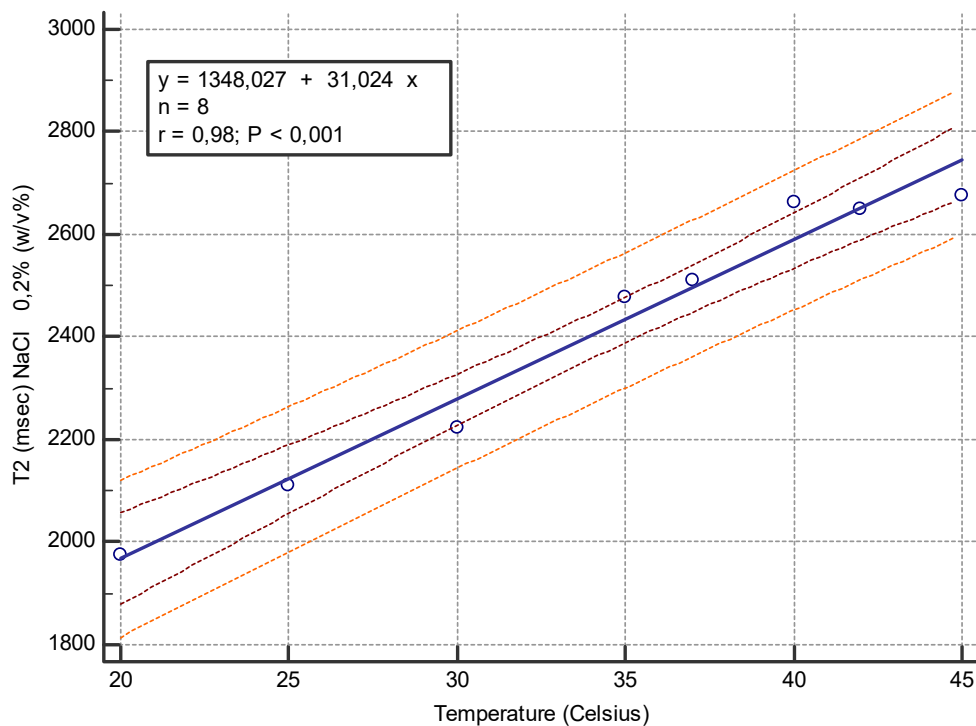


Figure 49 : Linear regression for the relationship between 0,2 %(w/v%) NaCl solution T2 and temperature. The T2 values were obtained with MESE sequence.

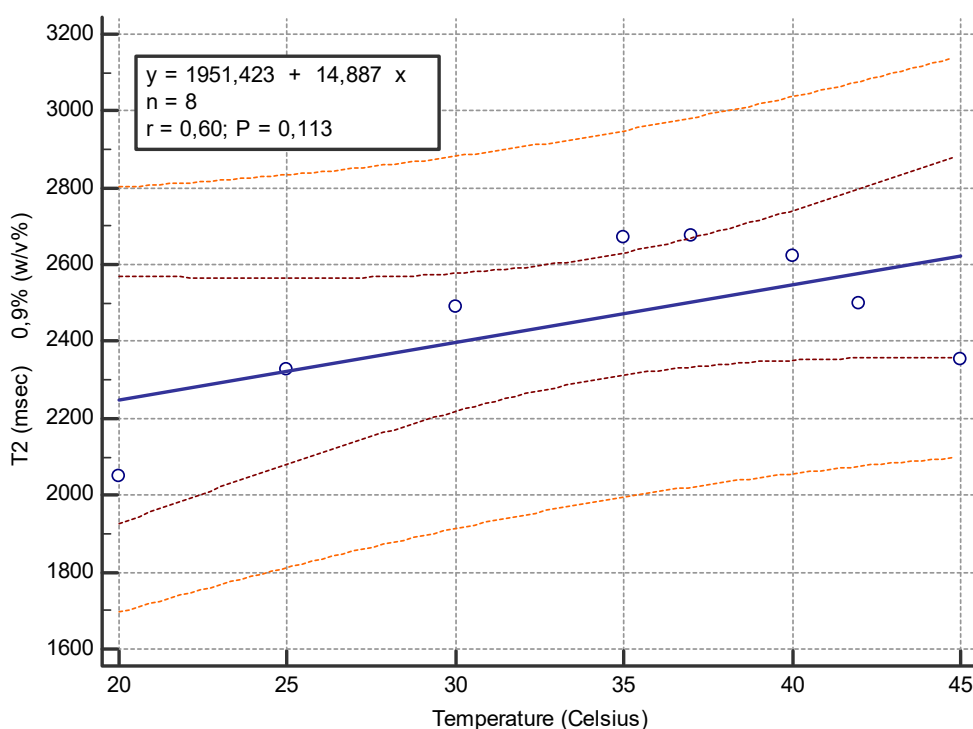


Figure 50 : Linear regression for the relationship between 0,9% (w/v%) NaCl solution T2 and temperature. The T2 values were obtained with MESE sequence

Table 5 : Correlations of NaCl solutions and tap water samples T2 with temperature, T.

<i>HASTE sequence</i>					
<i>Y axis</i>	<i>X axis</i>	<i>slope ($\frac{msec}{^{\circ}C}$)</i>	<i>Intercept (msec/°C)</i>	<i>R²</i>	<i>P</i>
<i>T2(msec) of NaCl 0,2%</i>	<i>T(°C)</i>	$25,866 \pm 1,288$	$1512,6504 \pm 45,3285$	0,9853	< 0,0001
<i>T2(msec) of NaCl 0,4%</i>	<i>T(°C)</i>	$32,4721 \pm 1,7976$	$1412,8193 \pm 63,2615$	0,9819	< 0,0001
<i>T2(msec) of NaCl 0,6%</i>	<i>T(°C)</i>	$30,4570 \pm 1,5847$	$1543,3721 \pm 55,7696$	0,9840	< 0,0001
<i>T2(msec) of NaCl 0,8%</i>	<i>T(°C)</i>	$30,9684 \pm 1,2101$	$1591,8578 \pm 42,5877$	0,9909	< 0,0001
<i>T2(msec) of NaCl 0,9%</i>	<i>T(°C)</i>	$32,4275 \pm 1,4726$	$1554,3579 \pm 51,8253$	0,9878	< 0,0001
<i>T2(msec) of NaCl 1%</i>	<i>T(°C)</i>	$30,4467 \pm 2,1179$	$1585,0254 \pm 30,4467$	0,9718	< 0,0001
<i>T2(msec) of tap water%</i>	<i>T(°C)</i>	$30,4625 \pm 3,4579$	$1667,6606 \pm 121,6908$	0,9289	= 0,0001

Table 6: Correlations of NaCl solutions and tap water samples T2 with temperature, T.

<i>HASTE (32 NEX) sequence</i>					
<i>Y axis</i>	<i>X axis</i>	<i>slope ($\frac{msec}{^{\circ}C}$)</i>	<i>Intercept (msec/°C)</i>	<i>R²</i>	<i>P</i>
<i>T2(msec) of NaCl 0,2%</i>	<i>T(°C)</i>	$30,0188 \pm 0,7465$	$1438,1826 \pm 26,2705$	0,9963	< 0,0001
<i>T2(msec) of NaCl 0,4%</i>	<i>T(°C)</i>	$38,2754 \pm 1,0394$	$1272,6940 \pm 36,5804$	0,9956	< 0,0001
<i>T2(msec) of NaCl 0,6%</i>	<i>T(°C)</i>	$36,1074 \pm 0,6558$	$1391,2090 \pm 36,1074$	0,9980	< 0,0001
<i>T2(msec) of NaCl 0,8%</i>	<i>T(°C)</i>	$37,5064 \pm 0,8425$	$1422,6558 \pm 29,6503$	0,9970	< 0,0001
<i>T2(msec) of NaCl 0,9%</i>	<i>T(°C)</i>	$39,0007 \pm 0,7443$	$1375,0021 \pm 26,1936$	0,9878	< 0,0001
<i>T2(msec) of NaCl 1%</i>	<i>T(°C)</i>	$35,0071 \pm 1,1165$	$1467,6938 \pm 39,2922$	0,9939	< 0,0001
<i>T2(msec) of tap water%</i>	<i>T(°C)</i>	$37,1213 \pm 1,0191$	$1573,7814 \pm 35,8637$	0,9955	= 0,0001

Table 7: Correlations of NaCl solutions and tap water samples T2 with temperature, T.

<i>MESE sequence</i>					
<i>Y axis</i>	<i>X axis</i>	<i>slope ($\frac{msec}{^{\circ}C}$)</i>	<i>Intercept (msec/°C)</i>	<i>R²</i>	<i>P</i>
<i>T2(msec) of NaCl 0,2%</i>	<i>T(°C)</i>	$31,0244 \pm 2,2221$	$1348,0267 \pm 78,2007$	0,9701	< 0,0001
<i>T2(msec) of NaCl 0,4%</i>	<i>T(°C)</i>	$35,8571 \pm 2,7736$	$1263,2079 \pm 35,8571$	0,9653	< 0,0001
<i>T2(msec) of NaCl 0,6%</i>	<i>T(°C)</i>	$32,6152 \pm 5,9697$	$1497,5549 \pm 210,0869$	0,8326	= 0,0016
<i>T2(msec) of NaCl 0,8%</i>	<i>T(°C)</i>	$27,2755 \pm 6,6375$	$1682,2657 \pm 233,5882$	0,7378	< 0,0063
<i>T2(msec) of NaCl 0,9%</i>	<i>T(°C)</i>	$14,8869 \pm 8,0336$	$1951,4232 \pm 282,7213$	0,3640	= 0,1133
<i>T2(msec) of NaCl 1%</i>	<i>T(°C)</i>	$28,1454 \pm 4,6953$	$1635,3070 \pm 165,2379$	0,8569	= 0,001
<i>T2(msec) of tap water%</i>	<i>T(°C)</i>	$19,4282 \pm 7,8436$	$2012,9100 \pm 276,9100$	0,5056	= 0,048

Similarly, data is presented separately for each kind of sample phantom. Specifically, proton density (PD) values regarding different concentration of sodium chloride

solution (% w/v) and tap water as a function of temperature are summarized in Table 8, 9 and 10. Each table corresponds to a different PD – mapping technique.

Referring to table 8, normality was tested in the same way as before. In almost all the cases, Shapiro – Wilk test statistic, W , is always greater than 0,95 ($P > 0,05$).

Table 8: T2 measurements of the salt solutions and of the tap water sample at various temperatures. All T2 values were acquired using the MESE sequence.

<i>PD (AU) – HASTE sequence</i>							
<i>NaCl (% w/v)</i>							<i>Tap water</i>
<i>T(°C)</i>	0,2%	0,4%	0,6%	0,8%	0,9%	1%	–
20	1721,9	1610,9	1711,9	1723,4	1612,8	1687,5	1242,6
25	1677,9	1548,7	1663,4	1649,7	1524	1604,9	1143,6
30	1608,6	1437,7	1600,5	1563	1427,7	1518,5	1056,5
35	1515,9	1370,5	1513	1454,2	1306,1	1410,9	954,8
37	1470,7	1324,9	1469,7	1395,1	1248,1	1351,9	876
40	1437	1271,4	1428,4	1358,9	1196,6	1314,1	860,5
42	1106,9	983,3	1108,5	1045,2	922,7	1007,5	659,2
45	1358,9	1204,6	1359,2	1267,9	113,9	1225,8	782,8

In table 8 the value of PD at 42°C was suspected to be a potential outlier. However, box and whisker plots were created to reject that hypothesis. Moreover, Grubb's test was performed to find a single outlier in our normally distributed data. However, no outlier was found. So, we did not exclude this data point from our measurements.

Table 9: PD measurements of the salt solutions and of the tap water sample at various temperatures. All PD values were acquired using the HASTE (32NEX) sequence.

<i>PD (AU) – HASTE (32NEX) sequence</i>							
<i>NaCl (% w/v)</i>							<i>Tap water</i>
<i>T(°C)</i>	0,2%	0,4%	0,6%	0,8%	0,9%	1%	–
20	804,1	756,3	822,1	840	791,3	826,1	628,6
25	726,1	681,5	742,9	742,9	687,5	722,8	536,8
30	673,1	627,8	692,3	687,5	630,5	667,7	492,4
35	592,6	545,7	613,1	598	538,6	576,2	417,2
37	1483,5	1337,7	1482,5	1407,9	1260,9	1364,7	888,8
40	524,4	479,8	547,5	529	469,2	506,8	363,9
42	520,1	472,9	542,4	520,4	460,2	498,3	355,8
45	483,5	439,4	502,3	476,9	418,7	455,5	322,6

Referring to table 9, the values of PD for all NaCl concentrations and tap water are not normally distributed. So, box and whisker plots were generated to examine

possible outliers in our data. For instance, the corresponding plot of the 0,2% NaCl solution (% w/v) PD measurements is shown below :

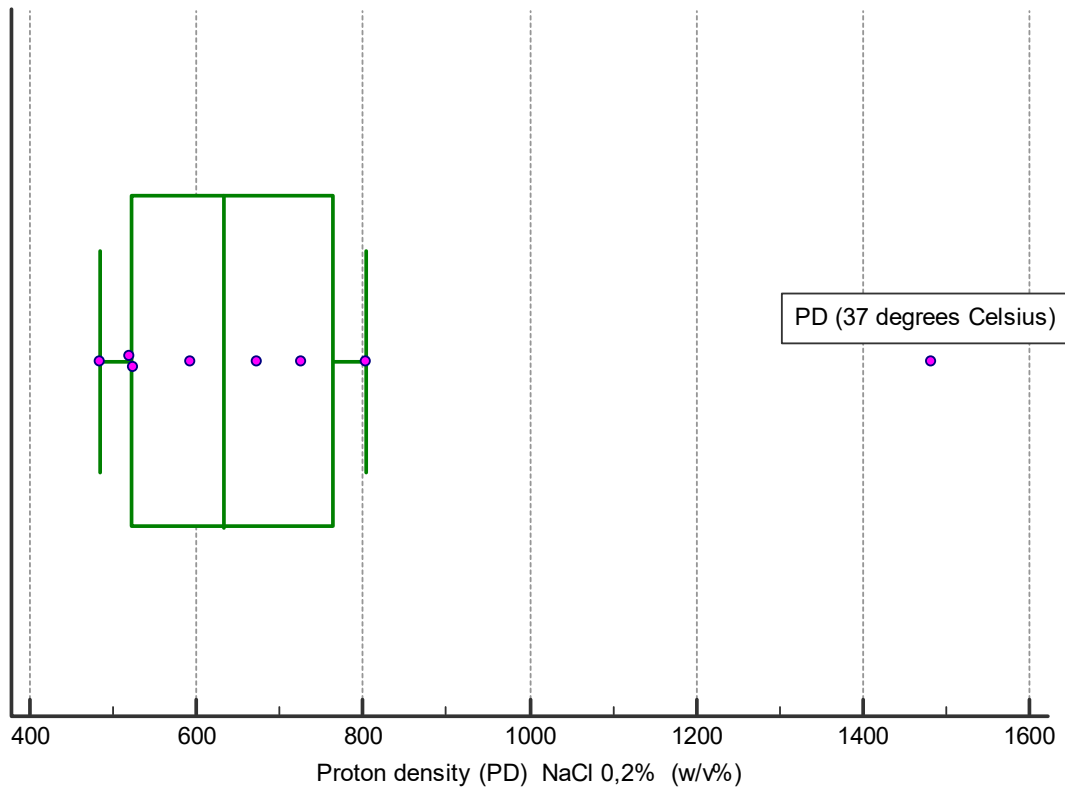


Figure 51 : Box and Whisker plot of 0,2 % (w/v) NaCl solution PD values. The value of PD at 37°C is displayed as a separate point.

Moreover, Q-Q plots were created to judge visually the normality of our PD measurements. For example, the corresponding Q-Q plot of the NaCl – 0,2% (% w/v) PD measurements is shown below :

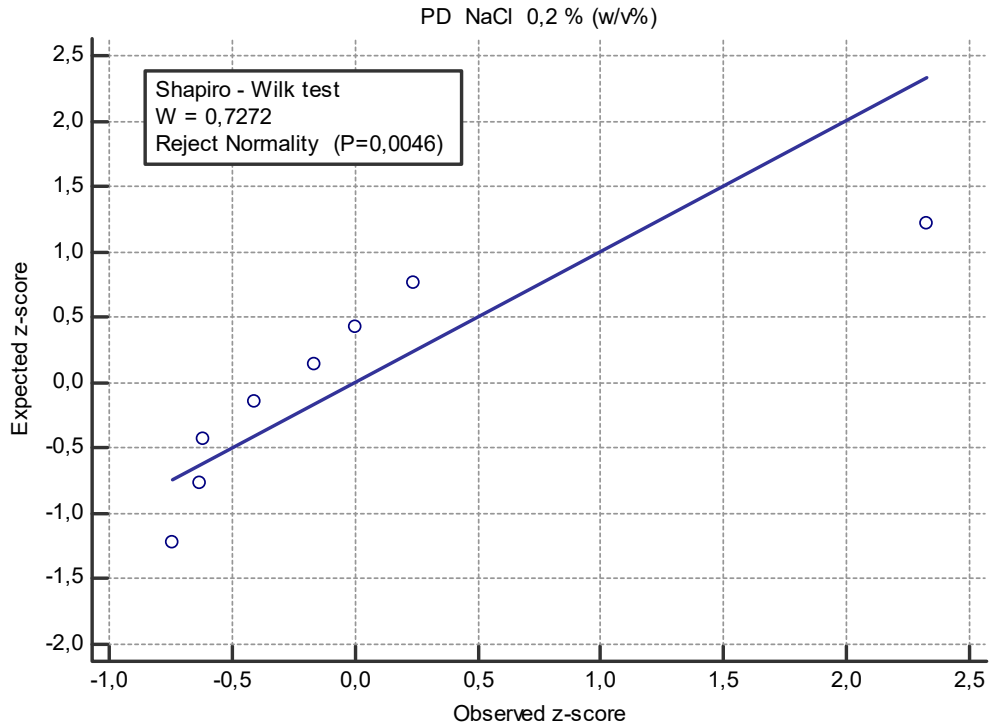


Figure 52 : Q-Q plot of 0,2 % (w/v %) NaCl solution PD values. The data is not normal since the data points deviate significantly from the reference straight line.

Based on figure 51, it is obvious that the value of PD at 37°C is an outlier and it must be excluded from our data. From figure 52, it can be concluded that PD measurements do not follow a normal distribution. However, when the value of PD measurement at 37°C is excluded from all data sets, sodium chloride and tap water PD follows the Normal distribution. On average, W is always greater than 0,9 with P value always much higher than 0,05. Thus, this specific value is excluded from our data.

Table 10 : PD measurements of the salt solutions and of the tap water sample at various temperatures. All PD values were acquired using the MESE sequence.

<i>PD (AU) – MESE sequence</i>							
<i>NaCl (% w/v)</i>							<i>Tap water</i>
<i>T (°C)</i>	0,2%	0,4%	0,6%	0,8%	0,9%	1%	–
20	317,9	302,7	317,1	323,1	317,7	277,9	628,6
25	274,7	258,5	269,4	275,9	264	231,3	536,8
30	245,1	231,3	241,3	246,8	231,6	206,7	492,4
35	203,9	191,6	203	201	235,9	167,5	417,2
37	196,6	183,2	193,9	197	193,6	160,4	888,8
40	183,3	169,8	181,9	180,1	172,2	148,1	363,9
42	174,3	157,1	174,1	171,9	160,6	139,5	355,8
45	159,1	148,5	156,3	149,3	142,8	112,4	322,6

Referring to table 10, the values of PD for all NaCl concentrations and tap water are normally distributed. On average, W is always greater than 0,9 with P value always much higher than 0,05.

Based on the previous tables, results for the Proton density (PD) correlation with temperature is presented graphically in the following figures. In this study, the PD vs temperature dependence is approximated by a linear function ($y = a \cdot x + b$). The choice of equation was based on the best fit of the data (R^2 for the fits).

The Pearson correlation coefficient between all sets of data (PD and T), for any MRI pulse sequence (HASTE and MESE) is always less than - 0,90 which indicates a negative correlation between these two variables. In addition, the calculated correlation coefficient is statistical significant because P value was always much less than 0,05.

For obvious reasons, only 2 figures for each MRI sequence are presented below. However, the correlations of PD of each sample phantom with temperature are presented in Table 12, 13 and 14. Each table corresponds to a specific MRI pulse sequence.

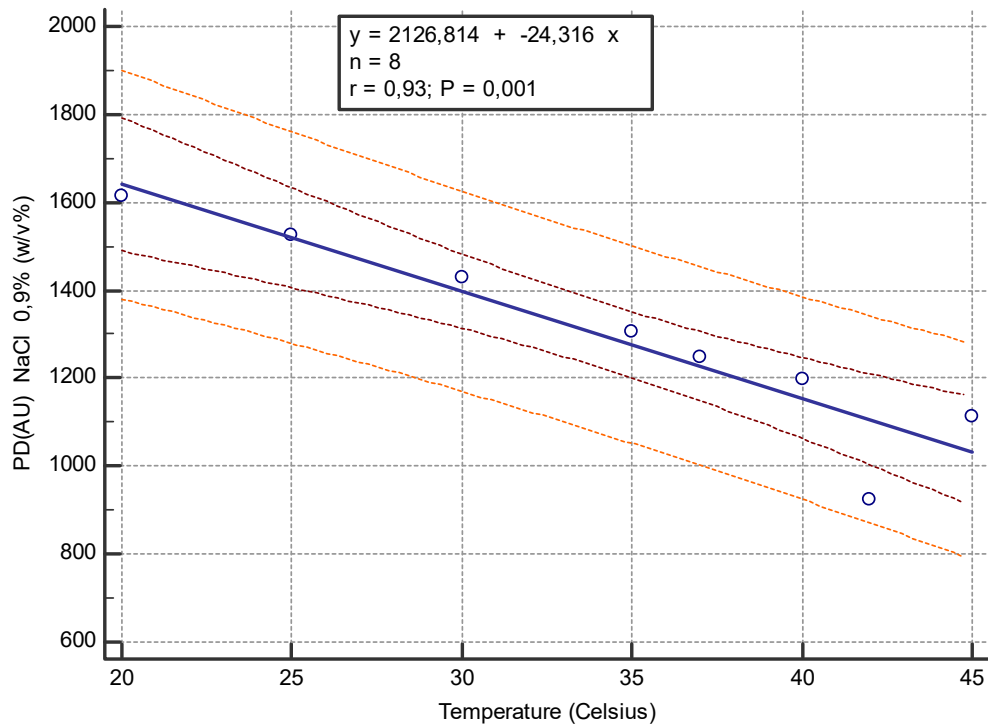


Figure 53: Linear regression for the relationship between NaCl (0,9%) PD and temperature. The PD values were obtained with HASTE sequence.

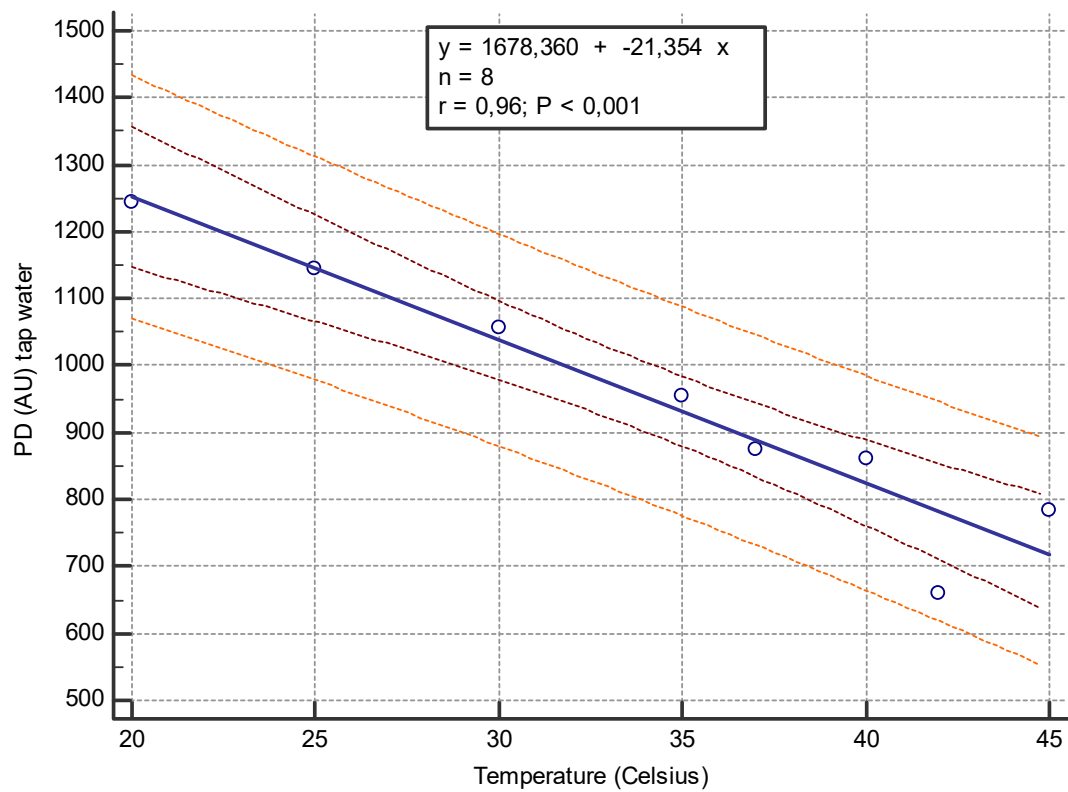


Figure 54: Linear regression for the relationship between tap water PD and temperature. The PD values were obtained with HASTE sequence.

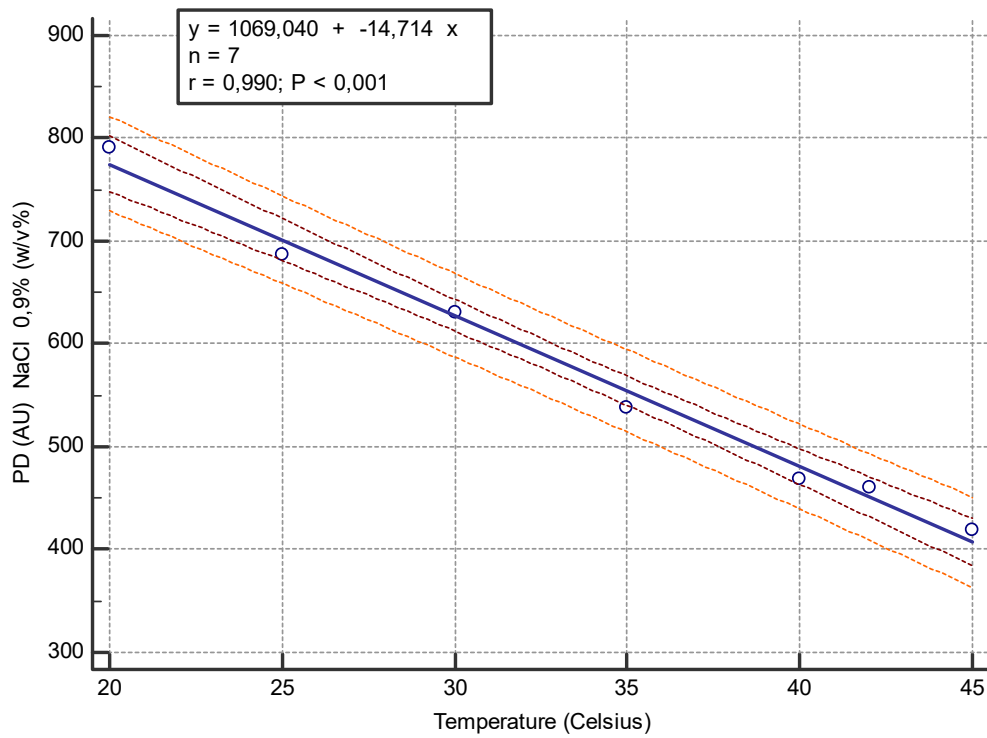


Figure 55: Linear regression for the relationship between NaCl (0,9%) PD and temperature. The PD values were obtained with HASTE (32 NEX) sequence.

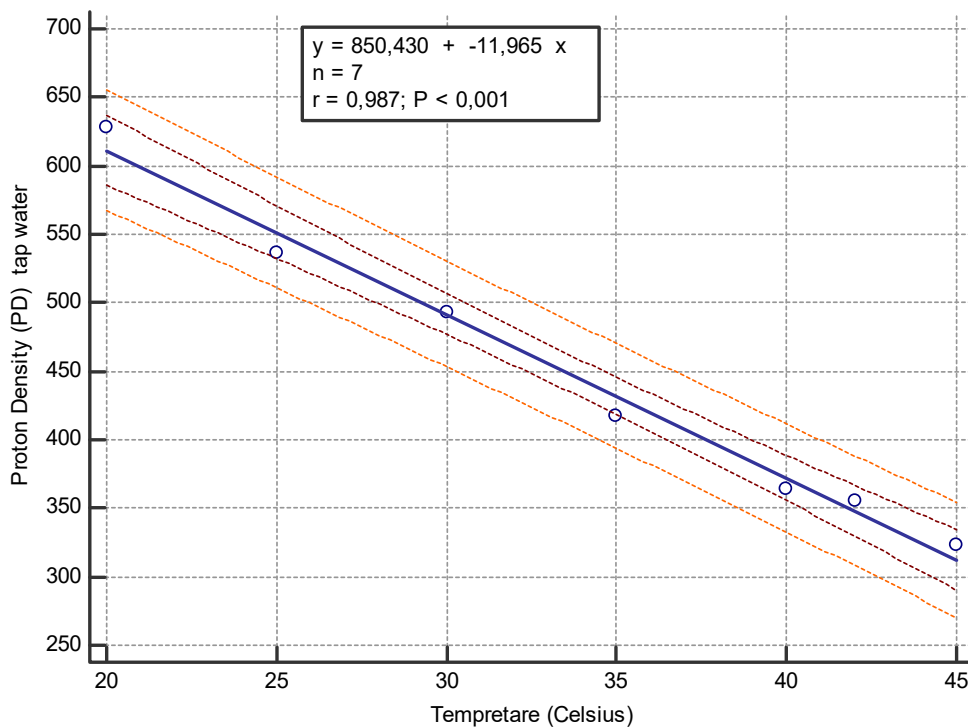


Figure 56: Linear regression for the relationship between tap water PD and temperature. The PD values were obtained with HASTE (32 NEX) sequence.

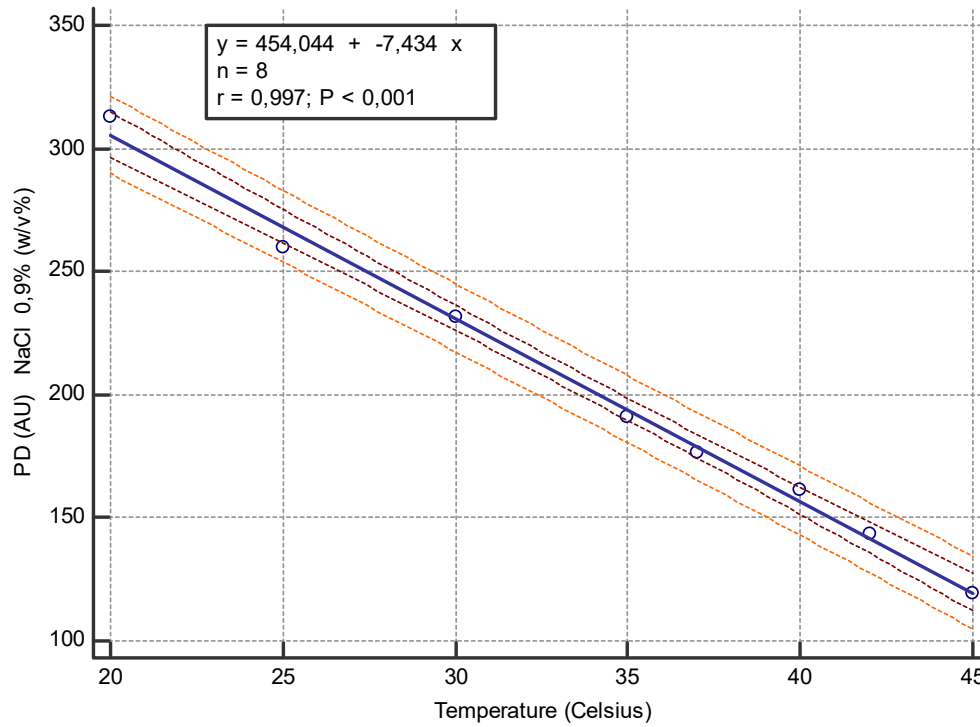


Figure 57: Linear regression for the relationship between NaCl (0,9%) PD and temperature. The PD values were obtained with MESE sequence.

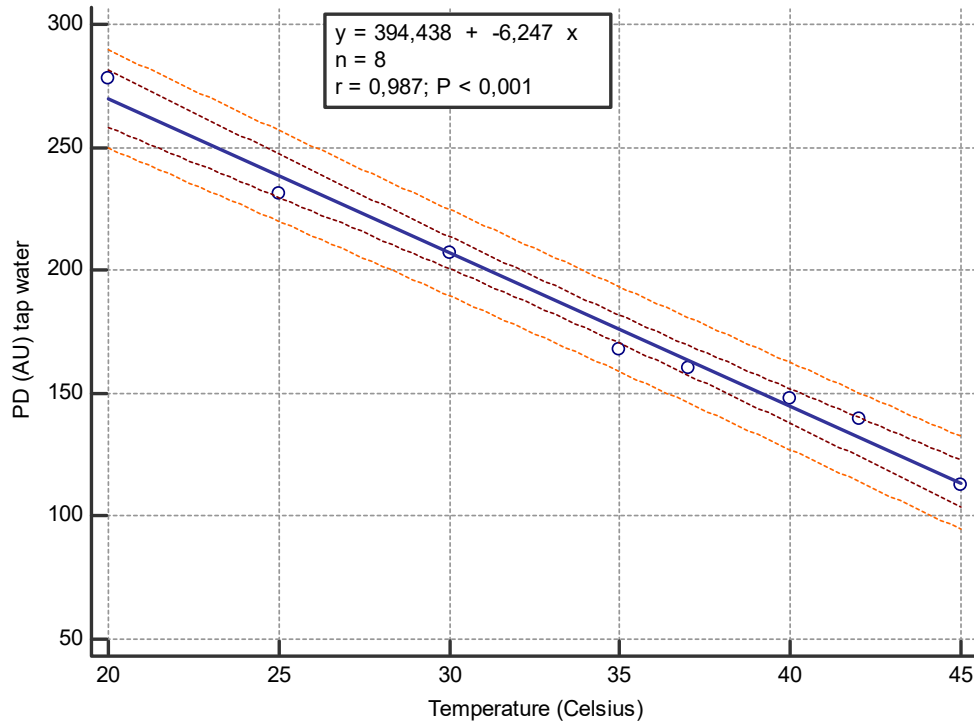


Figure 58: Linear regression for the relationship between tap water PD and temperature. The PD values were obtained with MESE sequence.

Table 11: Correlations of NaCl solutions and tap water samples PD with temperature, T.

<i>HASTE sequence</i>					
<i>Y axis</i>	<i>X axis</i>	<i>slope</i> $\left(\frac{AU}{^{\circ}C}\right)$	<i>Intercept</i> (AU/°C)	R^2	P
<i>PD(AU) of NaCl 0,2%</i>	<i>T(°C)</i>	$-19,6069 \pm 4,7113$	$2158,7497 \pm 165,8028$	0,7427	< 0,0001
<i>PD(AU) of NaCl 0,4%</i>	<i>T(°C)</i>	$-20,9161 \pm 4,1552$	$2063,6278 \pm 146,2326$	0,8085	< 0,0001
<i>PD(AU) of NaCl 0,6%</i>	<i>T(°C)</i>	$-19,0853 \pm 4,6421$	$2135,4962 \pm 163,3658$	0,7380	= 0,0063
<i>PD(AU) of NaCl 0,8%</i>	<i>T(°C)</i>	$-22,9032 \pm 4,3194$	$2216,6112 \pm 152,0101$	0,8241	= 0,0018
<i>PD(AU) of NaCl 0,9%</i>	<i>T(°C)</i>	$-24,3161 \pm 3,7816$	$2126,8137 \pm 133,0831$	0,8733	= 0,0007
<i>PD(AU) of NaCl 1%</i>	<i>T(°C)</i>	$-22,9768 \pm 4,2117$	$2177,0942 \pm 148,2555$	0,8322	= 0,0016
<i>PD(AU) of tap water%</i>	<i>T(°C)</i>	$-21,3536 \pm 2,6280$	$1678,3602 \pm 92,4847$	0,9167	= 0,0002

Table 12: Correlations of NaCl solutions and tap water samples PD with temperature, T.

<i>HASTE (32NEX) sequence</i>					
<i>Y axis</i>	<i>X axis</i>	<i>slope</i> $\left(\frac{AU}{^{\circ}C}\right)$	<i>Intercept</i> (AU/°C)	R^2	P
<i>PD(AU) of NaCl 0,2%</i>	<i>T(°C)</i>	$-12,9137 \pm 0,4729$	$1054,9203 \pm 16,5182$	0,9933	< 0,0001
<i>PD(AU) of NaCl 0,4%</i>	<i>T(°C)</i>	$-12,8577 \pm 0,4622$	$1007,2397 \pm 16,1414$	0,9936	< 0,0001
<i>PD(AU) of NaCl 0,6%</i>	<i>T(°C)</i>	$-12,7503 \pm 0,4439$	$1069,2032 \pm 12,7503$	0,9940	< 0,0001
<i>PD(AU) of NaCl 0,8%</i>	<i>T(°C)</i>	$-14,3480 \pm 0,5590$	$1113,5796 \pm 19,5240$	0,9925	< 0,0001
<i>PD(AU) of NaCl 0,9%</i>	<i>T(°C)</i>	$-14,7143 \pm 0,6411$	$1069,0400 \pm 22,3898$	0,9906	< 0,0001
<i>PD(AU) of NaCl 1%</i>	<i>T(°C)</i>	$-14,6057 \pm 0,6293$	$1102,1373 \pm 21,9794$	0,9908	< 0,0001
<i>PD(AU) of tap water%</i>	<i>T(°C)</i>	$-11,9650 \pm 0,6116$	$850,4297 \pm 21,3612$	0,9871	< 0,0001

Table 13: Correlations of NaCl solutions and tap water samples PD with temperature T.

<i>MESE sequence</i>					
<i>Y axis</i>	<i>X axis</i>	<i>slope</i> ($\frac{AU}{^{\circ}C}$)	<i>Intercept</i> (AU/°C)	R^2	P
<i>PD(AU) of NaCl 0,2%</i>	<i>T(°C)</i>	$-6,3114 \pm 0,3096$	$435,5284 \pm 10,8970$	0,9858	< 0,0001
<i>PD(AU) of NaCl 0,4%</i>	<i>T(°C)</i>	$-6,2080 \pm 0,31092$	$417,9606 \pm 10,9426$	0,9852	< 0,0001
<i>PD(AU) of NaCl 0,6%</i>	<i>T(°C)</i>	$-6,2564 \pm 0,3344$	$431,4083 \pm 11,7681$	0,9831	< 0,0001
<i>PD(AU) of NaCl 0,8%</i>	<i>T(°C)</i>	$-6,7619 \pm 0,3104$	$449,7339 \pm 10,9232$	0,9875	< 0,0001
<i>PD(AU) of NaCl 0,9%</i>	<i>T(°C)</i>	$-7,4338 \pm 0,2292$	$454,0439 \pm 8,0663$	0,9943	< 0,0001
<i>PD(AU) of NaCl 1%</i>	<i>T(°C)</i>	$-6,7663 \pm 0,3534$	$440,9844 \pm 12,4376$	0,9839	< 0,0001
<i>PD(AU) of tap water%</i>	<i>T(°C)</i>	$-6,2471 \pm 0,2095$	$394,4377 \pm 10,2231$	0,9872	< 0,0001

3.2 Electrical conductivity (EC) vs temperature measurements

The dependence of EC was investigated over a wide range of temperatures. Specifically, EC of the salt solutions and tap water samples was measured with respect to each degree of temperature. The maximum temperature was 45°C and the starting temperature was 20°C. The scheme of temperatures was 20°C, 22,5°C, 25°C, 27,5°C, 30°C, 35°C, 37,5°C, 40°C, 42,5°C, 45°C.

Data is presented separately for each kind of sample phantom. Specifically, EC values regarding different concentration of sodium chloride solution (% w/v) and tap water as a function of temperature are summarized in Table 15. The unit of EC in the following table is $\mu S/cm$. The accuracy of the EC meter is $\pm 1\%$ of reading.. Also, at a specific temperature the resultant EC value is the mean of multiple measurements.

Table 14: EC measurements of the salt solutions and of the tap water samples at various temperatures.

$T(^{\circ}C)$	$EC(0,2\%)$	$EC(0,4\%)$	$EC(0,6\%)$	$EC(0,8\%)$	$EC(0,9\%)$	$EC(1\%)$	<i>Tap water</i>
20	3462	3713	10155	13576	14903	16193	278
22,5	3774	7475	10627	-	15274	-	275
25	4044	7865	11530	14969	15794	18571	303
27,5	4227	8186	-	15195	16767	19546	306
30	4426	8599	12054	16680	17587	20646	339
35	4917	9640	13737	18295	18981	22628	362
37,5	5150	9970	14650	19119	19946	23585	377
40	5365	9698	15165	20033	20940	24730	392
42,5	5588	10778	16045	20950	21504	26440	415
45	5900	11560	16538	21940	22753	27155	441

From the previous table, the EC measurements follow normal distributions. This assumption was examined via Shapiro – Wilk test. Moreover, no outliers were found in our data.

According to the theoretical introduction, the temperature dependence of EC can be described by three different types of relationships : $y = a \cdot x + b$, $y = a \cdot x^2 + b \cdot x + c$ and $y = a \cdot e^{-b \cdot x}$. The final choice was based on the best fit of the data. So we compared the R^2 and the residual standard deviation for the fits and we concluded that the conductivity of the samples is approximately parabolic as a function of temperature between 20-45°C.

Table 16 presents the derived relationship between EC of the NaCl and tap water samples with temperature

As an example, the variation of 0,9 % (w/v %) NaCl solution with temperature is shown in figure 59.

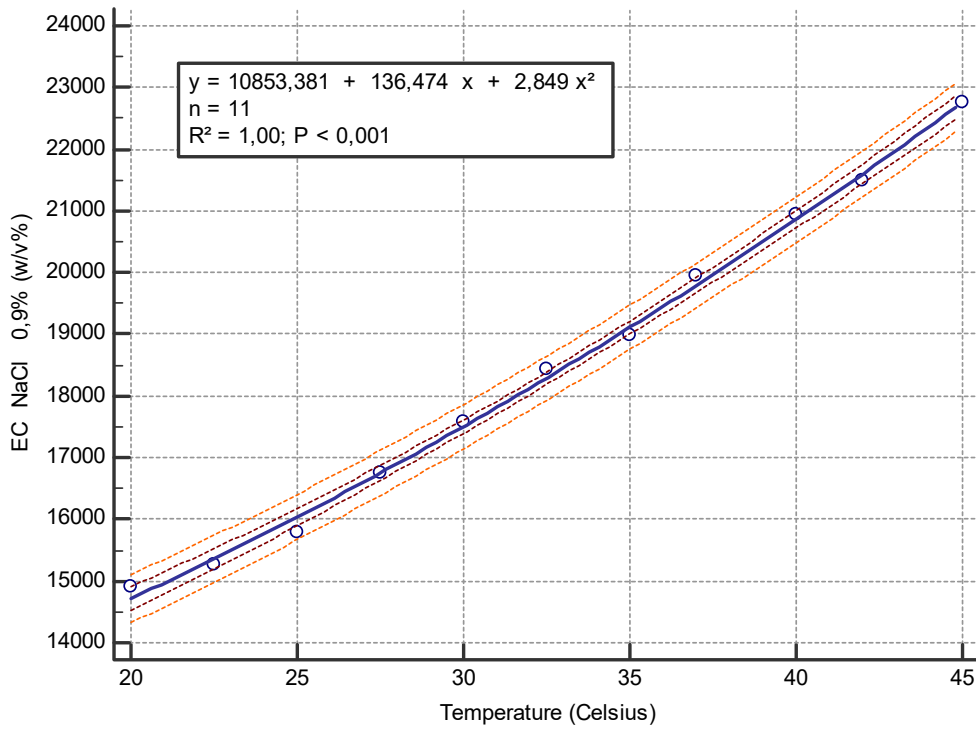


Figure 59 : Parabolic relationship between 0,9% NaCl solution EC and temperature.

Table 15 : Fit functions between 20 - 45°C for the NaCl solutions and tap water samples.

Y axis	X axis	$a\left(\frac{\mu S}{cm \cdot ^\circ C^2}\right)$	$b\left(\frac{\mu S}{^\circ C \cdot cm}\right)$	$c\left(\frac{\mu S}{cm}\right)$	R^2	P
$EC\left(\frac{\mu S}{cm}\right)$ of NaCl 0,2%	T(°C)	-0,08503	99,1491	1562,1510	0,9978	< 0,0001
$EC\left(\frac{\mu S}{cm}\right)$ of NaCl 0,4%	T(°C)	-8,0610	751,4364	-66621,3706	0,8692	= 0,0003
$EC\left(\frac{\mu S}{cm}\right)$ of NaCl 0,6%	T(°C)	-2,9977	66,8170	7653,7720	0,9907	< 0,0001
$EC\left(\frac{\mu S}{cm}\right)$ of NaCl 0,8%	T(°C)	+2,9437	148,9400	9333,0374	0,9954	< 0,0001
$EC\left(\frac{\mu S}{cm}\right)$ of NaCl 0,9%	T(°C)	+2,8490	136,4740	10853,3812	0,9973	< 0,0001
$EC\left(\frac{\mu S}{cm}\right)$ of NaCl 1%	T(°C)	+1,6858	325,6483	9174,9091	0,9962	< 0,0001
$EC\left(\frac{\mu S}{cm}\right)$ of tap water%	T(°C)	0,007119	2,0089	204,2126	0,9889	< 0,0001

3.3 Correlation between T2 relaxation time and EC measurements.

A possible relation between T2 and EC was investigated. However, as analyzed previously EC and T2 are highly correlated with temperature. So in order to examine the relationship between T2 and EC, we must eliminate the dependence on temperature. For this reason, we constructed the following tables. Each table corresponds to a specific MRI pulse sequence which was utilized to measure T2 relaxation time. The variation of T2 with EC is presented. The units of EC and T2 are $\mu S/cm$ and *msec* respectively.

Tables 16 & 17: Electrical conductivity measurements and T2 values calculated from HASTE pulse sequence at a specific temperature.

<i>HASTE sequence</i>								
	T2 (20°C)	EC (20°C)	T2 (25°C)	EC (25°C)	T2 (30°C)	EC (30°C)	T2 (35°C)	EC (35°C)
<i>NaCl</i> 0,2%	2045	3462	2156	4044	2237	4426	2443	4917
<i>NaCl</i> 0,4%	2056	3713	2218	7865	2375	8599	2555	9640
<i>NaCl</i> 0,6%	2140	10155	2287	11530	2414	12054	2633	13737
<i>NaCl</i> 0,8%	2197	13576	2364	14969	2506	16680	2724	18295
<i>NaCl</i> 0,9%	2198	14903	2368	15794	2494	17587	2719	18981
<i>NaCl</i> 1%	2173	16193	2338	18571	2470	20646	2705	22628

<i>HASTE sequence</i>								
	T2 (37°C)	EC (37°C)	T2 (40°C)	EC (40°C)	T2 (42°C)	EC (42°C)	T2 (45°C)	EC (45°C)
<i>NaCl</i> 0,2%	2499	5150	2559	5365	2574	5588	2676	5900
<i>NaCl</i> 0,4%	2621	9970	2795	9698	2755	10778	2824	11560
<i>NaCl</i> 0,6%	2702	14650	2793	15165	2786	16045	2865	16538
<i>NaCl</i> 0,8%	2754	19119	2847	20033	2865	20950	2963	21940
<i>NaCl</i> 0,9%	2776	19946	2895	20940	2870	21504	2999	22753
<i>NaCl</i> 1%	2775	23585	2836	24730	2831	26440	2895	27155

At constant temperature, the measured T2 values were plotted against electrical conductivity. A second degree polynomial was fitted to the measured points ($Y = a \cdot x^2 + b \cdot x + c$). Results are shown in the following table. The units of EC and T2 are $\mu S/cm$ and $msec$ respectively.

The variation of T2 with EC when temperature is constant and equal to 37°C is presented in the next figure.

Table 18 : Fit functions between for the NaCl solutions and tap water samples.

Y axis	X axis	$a(\frac{msec \cdot cm^2}{\mu S^2})$	$b(\frac{msec \cdot cm}{\mu S})$	$c(msec)$	R^2	P
T2(20°C)	EC(20°C)	$-8423 \cdot 10^{-10}$	0,002770	1960,5879	0,9644	= 0,0067
T2(25°C)	EC(25°C)	$-8950 \cdot 10^{-10}$	0,03502	2017,2764	0,9406	= 0,0145
T2(30°C)	EC(30°C)	$-1346 \cdot 10^{-10}$	0,04883	2046,1205	0,9756	= 0,0038
T2(35°C)	EC(35°C)	$-9081 \cdot 10^{-10}$	0,04109	2254,9316	0,9803	= 0,0028
T2(37°C)	EC(37°C)	$-7453 \cdot 10^{-10}$	0,03666	2329,5631	0,9966	= 0,0002
T2(40°C)	EC(40°C)	$-1375 \cdot 10^{-10}$	0,05417	2334,4770	0,8802	= 0,0415
T2(42°C)	EC(42°C)	$-1037 \cdot 10^{-10}$	0,04543	2359,5598	0,9630	= 0,0071
T2(45°C)	EC(45°C)	$-1011 \cdot 10^{-10}$	0,0457	2433,7639	0,9070	=0,02823

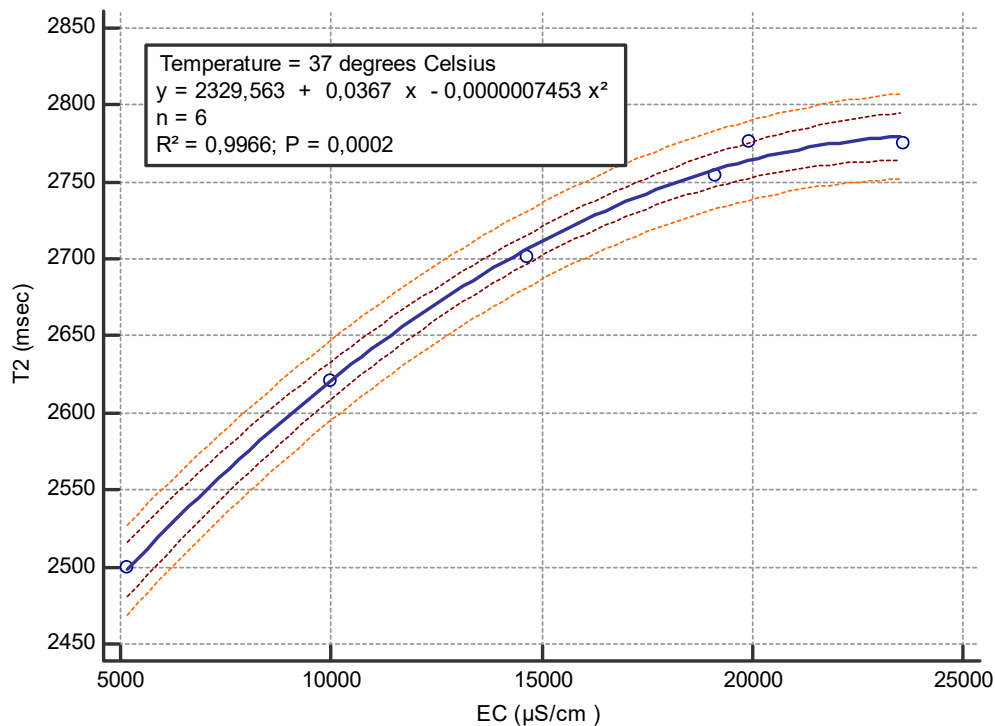


Figure 60 : Variation of T2 with EC when temperature is set to 37 degrees Celsius. The T2 values were obtained with HASTE sequence.

Tables 19 & 20 : Electrical conductivity measurements and T2 values calculated from HASTE (32 NEX) pulse sequence at a specific temperature.

<i>HASTE (32 NEX)sequence</i>								
	T2 (20°C)	EC (20°C)	T2 (25°C)	EC (25°C)	T2 (30°C)	EC (30°C)	T2 (35°C)	EC (35°C)
<i>NaCl</i> 0,2%		3462	2177	4044	2237	4426	2508	4917
<i>NaCl</i> 0,4%	2047	3713	2225	7865	2402	8599	2644	9640
<i>NaCl</i> 0,6%	2109	10155	2292	11530	2466	12054	2684	13737
<i>NaCl</i> 0,8%	2175	13576	2362	14969	2539	16680	2764	18295
<i>NaCl</i> 0,9%	2160	14903	2351	15794	2517	17587	2764	18981
<i>NaCl</i> 1%	2173	16193	2350	18571	2514	20646	2727	22628

<i>HASTE (32 NEX)sequence</i>								
	T2 (37°C)	EC (37°C)	T2 (40°C)	EC (40°C)	T2 (42°C)	EC (42°C)	T2 (45°C)	EC (45°C)
<i>NaCl</i> 0,2%	2528	3462	2657	4044	2704	4426	2782	4917
<i>NaCl</i> 0,4%	2654	3713	2816	2900	2402	8599	2981	9640
<i>NaCl</i> 0,6%	2732	10155	2837	11530	2888	12054	3015	13737
<i>NaCl</i> 0,8%	2787	13576	2923	14969	2978	16680	3130	18295
<i>NaCl</i> 0,9%	2813	14903	2950	15794	3011	17587	3120	18981
<i>NaCl</i> 1%	2809	16193	2882	18571	2948	20646	3013	22628

At constant temperature, the measured T2 values were plotted against electrical conductivity. A second degree polynomial was fitted to the measured points ($Y = a \cdot x^2 + b \cdot x + c$). Results are shown in the following table. The units of EC and T2 are $\mu S/cm$ and $msec$ respectively.

The variation of T2 with EC when temperature is constant and equal to 37°C is presented in the next figure.

Table 21: Fit functions between for the NaCl solutions and tap water samples.

Y axis	X axis	$a(\frac{msec \cdot cm^2}{\mu S^2})$	$b(\frac{msec \cdot cm}{\mu S})$	$c(msec)$	R^2	P
T2(20°C)	EC(20°C)	$-2584 \cdot 10^{-10}$	0,01488	1998,3981	0,9509	= 0,0109
T2(25°C)	EC(25°C)	$-5795 \cdot 10^{-10}$	0,02663	2069,2951	0,9570	= 0,0089
T2(30°C)	EC(30°C)	$-8923 \cdot 10^{-10}$	0,03514	2178,0458	0,9748	= 0,0040
T2(35°C)	EC(35°C)	$-1126 \cdot 10^{-10}$	0,04422	2315,6850	0,9712	= 0,0049
T2(37°C)	EC(37°C)	$-7558 \cdot 10^{-10}$	0,03725	2355,6878	0,9948	= 0,0004
T2(40°C)	EC(40°C)	$-1081 \cdot 10^{-10}$	0,04455	2456,7247	0,9169	= 0,0240
T2(42°C)	EC(42°C)	$-1005 \cdot 10^{-9}$	0,04368	2503,2243	0,8913	= 0,0358
T2(45°C)	EC(45°C)	$-1419 \cdot 10^{-9}$	0,05925	2476,6743	0,9260	= 0,0201

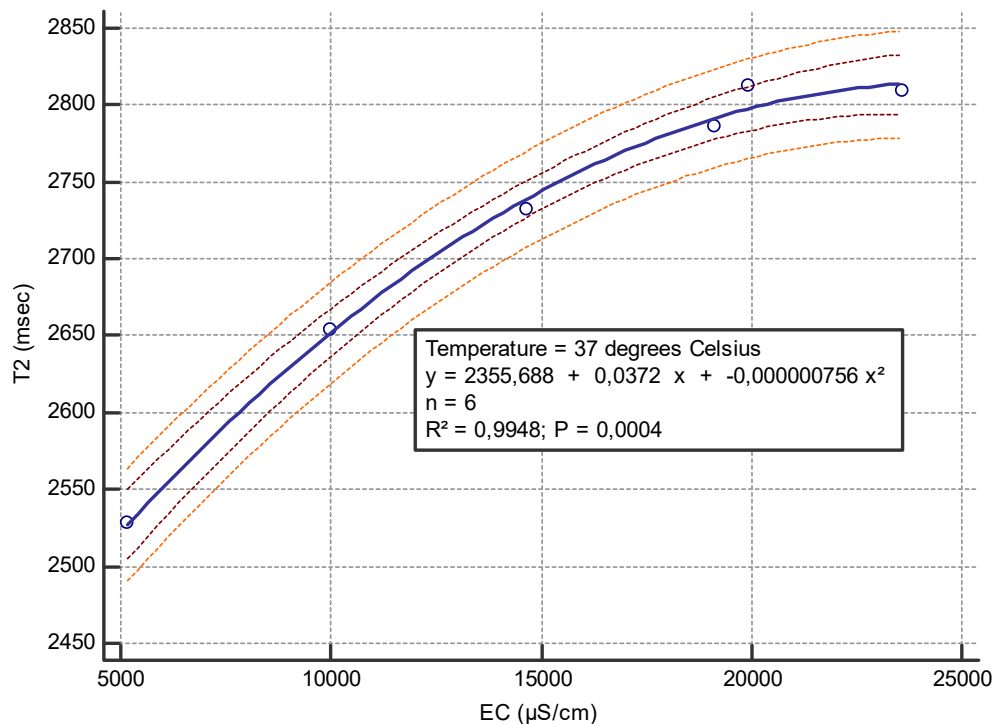


Figure 61 : Variation of T2 with EC when temperature is set to 37 degrees Celsius. The T2 values were obtained with HASTE (32NEX) sequence.

Tables 22 & 23 : Electrical conductivity measurements and T2 values calculated from MESE pulse sequence at a specific temperature.

<i>MESE sequence</i>								
	T2 (20°C)	EC (20°C)	T2 (25°C)	EC (25°C)	T2 (30°C)	EC (30°C)	T2 (35°C)	EC (35°C)
<i>NaCl</i> 0,2%	1976	3462	2111	4044	2224	4426	2477	4917
<i>NaCl</i> 0,4%	1958	3713	2170	7865	2288	8599	2554	9640
<i>NaCl</i> 0,6%	2050	10155	2312	11530	2493	12054	2692	13737
<i>NaCl</i> 0,8%	2106	13576	2342	14969	2506	16680	2852	18295
<i>NaCl</i> 0,9%	2050	14903	2327	15794	2490	17587	2672	18981
<i>NaCl</i> 1%	2089	16193	2336	18571	2516	20646	2771	22628

<i>MESE sequence</i>								
	T2 (37°C)	EC (37°C)	T2 (40°C)	EC (40°C)	T2 (42°C)	EC (42°C)	T2 (45°C)	EC (45°C)
<i>NaCl</i> 0,2%	2509	3462	2664	4044	2648	4426	2676	4917
<i>NaCl</i> 0,4%	2632	3713	2762	2900	2803	8599	2764	9640
<i>NaCl</i> 0,6%	2843	10155	2879	11530	2944	12054	2704	13737
<i>NaCl</i> 0,8%	2834	13576	2812	14969	2804	16680	2677	18295
<i>NaCl</i> 0,9%	2677	14903	2623	15794	2498	17587	2354	18981
<i>NaCl</i> 1%	2773	16193	2788	18571	2764	20646	2758	22628

At constant temperature, the measured T2 values were plotted against electrical conductivity. A second degree polynomial was fitted to the measured points ($Y = a \cdot x^2 + b \cdot x + c$). Results are shown in the following table. The units of EC and T2 are $\mu S/cm$ and $msec$ respectively.

The variation of T2 with EC when temperature is constant and equal to 37°C is presented in the next figure.

Table 24: Fit functions between for the NaCl solutions and tap water samples.

Y axis	X axis	$a(\frac{msec \cdot cm^2}{\mu S^2})$	$b(\frac{msec \cdot cm}{\mu S})$	c(msec)	R^2	P
T2(20°C)	EC(20°C)	$-7790 \cdot 10^{-10}$	0,02445	1888,9500	0,8812	= 0,0409
T2(25°C)	EC(25°C)	$-1203 \cdot 10^{-9}$	0,04418	1936,9055	0,9441	= 0,0132
T2(30°C)	EC(30°C)	$-1319 \cdot 10^{-9}$	0,05211	2000,0111	0,9054	= 0,0291
T2(35°C)	EC(35°C)	$-8296 \cdot 10^{-10}$	0,04081	2278,8976	0,7911	= 0,0955
T2(37°C)	EC(37°C)	$-1708 \cdot 10^{-9}$	0,06222	2225,2794	0,7382	= 0,1340
T2(40°C)	EC(40°C)	$-1070 \cdot 10^{-9}$	0,03442	2526,0525	0,2286	= 0,6775
T2(42°C)	EC(42°C)	$-1144 \cdot 10^{-9}$	0,03556	2523,6698	0,01225	= 0,8221
T2(45°C)	EC(45°C)	$-4478 \cdot 10^{-10}$	-0,01929	2833,2497	0,07632	= 0,8877

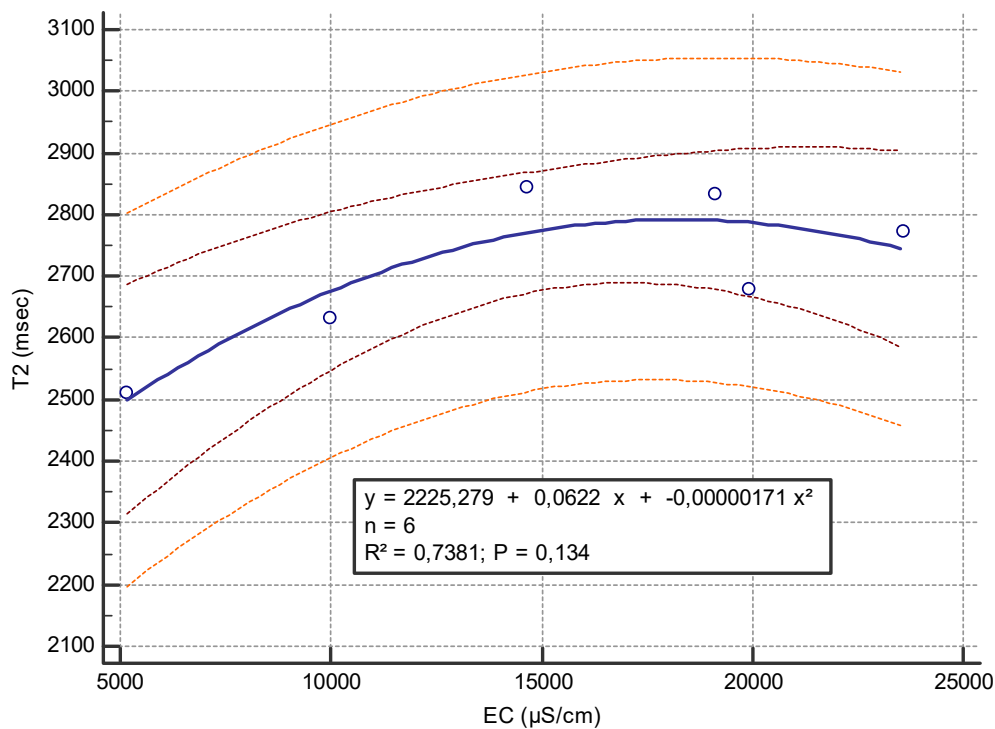


Figure 62 : Variation of T2 with EC when temperature is set to 37 degrees Celsius. The T2 values were obtained with MESE sequence.

4. DISCUSSION/CONCLUSIONS

4.1 Evaluating the goodness of fit

4.1.1 Variation of T2 with temperature

We tried to predict the variation of T2 with temperature with three different MRI imaging techniques: 1) HASTE 2) HASTE (32NEX) 3) MESE. .Next, we performed linear regression analysis to describe quantitatively the relationship between those two variables. In this chapter, for each separate MRI sequence, we evaluate the goodness of the fit of the linear regression model. For each case, the effectiveness of the linear model is evaluated based on various metrics. In our study we used the Coefficient of Determination, R^2 and the residual standard deviation (or standard error of the estimate), S_{res}, S_E . Moreover, the graphical representation of the 95 % confidence interval for the regression line is used as a visual quality measure of the linear fit. The goodness of fit indicates which MRI pulse sequence can be used to calculate more accurately T2 relaxation time and quantify better its correlation with temperature. For this purpose, the next table is presented which includes the R^2 S_{res} and the significance level sit the F- test (P value)of linear regression lines of T2(ms) vs temperature, T(°C). From tables 5,6 and 7, we will evaluate only one linear regression model. In other words, the EC parameter becomes constant and the evaluation concerns only the relationship between T2 and temperature. Thus, for each separate imaging technique we will measure the quality of linear regression between 0,2% and 0.9% (w/v%) NaCl solution on T2 with temperature. Though not presented here, similar results can be obtained for each and very aqueous solution used in our study.

Tables 24 &25: Quality metrics for regression between T2 and temperature.

Linear regression: T2(ms) – T(°C), EC: 0,2% ($\frac{w}{v}$%)			
–	R^2	$S_E(msec)$	P value
HASTE	0.9853	29.4701	< 0.0001
HASTE (32NEX)	0.9963	17.0797	< 0.0001
MESE	0.9701	50.8418	< 0.0001

Linear regression: T2(ms) – T(°C), EC: 0,9% ($\frac{w}{v}$%)			
–	R^2	$S_E(msec)$	P value
HASTE	0.9878	33.6940	< 0.0001
HASTE (32NEX)	0.9878	17.0297	< 0.0001
MESE	0.3640	183.8099	= 0.1133

Comparing the confidence interval for the regression line in figures 45-50 (dashed brown curves next to the regression line) we can see that : The width of the

confidence interval is small when T2 values are obtained with HASTE (32NEX) technique (figures 47-48). In contrast, the interval is wider when T2 values are acquired with the MESE technique (figures 49-50). The HASTE technique covers the intermediate region between HASTE(32NEX) and MESE techniques.

From tables 24 & 25, we can see that the regression line of T2 vs temperature using the HASTE(32NEX) pulse sequence has the highest coefficient of determination and the smallest residual standard deviation. Also from table 6, the significance level for the F-test (P -value) is always much less than 0.05. On the contrast, when MESE sequence is utilized, the corresponding regression line of T2 and temperature has the lowest coefficient of determination and the value of residual standard deviation is unacceptably large. Moreover, P value is not always less than 0,05 (Table 25). So, this sequence results in statistically non significant relation between T2 and temperature. However, these two variables are strongly correlated, as we discussed in the introduction. Again, the results obtained with the HASTE sequence cover the intermediate region between HASTE (32NEX) and MESE techniques.

Considering all the above, HASTE with multiple signal averaging calculates better and more accurately T2 relaxation time of sodium chloride solution compared to HASTE and MESE sequence. In addition this T2 mapping technique is found to be the best approach to accurate modeling the relationship between T2 and temperature.

The only difference between HASTE and HASTE (32NEX) sequence is the acquisition time and the number of signal averages. In particular, the total scan time of the HASTE sequence was 1 second whereas the acquisition time of HASTE (32 NEX) was approximately 10 seconds. However, due to signal averaging, the HASTE (32NEX) technique quantifies the actual T2 values more accurate than those values obtained from the HASTE pulse sequence. In MESE sequence, the quality of fit between T2 and temperature is inadequate compared to HASTE and HASTE (32 NEX) techniques. Moreover this method has the longest scan time (4 minutes and 20 seconds). Therefore, the best MRI sequence/technique for establishing the linear relationship between T2 relaxation time and temperature is HASTE (32NEX).

4.1.2 Variation of Proton Density (PD) with temperature

Similarly, the following tables are presented below:

In the following tables S_E is measured in Arbitrary Units (AU); the same units on which PD variable is measured.

Tables 26&27: Quality metrics for regression between PD and temperature.

<i>Linear regression: PD(AU) – T(°C), EC: 0, 9% ($\frac{w}{v}$%)</i>			
–	R^2	$S_E(AU)$	<i>P value</i>
HASTE	0.8733	86,5233	= 0.0007
HASTE (32NEX)	0.9906	14,5459	< 0.0001
MESE	0.9943	5.2442	< 0.0001

Linear regression: PD(AU) – T(°C), tap water			
–	R²	S_E(AU)	P value
HASTE	0.9167	60.1285	= 0.0007
HASTE (32NEX)	0.9871	13.9876	< 0.0001
MESE	0.9872	6.6465	< 0.0001

Comparing the confidence interval for the regression line in figures 53-58 (dashed brown curves next to the regression lines) we can see that : The width of the confidence interval is small when PD values are acquired using the MESE and HASTE (32NEX) techniques (figures 55-58). In contrast, the interval is wider when PD values are acquired with the HASTE technique (figures 53-54). Also from table 6, P value for each and every utilized pulse sequence is always much less than 0.05. This implies that the relationship between PD and temperature is statistically significant

From tables 26 & 27, we can see that the regression line of PD and temperature using the HASTE pulse sequence has the lowest coefficient of determination and the highest residual standard deviation. On the contrast, when MESE sequence is utilized, the corresponding coefficient of determination for the regression line of PD and temperature increases substantially and the value of residual standard deviation gets shortened significantly (tables 26 and 27). It is worth mentioning that when this technique is utilized to quantify the PD, the residual standard deviation is the smallest compared to HASTE and HASTE (32NEX) methods. However, as we can see in tables 11-13 the value of R² is maximized (close to 1) when PD values are recovered from HASTE (32NEX) T2 decay curves.

It is noteworthy that the values of PD when the MESE sequence is utilized are significantly lower than the corresponding values acquired with the HASTE technique. A major difference between these two methods is that a driven equilibrium pulse is used in conjunction with the HASTE sequence. Consequently, the longitudinal magnetization is fully recovered by the end of each effective TR interval. In contrast, when MESE sequence is utilized, the magnetization is not fully recovered within a given TR period (aqueous solutions have long T1 values, i.e. several seconds). In other terms, when the magnetization is rotated into the transverse plane, its magnitude is affected indirectly by the T1 relaxation time. Under this rationale, HASTE (32NEX) was found to be the appropriate sequence for quantifying the relationship between PD and temperature.

[4.1.3 Variation of T2 with Electrical Conductivity \(EC\)](#)

In our study, HASTE, HASTE with multiple signal averaging and MESE sequences were used for T2 mapping. The final aim of our study was to derive a possible relationship between the data obtained from these sequences and the electrical conductivity (EC) of aqueous solutions samples. Hence, a collection of six 100 ml samples were prepared with NaCl concentration that ranged from 0,2% (w/v%) up to 1 (w/v%) at intervals of approximately 0,2%.

However, both of T2 relaxation time and EC depend on temperature. Thus, if we want to derive a relationship between them, temperature must be kept constant. Based on various quality metrics, a parabolic equation was found to describe the relationship between T2 and EC. Thus, for each separate imaging technique we will estimate the quality of nonlinear regression between T2 relaxation time and EC when temperature, T , is at 37°C. Though not presented here, similar results can be obtained for each and every temperature used in this study.

Table 28: Quality metrics for nonlinear regression between T2 and EC

<i>NonLinear regression: T2(msec) – EC ($\frac{\mu S}{cm}$), T = 37°C</i>			
–	R^2	$S_E(AU)$	<i>P value</i>
HASTE	0.9966	8.2710	= 0.0002
HASTE (32NEX)	0.9948	10.4087	= 0.0004
MESE	0.7382	85.7894	= 0.1340

From tables 18 (HASTE sequence) and 21 (HASTE sequence with 32 NEX) we can see that the values of R^2 range between 0,88 and 0,99. As it can be seen from the table 28, the value of R^2 is maximized when $T = 37^\circ\text{C}$. In contrast, the coefficient of determination is significant lower when T2 values are obtained from the MESE sequence (Table 24).

The residual standard deviation is minimized when T2 values are obtained with HASTE technique, whereas its value is maximized when the MESE sequence is used (Table 28). The HASTE(32NEX) technique covers the intermediate region between HASTE and MESE methods.

Comparing the confidence interval for the regression line in figures 60-62, it can be concluded that : The width of the confidence interval is small when T2 values are obtained from HASTE (32NEX) and HASTE acquisition techniques. Conversely, the interval is wider when T2 values are acquired with MESE technique (figures 62).

Consequently, MESE is not the appropriate method to quantify the relationship between T2 and EC. In contrast, HASTE was found to be the best method for describing the relation between these two parameters.

4.2 Discussion

4.2.1 Hyperthermia treatment

Hyperthermia is a promising way to improve cancer treatment, especially when this method is applied in combination with surgery, chemotherapy, radiotherapy and immunotherapy. This treatment can be classified into 3 categories. : Local, regional and wholebody hyperthermia.⁵² Local hyperthermia via various mechanisms

activates antitumor immune responses: Overexpression of MICA and CD8⁺ T cells on the surface of tumour cells, heated tumour cells release heat shock proteins and exosomes, vasculature permeability within the tumour increases. Due to these anti-tumour immune responses the growth of tumour is slowed down.⁵³ Moreover, local hyperthermia proved to be a useful means for the treatment of head and neck cancer.⁵⁴ In addition, survival rates are increased when hyperthermia is combined with radiotherapy treatment.⁵³ There are novel therapeutic approaches that are guided or triggered by temperature manipulations such as heat-induced gene therapy or targeting methods like heat-sensitive liposomes.⁵⁵

4.2.2 Hyperthermia treatment and MRI.

Accurate measurement and real time monitoring of the applied temperature throughout the heated region affect the therapeutic outcome of this treatment.⁵⁶ More specifically, a non invasive three dimensioning method that enables the characterization of heating pattern during the hyperthermic treatment is required in order to improve quality control and real-time temperature monitoring. Quantitative MRI (qMRI) based on sensitive MR parameters provides such a method. Therefore, MRI could become a useful means for non-invasive thermometry monitoring procedures.

The ability of MRI to construct in vivo quantitative temperature maps makes it a well suited means for guiding and monitoring thermal therapy. However, these maps are limited to the measurement of relative temperature changes and they cannot be used to estimate absolute temperature values. However, thermosensitive nanoparticles (paramagnetic thermosensitive liposomes) have been reported as innovative contrast agents offering the potential to overcome these limitations.⁵⁷

Various temperature sensitive MR parameters have been proposed and investigated for MR based thermometry. These include changes in the proton resonance frequency (PRF), diffusion coefficients or T1 and T2 relaxation times. The PRF shift method is the most commonly preferred choice for imaging thermometry. Despite the advantages of this method (linearity of PRF over a large temperature range, independence of tissue types), the disadvantages include its ability to measure only relative temperature changes and it cannot be applied to measure temperature in adipose tissues.^{13,58} In contrast, T1 relaxation time –based MR thermometry is applicable in fatty tissues. However, T1 relaxation time is sensitive to tissue composition changes, whereas PRF is not.^{13,58} Many in vivo studies have shown the linear dependence of T1 relaxation time on temperature. Another disadvantage of T1 based- thermometry compared to PRF thermometry is that it requires longer acquisition times. This drawback limits its usefulness in real-time applications.^{13,58}

T2-based thermometry has been proposed as an alternative method for the measurement of temperatures. A main drawback of this method is its non-linear behavior on high temperature scales. In addition this technique requires longer acquisition time compared to PRF method. In order to quantify this parameter, multi echo spin echo (MESE) type pulse sequences are utilized.^{13,58} These disadvantages led to the tendency to discard T2-based thermometry for MR guidance of noninvasive thermal therapies in clinical applications. To the best of our knowledge,

utilization of fast imaging methods to address this problem have not been reported in the literature.

This work has revealed that HASTE or HASTE with multiple signal averages has been proved to be an appropriate pulse sequence to measure the signal decay and quantify T2 relaxation time or proton density (PD) within 1 second. Moreover, this technique can be used to sufficiently describe the variation of T2 or PD with temperature. Our work clearly has some limitations. The first is that the experiment was performed only 3 times in the past. The second is that the correlation of T2/PD with temperature is investigated only at absolute temperatures of 20-45°C. Finally, the electrical conductivity (EC) -dependence of T2 relaxation time is examined within a specified range of values of EC. Further work needs to be done to establish which MR parameter (T1, T2 and PD) is more sensitive to temperature changes. Further experimental investigations are needed to quantify the relationship between T2/PD and temperature in vivo and ex vivo (freshly excised biological tissue). At the same time, we have confirmed that T2 relaxation time and EC are strongly correlated. Further studies will need to be performed to investigate in detail this relationship.

References

1. Tofts P. Quantitative MRI of the Brain. Tofts P, editor. Chichester: John Wiley & Sons; 2003. 144–162 p.
2. McRobbie DW, Moore EA, Graves MJ. MRI from picture to proton. 2nd ed. MRI from Picture to Proton. New York: Cambridge University Press; 2006. 137–166 & 220–257 p.
3. Dale, Brian M., Brown, Mark A, Semelka RC. MRI: Basic principles and applications. 5th ed. Vol. 369, Journal of Petrology. Hoboken,NJ: Wiley-Blackwell;
4. Maris TG. Ανάπτυξη λογισμικού για την δημιουργία υπολογισμένων ποσοτικών εικόνων (M.R.I) T2-QMRI και η χρήση τους στον χαρακτηρισμό των ιστών. Εφαρμογή - Έρευνα στην μεσογειακή αναιμία (dissertation). National and Kapodistrian University of Athens; 1997.
5. Graaf RA de. In Vivo NMR Spectroscopy: Principles and Techniques. 3rd ed. Hoboken,NJ: John Wiley & Sons; 2019. 129–133 p.
6. Bloembergen N, Purcell EM, Pound R V. Relaxation effects in nuclear magnetic resonance absorption. Phys Rev. 1948;73(7):679–712.
7. Um V, 99 E, Er NB, Soromont L. P H YSI CAL REVIEW Relaxation Processes in a System of Two Spins*. Phys Rev [Internet]. 1955;953(8):559–65. Available from: <https://journals.aps.org/pr/pdf/10.1103/PhysRev.99.559>
8. Stroman P. Functional MRI Study Design. Essentials of Functional MRI. Boca Raton: CRC Press; 2011. 46–51 p.
9. Vlaardingerbroek, Marinus T., Boer JA. Magnetic resonance imaging. 3rd ed. Vol. 36, Biomedical Instrumentation and Technology. Heidelberg: Springer-Verlag GmbH;
10. Hendrick RE. Breast MRI: Fundamentals and Technical Aspects. Vol. 53, Journal of Chemical Information and Modeling. New York: Springer Science+Business Media; 21–25 p.
11. James TL, Thomas L. NUCLEAR MAGNETIC RESONANCE IN BIOCHEMISTRY: Principles and Applications. London: Academic Press; 1975. 40–45 p.
12. Hore P. Nuclear Magnetic Resonance. 2nd ed. Oxford: Oxford University Press; 2015. 65–66 p.
13. Shrivasta D. Theory and Applications of Heat Transfer in Humans. Shrivasta D, editor. Vol. 26. Hoboken,NJ: Wiley; 2018. 275–284 p.
14. Elster A. Spin echo v FSE - Questions and Answers in MRI [Internet]. 2019 [cited 2020 Oct 18]. Available from: <http://mriquestions.com/se-vs-multi-se-vs-fse.html>
15. Lipton ML. Totally Accessible MRI User's Guide to Principles. New York: Springer Science+Business Media; 2008. 38–45 & 113–127 p.
16. Semelka RC, Kelekis NL, Thomasson D, Brown MA, Laub GA. HASTE MR imaging: Description of technique and preliminary results in the abdomen. J Magn Reson Imaging. 1996;6(4):698–9.
17. MRI-questions.com. HASTE/SS-FSE - Questions and Answers in MRI [Internet]. [cited 2020 Oct 18]. Available from: <http://mriquestions.com/hastess-fse.html>
18. Elster A. Image contrast - Questions and Answers in MRI [Internet]. 2015 [cited 2020 Oct 18]. Available from: <http://mriquestions.com/image-contrast->

- trte.html
19. Xiong G. Influence of temperature on supercapacitor components. Vol. 25, SpringerBriefs in Applied Sciences and Technology. New York: Springer; 2015. 16 & 27–31 p.
 20. Zhang W, Chen X, Wang Y, Wu L, Hu Y. Experimental and Modeling of Conductivity for Electrolyte Solution Systems. ACS Omega. 2020;
 21. Petrowsky M, Frech R. Application of the compensated arrhenius formalism to self-diffusion: Implications for ionic conductivity and dielectric relaxation. J Phys Chem B. 2010;114(26):8600–5.
 22. Atkins, Peter, de Paula J. Physical Chemistry. 8th ed. Vol. 272, Journal of the Franklin Institute. Great Britain: Oxford University Press; 1961. 1019 p.
 23. Posts R. Temperature Compensation Algorithms for Conductivity. 2012 [cited 2020 Oct 19];2012–3. Available from: <https://www.aqion.de/site/112#fnref:1>
 24. Atc D, Rb- T, Likewise a, Figure B. CONDUCTIVITY METER 4520 Application note : A02-001A The effect of temperature on conductivity measurement. Bibby. 2009;44(0):1–3.
 25. Carlson G. Specific Conductance as an output unit for conductivity readings. Situ Tech Note. 2017;1–2.
 26. Barron JJ, Ashton C. The effect of temperature on conductivity measurement: a Reagecon technical paper. Reagecon [Internet]. 2007;(3):1–5. Available from: www.reagecon.com
 27. SAS. Conductivity-theory and practice. Anal Radiom [Internet]. 2004;D61M002:1–50. Available from: <http://scholar.google.com/scholar?hl=en&btnG=Search&q=intitle:Conductivity+Theory+and+Practice#4%5Cnhttp://scholar.google.com/scholar?hl=en&btnG=Search&q=intitle:Conductivity-theory+and+practice#0>
 28. Mäntynen M. Temperature correction coefficients of electrical conductivity and of density measurements for saline groundwater. Work Rep 2001–15 Posiva, Finl. 2001;(June):1–40.
 29. Leal A, Tarsikka PS. The Effect on Solubility and pH of Sodium Chloride Solution by Magnetic Field. Int J Environ Agric Biotechnol. 2017;2(5):2509–15.
 30. Peters RD, Henkelman RM. Proton-resonance frequency shift MR thermometry is affected by changes in the electrical conductivity of tissue. Magn Reson Med. 2000;43(1):62–71.
 31. Bottomley PA, Andrew ER. RF magnetic field penetration, phase shift and power dissipation in biological tissue: Implications for NMR imaging. Phys Med Biol. 1978;23(4):630–43.
 32. HI-2030 edge® Hybrid Multiparameter EC Meter [Internet]. [cited 2020 Oct 19]. Available from: <https://www.hannainst.dk/edge-bench-conductivity-meter.html>
 33. HI-763100 Edge Digital EC Platinum 4 Ring Electrode [Internet]. [cited 2020 Oct 19]. Available from: <https://www.hannainst.dk/hi-763100-edge-digital-ec-platinum-4-ring-electrode.html>
 34. Thermo Electron Corporation. Orion Conductivity Theory. 2012;6015:108–9. Available from: http://www.thermo.com/eThermo/CMA/PDFs/Articles/articlesFile_11377.pdf
 35. America S. Instruction Manual Instruction Manual. Int Bus. 2003;1–183.

36. Siemens MAGNETOM Sonata MRI - Manufacturer specifications [Internet]. [cited 2020 Oct 19]. Available from: <http://www.medwow.com/med/mri/siemens/magnetom-sonata/9776.model-spec>
37. Artisan. Find the Lumasense Technologies / Luxtron FOT at our website: Click HERE. 2003 [cited 2020 Oct 19];(217):352. Available from: www.artisanng.com
38. Industry Standard for Fiber Optic Thermometry [Internet]. [cited 2020 Oct 19]. Available from: www.luxtron.com
39. Luxtron Product Flour Optic Technology FOT.
40. Karvonen N. Operating instructions. *J Wildl Rehabil.* 2002;25(3):27.
41. Comet Tauchpumpe VIP, 12V, 16l/min von Comet Wasser & Sanitär bei Camping Wagner Campingzubehör [Internet]. [cited 2020 Oct 19]. Available from: https://www.campingwagner.de/product_info.php/info/p48369_Comet-Tauchpumpe-VIP--12V--16l-min.html
42. 12 & 24 Volt DC Submersible High Performance Pumps | Comet Pumps [Internet]. [cited 2020 Oct 19]. Available from: <https://www.cometpumps.biz/12-volt-submersible-high-performanc>
43. Bevington, Philip, Robinson DK. *Statistics book.pdf*. 3rd ed. New York: McGraw-Hill Education;
44. Saculinggan M, Balase EA. Empirical power comparison of goodness of fit tests for normality in the presence of outliers. *J Phys Conf Ser.* 2013;435(1).
45. Ghasemi A, Zahediasl S. Normality tests for statistical analysis: A guide for non-statisticians. *Int J Endocrinol Metab.* 2012;10(2):486–9.
46. Ahad NA, Yin TS, Othman AR, Yaacob CR. Sensitivity of normality tests to non-normal data. *Sains Malaysiana.* 2011;40(6):637–41.
47. Uttley J. Power Analysis, Sample Size, and Assessment of Statistical Assumptions—Improving the Evidential Value of Lighting Research. *LEUKOS - J Illum Eng Soc North Am* [Internet]. 2019;15(2–3):143–62. Available from: <https://doi.org/10.1080/15502724.2018.1533851>
48. 7.2.1.3. Anderson-Darling and Shapiro-Wilk tests [Internet]. 2009 [cited 2020 Oct 19]. p. 6–7. Available from: <https://www.itl.nist.gov/div898/handbook/prc/section2/prc213.htm>
49. Features H, Order D, Manual FAQ, Medcalc M, Shapiro T, Kolmogorov T, et al. Tests for Normal distribution [Internet]. 2011 [cited 2020 Oct 19]. Available from: <https://www.medcalc.org/manual/testsfornormaldistribution.php>
50. Features H, Order D, Manual FAQC, Distribution S, The D, The R. Normal plot [Internet]. 2014 [cited 2020 Oct 19]. p. 3–5. Available from: https://www.medcalc.org/manual/normal_plot.php
51. Box-and-whisker plot, boxplot [Internet]. [cited 2020 Oct 19]. Available from: https://www.medcalc.org/manual/box_and_whisker_plot.php
52. Behrouzkhia Z, Joveini Z, Keshavarzi B, Eyvazzadeh N, Aghdam RZ. Hyperthermia: How can it be used? *Oman Med J.* 2016;31(2):89–97.
53. Toraya-Brown S, Fiering S. Local tumour hyperthermia as immunotherapy for metastatic cancer. *Int J Hyperth.* 2014;30(8):531–9.
54. Gao S, Zheng M, Ren X, Tang Y, Liang X. Local hyperthermia in head and neck cancer: Mechanism, application and advance. *Oncotarget.* 2016;7(35):57367–

- 78.
55. Kaur P, Hurwitz MD, Krishnan S, Asea A. Combined hyperthermia and radiotherapy for the treatment of cancer. *Cancers (Basel)*. 2011;3(4):3799–823.
 56. Le Bihan D, Delannoy J, Levin RL. Temperature mapping with MR imaging of molecular diffusion: application to hyperthermia. *Radiology*. 1989;171(3):853–7.
 57. Viola Rieke, PhD and Kim Butts Pauly P. *MR Thermometry* Viola. North. 2008;29(10):1883–9.
 58. Odéen H, Parker DL. Magnetic resonance thermometry and its biological applications – Physical principles and practical considerations. *Prog Nucl Magn Reson Spectrosc*. 2019;110:34–61.